Decomposition experiments on *Cambarellus diminutus* (Decapoda: Cambaridae) under different environmental conditions and the influence of bacterial activity with regard to fossilization

Dissertation

zur

Erlangung des Doktorgrades (Dr. rer. nat.)

der

Mathematisch-Naturwissenschaftlichen Fakultät

der

Rheinischen Friedrich-Wilhelms-Universität Bonn

vorgelegt von

Dipl.-Biol. Bastian Mähler

aus

Bonn

Bonn, 2022

Angefertigt mit Genehmigung der Mathematisch-Naturwissenschaftlichen Fakultät der Rheinischen Friedrich-Wilhelms-Universität Bonn

Erstgutachter:	PD. Dr. rer. nat. Torsten Wappler
Zweitgutachter:	Prof. Dr. rer. nat. Thomas Martin
Tag der Promotion:	15. September 2022
Erscheinungsjahr:	2022

INDEX

Zusammenfassung

In der vorliegenden Dissertationsschrift wird der Zerfallsprozess des Flusskrebses *Cambarellus diminutus* (Decapoda, Cambaridae) unter verschiedenen Umgebungsbedingungen im Süßwasser erläutert.

Chapter 1.1

Die Evolution und Phylogenie der Arthropoden werden bis heute diskutiert. In dieser Diskussion spielen neben dem Erhalt von Hartgeweben, wie dem Exoskelett der Krebse, auch verschiedene Erhaltungsformen der Weichgewebe (Nervengewebe, gastrointestinal Strukturen) eine wichtige Rolle. Diese Weichgewebe werden unter „normalen" Bedingungen zügig zersetzt, sind jedoch trotzdem im Fossilbericht zu finden. Um die Zerfallsprozesse von Organsimen besser zu verstehen, wurden in den letzten 30 Jahren Studien zu diesem Thema durchgeführt. Denn, um die Prozesse der Fossilentstehung zu verstehen und Fehlinterpretationen zu vermeiden ist ein Verständnis über diese Zerfallsprozesse von essentieller Bedeutung. Ein Fossil kann nur dann entstehen, wenn gewisse Prozesse des Zerfalls stattfinden und/oder unterbrochen werden. Einen wichtigen und entscheidenden Einfluss haben dabei Mikroorganismen wie Bakterien und Pilze, die mit ihren Stoffwechselprodukten und dem bilden von Biofilmen die Umgebungsbedingungen maßgeblich verändern. Abiotische Faktoren wiederum, wie der pH-Wert, Sauerstoffgehalt, die Salinität und Temperatur beeinflussen die mikrobielle Aktivität. In diesem Projekt wurde eng mit der medizinischen Mikrobiologie zusammengearbeitet um den bakteriellen Einfluss auf den Zerfall und die Fossilisation besser verstehen zu können. Eine ausführliche Beschreibung der mikrobiologischen Untersuchungen und deren Auswertung findet sich in der Dissertationsschrift von Janssen (2021) mit dem Titel: „Der Einfluss bakterieller Aktivität auf die Präservierung und den Abbau von Weichgewebe".

Chapter 1.2

Für die nachfolgenden Studien wurde der Flusskrebs *Cambarellus diminutus* gewählt und im Labor gezüchtet. Da der Fokus in den Experimenten auf den Veränderungen der äußeren und inneren Strukturen lag, wird in diesem Kapitel die Anatomie der Tiere dargestellt und der Aufbau der Krustentier-Kutikula erläutert. Des Weiteren, werden Informationen über das sich in der Kutikula befindende Keto-Karotinoid „Astaxanthin" gegeben und der Häutungszyklus der Tiere erklärt. Abschließend werden einige verwendete Analyse-Methoden kurz beschrieben.

Chapter 2

In diesem Kapitel wird eine Übersicht des bisherigen Verständnisses zur Rolle mikrobieller Aktivität im Fossilisationsprozess gegeben. Bakterien spielen eine wichtige Rolle bei der Fossilisation von Weichgeweben. Durch ihre metabolischen Aktivitäten fördern sie deren Zerfall oder aber führen zu ihrer Mineralisation. Mangel an Sauerstoff, kalte Temperaturen und ein hoher Salzgehalt zählen zu den wichtigsten Umgebungsbedingungen, die eine Fossilisation begünstigen, da sie bakterielle Aktivitäten hemmen können. Bakterien sind jedoch sehr divers und haben ihre metabolischen Vorgänge an extreme Umweltbedingungen angepasst. Verschiedenste Beispiele zeigen, dass bisherige, einfache Annahmen über die Rolle von Bakterien bei der Fossilisation von Weichgeweben nicht in der Lage sind die Vorgänge ausreichend zu beschreiben. (i) Ergebnisse experimenteller Studien an Weichgeweben von Nesseltieren (Cnidaria) zeigten, dass sich bestimmte Weichgewebe unter Sauerstoffausschluss schneller zersetzten als unter sauerstoffreicher Atmosphäre. Zudem sind Fossilfunde dieser Gruppe häufiger in Fundstätten zu finden, die ein sauerstoffreiches Habitat wiederspiegeln als in Fundstätten die ein anoxisches Milieu darstellen. (ii) Siderit Konkretionen, die oftmals Weichgewebsfossilien enthalten entstehen durch ein komplexes Zusammenspiel aus Sulfat und Eisen reduzierenden Bakterien, im Gegensatz zu der eigentlichen Ansicht, dass Eisenreduktion den primären Treiber der Konkretionsbildung darstellt. (iii) Das Nervengewebe der Arthropoden, welches in vielen Fossilien des Kambriums gefunden wurde, zählt zu den Geweben, die sich unter Laborbedingungen, als erste zersetzen. Daher wird angenommen, dass zum Erhalt dieser Gewebe komplexe Prozesse notwendig sind, die von Bakterien beeinflusst werden.

Chapter 3

Im Fossilbericht sind Weichgewebe wie Muskeln oder innere Organe generell durch Pseudomorphosen vertreten, bei denen das organische Material meist durch Mineralausfällungen, wie Karbonat oder Phosphat, ersetzt ist. Durch Micro-Computertomographische Analysen (μ-CT) von sich zersetzenden Flusskrebsen in Aquarium-Wasser sowie destilliertem Wasser konnten Ausfällungen von Kristallstrukturen über die Zeit festgestellt werden. Rasterelektronenmikroskopische Aufnahmen (SEM) der kristallinen Strukturen zeigten sogar die Mineralisierung eines Muskels. Die folgenden Untersuchungen mittels der Konfokalen Raman Spektroskopie (CRS) zeigten, dass es sich bei den Kristallausfällungen und dem mineralisierten Muskel um Kalzit handelte. Eine massenspektrometrische Analyse des destillierten Wassers mit induktiv gekoppeltem Plasma

(ICPMS) zu Beginn des Experiments ergab einen Kalziumgehalt, der unterhalb der Nachweisgrenze lag, so dass davon ausgegangen werden konnte, dass ein Großteil der ausgefallenen Kalzium-Ionen, welche das Kalzit bildeten, aus den Tieren selbst stammte. Die Volumenberechnungen der 3-dimensionalen Modelle der Kalzit-Strukturen sowie der Gastrolithen zeigten einen Volumenanstieg der Kalzit-Ausfällungen mit fortschreitendem Zerfall und eine gleichzeitige Volumenabnahme der Gastrolithen. Individuen die sich in der Nachhäutungsphase befanden, zeigten ein geringeres Kalzit-Volumen als Individuen die sich zum Zeitpunkt des Todes in der Zwischen- oder Vorhäutungsphase befanden. Zudem zeigte die Analyse des gesamten Kalziumgehalts der Tiere, mittels Atomabsorptionsspektrophotometrie (AAS), dass sich mehr Kalzium in den Tieren befand, die keine Gastrolithen aufwiesen, als in den Tieren mit Gastrolithen. Es wird angenommen, dass in Individuen, die sich in der Zwischenhäutungsphase befinden, die Körpergröße entscheidend für die Menge des ausfallenden Kalzits ist und dass für Tiere die sich in der Vor- oder Nachhäutungsphase befinden die Phase an sich entscheidend ist.

Chapter 4

Weichgewebe sind im Fossilbericht oft durch sogenannte Pseudomorphosen überliefert, bei denen die organische Struktur durch Mineralien ersetzt wurde. In seltenen Fällen ist das Weichgewebe durch Pyrit ersetzt. Möglicherweise bildet Adipocire, in seiner Eigenschaft als formerhaltene Substanz, die Vorstufe bei der Pyritisierung von Weichgeweben unter anaeroben Bedingungen. Mit Hilfe von Hochdruckflüssigkeitschromatographie (HPLC) gekoppelt mit ultravioletter Photodiodenarray-Detektions Massenspektrometrie (UV/MS) und CRS konnte eine Umwandlung der Verdauungsdrüse des Flusskrebses *Cambarellus diminutus*, zu Adipocire, aber nur in Anwesenheit eines Biofilms, nach 9 Tagen nachgewiesen werden. Die für den Biofilm und möglicherweise für die Adipocirebildung verantwortlichen Mikroorganismen, wurden mittels 16S rRNA Gen Amplikon-Sequenzierung ermittelt. Des Weiteren zeigten die µ-CT Aufnahmen und Raman-Analysen eine Ausfällung von Kalzit in den Tieren. Es konnte zudem gezeigt werden, dass die Kalzit-Kristalle in Tieren die von einem Biofilm umschlossen waren, feinkörniger und dichter ausfielen und die Struktur der Kutikula besser nachbildeten, als die gröberen Kristalle, die ohne Biofilm ausfallen.

Chapter 5

Taphonomische Experimente mit künstlichem Meerwasser, Aquarium-Wasser und destilliertem Wasser haben gezeigt, dass es während des Zerfalls von Krebstieren (Crustacea) zu einer Ausfällung von Kalzit- und/oder Aragonit-Kristallen kommen kann und dass zudem organisches Gewebe, wie Muskeln und/oder die Verdauungsdrüsen mineralisiert bzw. konserviert werden können. Kapitel 5 dieser Arbeit beschreibt eine Studie, die sich mit den inneren und äußeren Veränderungen, während des Zerfalls von *Cambarellus diminutus* in Süßwasser mit Sediment, entnommen aus einem See in Bonn-Röttgen, befasst. Die Studie wurde in acht Versuchsansetze unterteilt, die sich in Temperatur, Sauerstoffgehalt und der Behandlung des Wassers und Sediments (unbehandelt / steril) unterschieden. Es zeigte sich, dass der Sauerstoffgehalt bei 24°C in der hier vorgestellten Studie einen minimalen Einfluss auf den Zerfall hatte, unabhängig davon ob Wasser und Sediment sterilisiert wurden oder nicht. Lediglich der Magen und die Verdauungsdrüse zersetzten sich 3 bis 4 Tage früher unter aeroben Bedingungen als unter anaeroben. Die 4°C Versuche zeigten hingegen, dass die Verdauungsorgane (Magen und Verdauungsdrüse) unter anaeroben Bedingungen deutlich schneller zersetzt wurden (nach 7 Tagen) als unter aeroben Bedingungen (nach 49 Tagen). Der Darm und das zentrale Nervensystem zersetzten sich bei 4°C nur unter anaeroben Bedingungen in unbehandeltem Wasser und Sediment. Es scheint damit, dass der Zerfall von Weichgeweben nicht pauschalisiert werden kann, sondern dass der Zerfall durch ein komplexes System aus Gewebetyp, Sauerstoffgehalt, Temperatur und mikrobiellen Einfluss bestimmt wird. μ-CT Aufnahmen und spätere Raman-Analysen zeigten, dass es zu einer höheren Kalzit-Ausfällung in Tieren bei 24°C kam, die sich in unbehandeltem Wasser zersetzten, als in Tieren, die sich in einem sterilen Medium befanden. Mikrobiologische Analysen ließen die Vermutung zu, dass für diese Ausfällungsunterschiede die bakterielle Gattung *Proteocatella* verantwortlich sein könnte.

Summary

The present dissertation deals with the decomposition process of *Cambarellus diminutus* (Decapoda: Cambaridae) in freshwater under different environmental conditions.

Chapter 1.1

Preserved hard tissues (e.g., exoskeleton) as well as soft tissues (gastrointestinal structures, nerve tissue) discovered from the fossil record play an important role in the discussion of the evolution and phylogeny of arthropods. During the last 30 years, taphonomic studies have been performed by several scientists to shed light upon the processes that are responsible for the formation of fossils. In order to understand the processes that lead to soft tissue preservation or the fossilization of the entire organism, knowledge of the decay processes is essential. A fossil only occurs if certain decay processes take place and/or are interrupted. Microorganisms such as bacteria and fungi are the main drivers of decomposition and therefore important for the studies on taphonomy. Microorganisms have an important influence on the environmental conditions, caused by their metabolic products and the formation of biofilms. Abiotic factors such as pH, oxygen content, salinity and temperature influence the microbial activity. Therefore, in this project I worked closely with the medical microbiology in order to understand the bacterial influence on decay and fossilization. A detailed description of the microbiological investigations and their evaluation can be found in the dissertation of Janssen (2021) entitled: „Der Einfluss bakterieller Aktivität auf die Präservierung und den Abbau von Weichgewebe."

Chapter 1.2

For the following studies the freshwater crayfish *Cambarellus diminutus* was chosen and bred in our lab. The main focus of this study was on morphological and inner anatomical changes. Therefore, general morphological and inner anatomical features are given in chapter 1.2. In addition, information about the general structure of the crustacean cuticle, the ketocarotinoid astaxanthin and the moulting cycle are given. Further on, some applied methods are presented.

Chapter 2

Chapter 2 is a review about the general understanding on the role of microbial activity in fossilization. Bacteria play an important role in the preservation of soft tissues caused by their metabolic activity that promote decay or lead to mineralization. Lack of oxygen, low temperatures and high salinity are important abiotic factors that might promote fossilization, as they can inhibit bacterial activity. However, bacteria are highly divers and adapted their

metabolic activity to extreme environmental conditions. A lot of examples show, that general simple assumptions on the role of bacteria during the preservation of soft tissues are unable to explain the processes that lead to fossilization. (i) Taphonomic experiments on cnidarian soft tissues revealed, that in contrast to aerobic conditions, low oxygen levels fasten decay. In addition, fossils of this group are found more frequently in fossil sites that reflect an oxygen rich habitat than in fossil sites that represent an anoxic environment. (ii) Siderite concretions often contain soft tissue fossils and are formed by a complex interplay of sulfate and iron-reducing bacteria, contrary to the traditional view that iron reduction is the primary driver of the formation of concretions. (iii) Arthropod nerve tissue, found in many Cambrian fossils, is one of the first tissues that decompose under laboratory conditions. Therefore, it is assumed that the preservation of these tissues requires complex processes that are influenced by bacteria.

Chapter 3

In the fossil record soft tissues (e.g., muscles and inner organs) are generally preserved as pseudomorphs in which the organic material is replaced by carbonate or phosphate. Observations of decomposing crayfish in tank- and distilled water with micro-computed tomography (μ-CT) revealed a precipitation of crystal structures over time. In addition, a mineralized muscle was found by scanning electron microscopy (SEM). Confocal Raman spectroscopy (CRS) on crystal structures and the mineralized muscle revealed that they consist of well-ordered calcite. Inductively coupled mass spectrometry of distilled water showed a calcium level under the detection limit at the beginning of the experiment. Therefore, it is assumed that calcium ions that are needed for the calcite precipitation were mostly provided by the carcasses themselves.

Volume measurements of 3-dimensional models of calcite clusters and gastroliths revealed a volume increase of calcite and simultaneously a volume reduction of gastroliths with progressive decay. Individuals which were in the postmoult phase showed a smaller total volume of precipitated calcite, compared to specimens that were in the intermoult or premoult phase. Measurements of the complete body calcium of *Cambarellus diminutus* by atomic absorption spectrophotometry (AAS) revealed a lower amount of calcium in individuals with gastroliths than in individuals without these structures. It is assumed, that the higher the body size the higher the precipitated calcite, if the animals were in the intermoult phase at the time of death. If the individuals were in the premoult or postmoult phase, the phase itself seems to be important.

Chapter 4

In the fossil record soft tissues are represented as so called pseudomorphs in which the organic material is replaced by minerals. In rare cases soft tissues are preserved in pyrite. In some cases, adipocere might be the first step in soft tissue preservation as a shaping component. In this study, high performance liquid chromatography (HPLC) coupled with ultraviolet mass spectrometry (UV/MS) and CRS showed the transformation of the digestive gland of *Cambarellus diminutus* into adipocere in just 9 days only inside a biofilm. With 16S rRNA gene amplicon sequencing microorganisms that might responsible for the biofilm and the adipocere formation were determined. Further on, µ-CT analysis and CRS revealed a precipitation of calcite inside the animals. Calcite crystals that precipitated inside the biofilms were fine grained and replicated the structures of the cuticles better than the coarse precipitates that occurred without a biofilm.

Chapter 5

Taphonomic experiments with artificial seawater, tank water and distilled water revealed a precipitation of minerals (calcite or aragonite) and soft tissue preservation by phosphates and carbonates during the decay of crustaceans. A study with 8 different experimental setups described the inner and outer changes during the decay of *Cambarellus diminutus* in freshwater and sediment, taken from a lake in Bonn-Röttgen. The experiments differed in temperature, oxygen level and treatment of water and sediment (untreated/sterile). The oxygen content at a constant temperature of 24°C had a minimal influence on the decay whether the medium was untreated or sterile. Only the stomach and the digestive gland decomposed 3 to 4 days earlier under aerobic conditions than under partly anaerobic conditions. Experiments that were conducted at 4°C revealed a decomposition of stomach and digestive gland after 7 days under partly anaerobic conditions and a decomposition of these organs only after 49 days under aerobic conditions. Guts and the general nerve cord have been decomposed at 4°C only under partly anaerobic conditions and in untreated water and sediment. It seems, that the decomposition of soft tissue cannot be generalized, but is a complex interaction of tissue type, oxygen level, temperature and microbial influence. µ-CT observations and Raman analyses revealed a higher precipitation of calcite at 24°C in animals that decomposed in untreated water than in animals which decayed under sterile conditions. Caused by microbiological investigations it is assumed, that the bacterial genus *Proteocatella* might be responsible for the difference in calcite precipitation.

Abbreviations

2D	Two dimensional
3D	Three dimensional
4D	Four dimensional
AAS	Atom Absorption Spectrophotometry
AB	Abdominal cord
ACC	Amorphous Calcium Carbonate
AHPO	Alkaline Hydrogen Peroxide Oxidation
AI	Additional Information
AS	Additional Study
ASV	Amplicon Sequencing Variant
avg.	Average
AXT	Astaxanthin
b	Bacteria
BIM	Biological Induced Mineralization
brn	Branchia
bs	Body size
BSE	Back Scattered Electron
bspd	Basipodite
C	Carbon
Ca	Calcium
$CaCO_3$	Calcium carbonate
$CaPO_4$	Calcium phosphate
cc	Calcite cluster
chpd	Cheliped
Cl	Chlorine
cm	Centimeter
CO_2	Carbon dioxide
CP	Check plot
crppd	Carpopodite

CRS	Confocal Raman Spectroscopy
CT	Computed Tomography
Cu	Copper
d	Day
Da	Dalton
dist	Distilled water
DL	Detection Limit
DNA	Desoxyribonucleicacid
ecm	Extra cellular matrix
e.g.	Exempli gratia
EIC	Extracted ion chromatograms
ENA	European Nucleotide Archive
EPS	Extracellular Polymeric Substances
ESI-MS	Electrospray Positive Ion-Mass Spectra
EXP	Experiment
Exp.	Experiment
f	Fungi
FTIR	Fourier-Transform Infrared Spectroscopy
g	Gram
GL	Gastrolith
H_2CO_3	Carbonic acid
H_2O	Water
H_2SO_4	Sulfuric acid
HNO_3	Nitric acid
HPLC	High Performance Liquid Chromatography
ICPMS	Inductively Coupled Plasma-Mass Spectrometry
INSD	International Nucleotide Sequence Database
iscpd	Ischiopodite
kV	Kilo Volt
L	Liter
mg	Milligram

$MgCO_3$	Magnesium carbonate
min	Minutes
mL	Milliliter
mm	Millimeter
mm^3	Cubic millimeter
MR	Magnetic resonance
mrpd	Meropodite
MV	Mean Value
mxpd	Maxilliped
$M\Omega$	Mega Ohm
m/z	Mass to ratio
N_2	Nitrogen
NaCl	Sodium chloride
NO^{3-}	Nitrate
Pb	Plumbum
PCC	Pearson Correlation Coefficient
PCR	Polymerase Chain Reaction
Py-GCMS	Pyrolysis-Gas Chromatography-Mass Spectrometry
R^2	Regression line
Rh	Rhodium
s	Seconds
S	Sulphur
S1; S2; …	Supplement 1; Supplement 2; …
SEM	Scanning Electron Microscope
$[SO_4]^{2-}$	Sulfate
STD	Standard
tank	Tank water
TVC	Total Volume of Calcite
TVG	Total Volume of Gastrolith
V	Volume
ww	Wet weight

Zn	Zinc
μA	Micro Ampere
μ-CT	Micro-Computed Tomography
μg	Microgram
μm	Micrometer

LIST OF FIGURES

Chapter 5

APPENDIX

Chapter 3

Additional Information (AI)

FIGURE AI 1. 3D-model of the right cheliped of sample C9$_{dist.}$ with mineralized parts of opener muscles (yellow) and the closer muscles (red).

FIGURE AI 2. Representative Raman spectra of observed muscle remains compared to Raman reference spectra of crystalline apatite and calcite.

FIGURE AI 3. Photos and SEM images of mineralized structures discovered from the right cheliped of *C. diminutus* C9$_{dist.}$

FIGURE AI 4. Images of dissolving gastroliths during the decomposition of *C. diminutus* (C9$_{tank}$) in freshwater.

Additional Study (AS)

FIGURE AS 1. Translucent 3D-models of *C. diminutus*.

FIGURE AS 2. Comparison of the amount of dissolved calcium ions in tank water samples and distilled water samples for a duration of 11 days.

FIGURE AS 3. SEM images of mineralized structures discovered from the pereiopods and the gut of *C. diminutus* C13$_{dist.}$

FIGURE AS 4. Representative Raman spectra of observed crystal clusters compared to Raman reference spectra of crystalline calcite and apatite.

FIGURE AS 5. Mean values of TVC of individuals which decomposed in tank- and distilled water on day 11.

Chapter 4

SUPPLEMENTARY FIGURE S1. Structures of the free fatty acids.

SUPPLEMENTARY FIGURE S2. Extracted ion chromatograms (EIC).

LIST OF TABLES

Chapter 4

APPENDIX

Chapter 3

Additional study (AS)

Chapter 4

Chapter 5

Danksagung

Als erstes möchte ich mich bei meinem ehemaligen Betreuer **Jes Rust** für sein Vertrauen und seine Unterstützung in den ersten Jahren dieser Arbeit bedanken. Ich wünsche ihm alles Gute und eine baldige Genesung.

Als nächstes bedanke ich mich bei **Torsten Wappler** der die Betreuung in der Schlussphase dieser Arbeit ohne Zögern übernommen hat und mir mit Rat und Tat zur Seite stand.

Ich bedanke mich bei **Thomas Martin**, meinem Zweitgutachter und **Thorsten Geisler-Wierwille**, meinem Drittgutachter für ihre Unterstützung.

Weiterhin bedanke ich mich besonders bei **Gabriele Bierbaum** für viele Stunden intensiver Diskussionen, Gespräche und Ideen, sowie für ihre großartige Unterstützung während dieser Arbeit.

In diesem Rahmen bedanke ich mich ebenfalls besonders bei **Kathrin Janssen** für ihre tolle Unterstützung in diesem Projekt und die großartigen Diskussionen. Nicht zu vergessen sind die zahlreichen zwischenmenschlichen Gespräche, die mir immer wieder Mut gemacht haben. Vielen lieben Dank. Ohne dich wäre diese Zeit nur halb so schön gewesen.

Ich bedanke mich außerdem bei **Julia Schultz** für die tolle Unterstützung während dieser Arbeit und die aufbauenden Worte, wenn meine Fäden am Kopf mal wieder zu viele wurden. Außerdem bedanke ich mich für die schönen und lustigen Videoabende, die die Zeit einfacher gemacht haben.

Ich bedanke mich bei **Frauke Stebner** für die vielen tollen Mittagessen zusammen und großartigen Gespräche dabei.

Ich bedanke mich des Weiteren bei **Rico Schellhorn** für seine große Hilfsbereitschaft in fachlichen Dingen aber auch im Privaten z.B. beim Maibaumstellen.

Ich danke den Mitgliedern meiner Arbeitsgruppe für das tolle Arbeitsklima und die interessanten Arbeitsgruppentreffen. Nicht zu vergessen **Bruno** unserem AG Therapie-Hund.

Ich danke den **Blätterteigtaschen** und den **Bonn English Singers** für die vielen schönen Stunden mit Gesang und Freude.

Ein besonderer Dank gilt **Martin Landsberg** der mir in einer meiner schwierigsten Phasen meines Lebens eine große Hilfe war.

Ich bedanke mich ebenfalls bei **Andreas Lamberz-Brendler** von der Unteren Naturschutzbehörde der Stadt Bonn für seine Unterstützung.

Ich danke **Claudia Schmidt** vom Promotionsbüro der Universität Bonn für Ihre tolle Unterstützung und schnellen Antworten.

Ich bedanke mich bei **meiner gesamten Familie** für ihre Unterstützung und die vielen schönen Momente.

Zum Schluss möchte ich mich noch bei meiner Frau **Malina Gupta-Mähler** bedanken. Danke, dass du mich in der gesamten Zeit nach besten Kräften unterstützt hast. Ohne dich wäre diese Arbeit nicht möglich gewesen.

Chapter 1

General Introduction

1.1 Current stage of research

Arthropods are highly diverse and represented 85 % of the known Metazoans. The fossil record is outstandingly rich and dates back to the lower Cambrian (Edgecombe, 2020; and references therein). However, evolution and phylogeny of this diverse group are still subject of discussion, because the interpretation of the fossil data is limited to morphological features and often only fossils of exceptional preservation contribute to these discussions. Understanding the processes of hard and soft tissue preservation might be important for studies on arthropods, because fossilized digestive systems and/or nervous systems are used for the interpretation of the evolutionary success and the phylogeny of arthropods (Ma et al., 2012; Vannier et al., 2014; Yang et al., 2016; Ortega-Hernández et al., 2022). Therefore, actuo-paleontological studies on taphonomy are essential. These studies can also provide new information that can lead to a reinterpretation of previously described fossils. For example, Roger (1946) described calcite spheres in two crustacean specimens, of the upper Pleistocene Plattenkalk of Sahel-Alma (Lebanon), as mineralized eggs because of their size and location inside the specimens. Based on the results of Briggs and Kear (1993a), which had studied the decomposition of the shrimp *Crangon crangon,* Briggs and Wilby (1996) were able to reinterpret these eggs as only simple calcite bundles which occur during the decomposition of crustacean under marine conditions.

During the last 30 years actuo-paleontological studies on taphonomy were carried out to shed light upon the conditions that are responsible for soft tissue preservation (Briggs and Kear, 1993a; 1994; Sagemann et al., 1999; Martin et al., 2003; Sansom, 2010; Naimark et al., 2018). Soft tissues decompose very quickly under "normal" conditions but are still found in the fossil record as so called pseudomorphs, which are generally formed through the replacement of soft tissue by minerals e.g., phosphate, carbonate or pyrite (Martill, 1988; Wilby & Whyte, 1995; Briggs et al., 2011; Schiffbauer et al., 2014). To understand these processes that lead to the preservation of soft tissues, it is crucial to understand the processes that take place after an organism died and the function of involved microorganisms.

Only a few minutes after death endogenous enzymes like proteases, lipases and amylases start to digest body cells by a process called autolysis (Penning, 2006; Krause & Jachau, 2007). The activity of these enzymes is highly temperature depended and leads to remarkable changes. The higher the temperature, the faster the decomposition process is. Cell membranes rupture due to water inlet and tissue fluids of the cells are released (Schoenen, 2019). These released tissue

fluids serve microorganisms as a source of nutrition and they spread over the entire body starting from the most densely populated body regions (e.g., gastric, intestine, respiratory systems and skin).

The activity of bacteria is strongly influenced by abiotic factors in which water is the most important for bacterial life and growth (Schoenen, 2019). In addition, bacteria are highly sensitive to temperature, salinity, pH-value and oxygen. These parameters influence the ability of strains to successfully colonize a habitat or regulate the production of specific degrading exoenzymes (catalytic proteins secreted by the bacterial cell into the surrounding environment) according to the availability of nutrients, oxygen, bacterial cell density, and growth phase (Barbieri et al., 2016; Hertel et al., 2017; McAdams et al., 2004).

Each bacterial species has an optimum growth temperature and in many bacterial species, biochemical processes and membrane fluidity slow down at temperatures under 20°C. The membrane fluidity is important for transmembrane voltage and transport processes of the cells. Freezing temperatures are able to reduce bacterial decay processes over thousands of years, leading to soft tissue preservation (e.g., mammoth brains in permafrost) (Kharlamova et al, 2016). However, some bacterial groups, called "psychrophilic", can maintain their metabolic activity and growth rate in temperatures below 20°C (Pearce, 2012). Psychrophilic bacteria might have the ability to degrade organic matter or might have "fossilization" potential even in freezing temperatures. For example, Elster et al. (2016) collected calcite needles directly from the surface of a biofilm, found in two shallow lakes at the Island of James Ross (Antarctica), and assumed that among other possibilities, these calcite structures were formed by a unique bacterial community whose composition has not yet been described.

Beneath low temperatures, high salinity can inhibit the decomposition of soft tissues by microorganisms. A nice example from the fossil record is given by the Upper Jurassic Plattenkalk of Solnhofen, which is well known for its exceptional fossils and was most likely deposited in an environment in which surface waters overlaid deep hypersaline waters (Gäb et al., 2020). Halophilic microorganisms are able to tolerate high salinity in water (Oren, 2002) and were found in great salt lakes in Utah, in which the salinity can be seasonally eight times higher than in "normal" sea water (3.5 % NaCl) (Lee & Eom, 2016; Tazi et al., 2014). Various hypersaline lakes like "Lake Thetis" in Australia show a large number of dolomites and stromatolites (Grey et al., 1990; Reitner et al., 1996) and it is assumed that microbial mats of halophilic microorganisms are responsible for the formation of dolomites* (Warthmann et al., 2000; You et al., 2013).

*Dolomite [$CaMg(CO_3)_2$] has also been proven in the lumen of the heart of the early crustacean fossils of *Dollocaris ingens*, discovered from the Konservat-Lagerstätte of La Voulte-sûr-Rhone in France (Jauvion et al., 2020).

This assumption was supported by Warthmann et al. (2005) by the isolation of the microorganism *Desulfovibrio brasiliensis* from the hypersaline Lake "Lagoa Vermelha" (Brazil), which is able to precipitate dolomite by the reduction of sulphate. The degradative activity of halophilic organisms, caused by their ability to excrete hydrolytic enzymes (e.g., lipases, amylases and proteases) (Ghasemi et al., 2011; De Lourdes Moreno et al., 2013), along with their ability to influence mineral precipitation, might be key factors in fossilization or decay in high-salinity environments.

Another abiotic factor which influences bacterial activity and therefore favor the preservation of soft tissues is the pH-value. Most bacterial species prefer pH-values between 5 and 9, whereby deviations from this range can have a significant impact on their decay ability or metabolism (Horikoshi, 1999). The Eocene Green River Formation in North America is famous for its diverse biota of exceptional preserved fossils and was deposited by lake sedimentation in an environment in which freshwater alternated with highly alkaline and hyper saline conditions (Surdam & Stanley, 1979). Today, the Green River Formation hosts the largest concentrations of trona worldwide, a mineral that indicates a pH-value of >11 (Gäb et al., 2020). The combination of high pH-values and partly high salinity might have contributed to the outstanding preservation of fossils, because fossilization experiments on fish revealed that these conditions can inhibit or slow down decay processes (Gäb et al., 2020). But not only the environment can influence the pH-value, also bacteria are able to shift the pH-level by the extraction of metabolic products like organic acids and amines during decay (Berner, 1968; Vass, 2001). Fluctuations of the pH-value caused by microbial activity can lead to the precipitation of apatite (pH decrease) or calcite and/or aragonite (pH increase), as it was demonstrated in actuo-paleontological studies on taphonomy (Briggs & Kear, 1993a; 1994; Sagemann et al., 1999; Raff et al., 2008). In standard artificial seawater under laboratory conditions carbonate crystals precipitated inside the carcasses of the shrimp *Crangon crangon*, the prawn *Palaenon elegans* and the mantis shrimp *Neogonodactylus oerstedi* when pH-values were low, and soft tissues (e.g., muscles) were mineralized by apatite after the pH-value increased (Briggs and Kear 1993a; 1994; Hof and Briggs, 1997; Sagemann et al., 1999). The mineralization into calcite or apatite plays a significant role in the preservation of soft tissues (e.g., muscle tissue) in the fossil record (McCobb, 1998; Sagemann et al., 1999).

The decomposition or preservation of soft tissues is also influenced by the oxygen level of the surrounded medium due to its impact on the microbial community. Even if the general opinion is that anoxic conditions promote soft tissue preservation, taphonomic studies could not clearly demonstrate the role of aerobic or anaerobic conditions in soft tissue preservation. While some

results indicate faster decomposition of soft tissue under aerobic conditions (Briggs & Kear, 1993a, 1993b; Gostling et al., 2009; Martin et al., 2003), other experimental results show no differences in comparison to anaerobic decay (Allison, 1988; Kidwell & Baumiller, 1990) or only rare differences under various oxygen conditions (Bartley, 1996; Briggs & Kear, 1994). Especially, one study highlighted that some cnidarian tissues decayed even faster when oxygen is not available (Hancy & Antcliffe, 2020).

But the limited access to oxygen can also lead to the incomplete hydrolysis of fat and the formation of adipocere by bacterial influence (Krauland, 1943; Nanikawa, 1973; Tomita, 1984; Takatori et al., 1986; Schoenen & Schoenen, 2013). This greasy to lime-hard substance (Krause & Jachau, 2007) can also be formed by the conversion of muscle tissue (Brinkmann, 2003) or substances such as sphingosine (Schoenen, 2019). Fechner (1827) describes adipocere as a granular, light substance with a more or less white color. The main components of adipocere are higher fatty acids such as palmitic acid, stearic acid and mystric acid (Wetherhill, 1856; Nanikawa, 1973; Brinkmann, 2003; Forbes et al., 2005). The formation of adipocere is highly temperature dependent (Prokop & Göhler, 1976; Penning, 2006) and will be promoted by moisture (Zillner, 1885) and partial or complete exclusion of oxygen (Mant, 1987). Therefore, adipocere is especially formed in water corpse, corpses in clayish soils, and moist crypts (Penning, 2006). The preservation of soft tissue by adipocere, is an interesting aspect for paleontology as this substance has the ability to slow down or inhibit decay process (Forbes et al., 2005) and has been suggested as a key component in the outstanding preservation of fossils in Konservat-Lagerstätten like Messel or Holzmaden (Schwermann et al., 2012). In this complex fabric of abiotic and biotic factors that influence each other, properties of the involved bacteria play an important role. For example, *Pseudomonas tunicata*, an anaerobic marine bacterium forms pseudomorphs under aerobic conditions, but destroys the internal structures of cells after oxygen is depleted or is not available (Raff et al., 2014).

In aquatic environments bacteria occur as free-floating cells (planktonic lifestyle) or are bound at surfaces with other bacterial cells to form communities, which are called biofilms (sessile lifestyle). After the adhesion on a surface, bacteria multiply to a threshold density and induce the expression of biosynthesis genes that control the synthesis of an extracellular polymeric substance (EPS), which is composed out of polysaccharides, proteins, lipids and extracellular DNA. An EPS serves as a protective barrier against chemicals, scavengers and dehydration. In addition, it provides a perfect environment for interactions between different kinds of microorganisms (Mah & O´Toole, 2001; Flemming & Wingender, 2010).

A complex type of a biofilm is a microbial mat, which is formed if a microbial community is layered on the basis of abiotic gradients such as water, light, and oxygen (Stolz, 2000). The thickness of microbial mats varies from some millimeters to multiple centimeters (Prieto-Barajas et al., 2018). Extant microbial mats are mostly located in extreme habitats, caused by the limitation of biofilm-grazing organisms, due to the harsh environment which could be hypersaline, alkaline, or high or low in temperature (Schneider et al., 2013; Arp et al., 2003; Klatt et al., 2013; Ohtsuka et al., 2006).

Biofilms and microbial mats might play an important role in the fossilization process, because under aquatic conditions dead organisms could be enveloped by a biofilm, which seems to slow down decay processes (Briggs, 2003). Inside the biofilm environmental conditions will change due to microbial activity and mineralization might occur, leading to preservation of tissues and later to fossilization. Iniesto et al. (2013; 2016; 2017) were able to preserve muscle fibers in frogs and fish by placing the carcasses on microbial mats for a duration of 3 years. In addition, the midbrain of a frog, lying on a microbial mat, was replaced by calcium carbonate after 1.5 years (Iniesto et al., 2015).

But there is still only a limited knowledge about individual bacterial species, their impact on decay and preservation and their origin, either from the animal microbiome or from the biotope where the animal died. The experimental results of Butler et al. (2015) indicated a stabilizing influence of endogenous microorganisms from the gastro-intestinal flora of the brine shrimp Artemia, whereby Eagan et al. (2017) showed that each organism exhibits an individual microbiome that can support preservation or fasten decay.

More information and case studies that highlighted the complex role of microbes in fossilization is given in chapter 2.

The goal of this study was to create a general understanding of the different aspects of the decay and mineralization processes in arthropods, in context with microbial activity. Therefore, disarticulation and decomposition of hard and soft tissues were observed and the development of microbial communities on the carcasses over time were studied. A detailed description of the microbiological investigations and their evaluation can be found in the dissertation of Janssen (2021) with the title: „Der Einfluss bakterieller Aktivität auf die Präservierung und den Abbau von Weichgewebe". To address the topic of decay and mineralization processes in arthropods, it is essential to understand the mechanisms of the decomposition processes under different environmental conditions and the role of microorganisms therein.

Today there is a number of experimental studies on mineralization and preservation of soft tissues, but they are mainly limited to marine conditions (Briggs & Kear, 1993a; 1994; Hof &

Briggs, 1997; Butler et al., 2015; Eagan et al., 2017; Naimark et al., 2018). During the experiments of Briggs & Kear (1993a; 1994) and Hof & Briggs (1997) aragonite clusters precipitated early diagenetic under artificial seawater conditions, that were known as calcite clusters from marine fossil deposits (Briggs & Wilby, 1996). However, since these calcite bundles have also been observed in crustaceans from the laminated green marls of Cherasco in Northern Italy and from the lacustrine plattenkalks of Las Hoyas in Spain (Briggs & Wilby, 1996), it was tested whether these precipitations are early diagenetic under freshwater conditions and whether the required calcium ions originate from the individuals themselves or from the surrounding medium.

Actuo-paleontological studies of Briggs & Kear (1993a) and Hof & Briggs (1997) revealed a muscle preservation by calcium phosphate under marine conditions and in 2019 Klompmaker et al. published the first global data set of exceptionally preserved muscle tissue in fossil malacostraca and postulated that muscles are primarily preserved through phosphatization, whereby most of the data belongs to marine, brackish or high saline fossil deposits. Therefore, it was tested if such a preservation scenario will also occur under freshwater conditions and if it is also early diagenetic. During the experiments of Briggs & Kear (1993a; 1994) precipitation of crystal bundles composed of aragonite occurred within the carcasses. Sagemann et al., (1999) also observed a precipitation of crystal bundles in artificial seawater, but they were composed of calcite as it is known from the fossil record (Briggs & Wilby, 1996).

In this study, it was tested if the body size and/or the stage of moulting have an influence on the precipitation of calcite and maybe on the preservation of muscle tissue.

As mentioned above, there is still only a limited knowledge about extrinsic and intrinsic bacteria and their impact on decomposition and preservation. Therefore, the influence of extrinsic microorganisms on the decay of *Cambarellus diminutus* in freshwater was shown. In addition, the influence of different environmental conditions and the impact of bacteria on the decomposition of *C. diminutus* in natural lake water and sediment was investigated.

1.2 Material

For the following studies the freshwater crayfish *Cambarellus diminutus* was used, because of its lightly sclerotization, his optimal body size for micro-computed tomography and the easy way of breeding. It was decided to breed the animals due to various problems with purchasing, like unknown type of feed, treating with antifungal and antibacterial agents or contamination with parasites, symbionts or commensals.

1.2.1 Breeding of *Cambarellus diminutus*

Individuals of the extant crayfish *Cambarellus diminutus* were raised in a settled tank community in the lab. The animals were kept in 54 L tanks of 60 x 30 x 30 cm in size, at a constant water temperature of 26°C. Tanks were filled with pipe water and fortified with "Biotopol C" water conditioner (JBL, GmbH & Co. KG, Neuhofen, Germany) to neutralise zinc (Zn) and plumbum (Pb) and to remove chlorine (Cl) and bind copper (Cu). The crayfish were fed with nothing but "Crab Natural" (Sera, GmbH, Heinsberg, Germany), a main food for crayfish.

Ingredients: Fish meal, corn starch, wheat flour, spirulina, brewers yeast, wheat germ, gammarus, Ca-caseinate, sea algae, stinging nettle, willow bark, alder cones, fish oil (containing 49 % omega fatty acids), mannan oligosaccharides, herbs, alfalfa, parsley, paprika, green-lipped mussel, spinach, carrots, *Haematococcus* algae, garlic.

Analytical constituents

Crude Protein 36.7 %, Crude Fat 11.1 %, Crude Fiber 4.5 %, Moisture 5.2 %, Crude Ash 8.6 %, Ca 1.9 %, P 1.0 %.

Additives

Vitamins and provitamins: Vit. A 37,000 IU/kg, Vit. D3 1,800 IU/kg, Vit. E (D, L-α-tocopheryl acetate) 120 mg/kg, Vit. B1 35 mg/kg, Vit. B2 90 mg/kg, stab. Vit. C (L-ascorbyl monophosphate) 550 mg/kg.

1.2.2 General morphological features

The crayfish is divided in two tagmata: Cephalothorax and pleon. The cephalothorax is composed out of the carapax and rostrum, two compound eyes, two pairs of antennae, and five pairs of pereiopods (legs). The first pair of pereiopods has two giant chelae and is also called chelipeds. The chelae are divided in the propodus and the mobile dactylus. The pleon is composed of six abdominal segments called pleomeres, the telson, and the uropods. Each of the first five abdominal segments carries one pair of pleopods (swimmerets) (**Figure 1**).
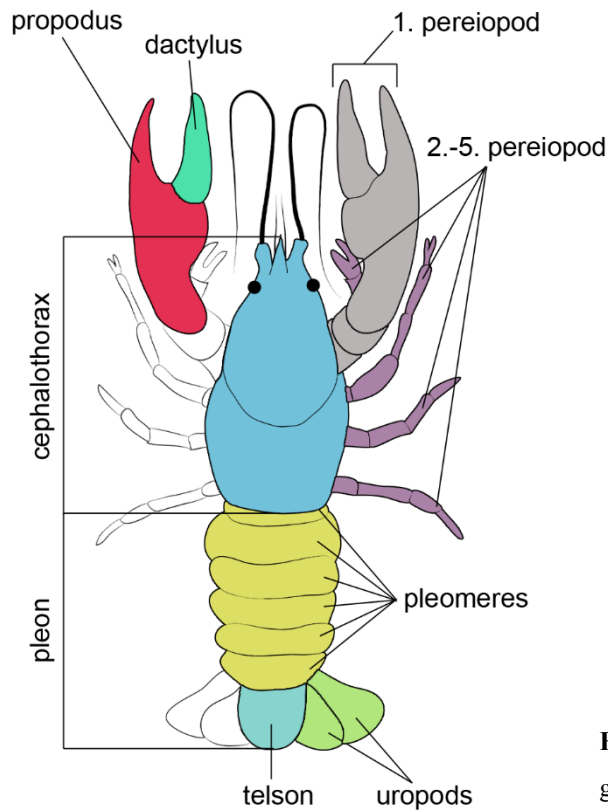
FIGURE 1. Dorsal view of a crayfish showing general morphological features

1.2.3 General inner anatomy

The inner anatomy is mainly composed of the gastric (stomach), the intestine (gut), ganglion (ventral nerve cord), hepatopancreas (digestive gland), coxal gland (green gland or antennal gland), heart, cerebral ganglion (brain), branchiae (gills) and muscles (**Figure 2**).
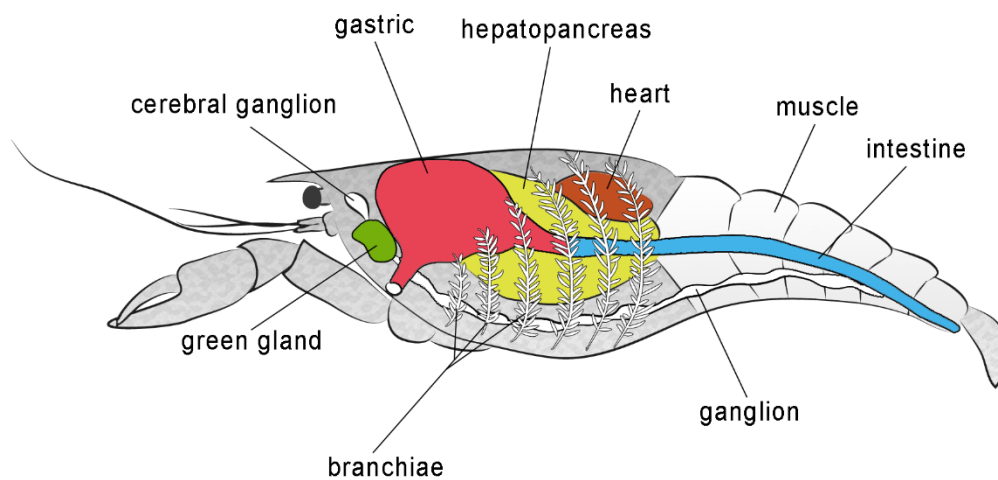
FIGURE 2. Lateral view of a crayfish showing general inner anatomical features

1.2.4 General construction of the crustacean cuticle

The cuticle of the crustaceans is divided into four main layers (**Figure 3**).

The outermost layer is the epicuticle, which is the thinnest of all layers and consists of calcium carbonate ($CaCO_3$) and lipoproteins. Immediately under the epicuticle lies the exocuticle, which is composed out of chitin-protein fibers as the main framework and is stabilized by calcite crystals in between (Travis, 1955a). The exocuticle is also known as the pigmented layer (Giraud-Guille, 1984) and contains the α-crustacynin-protein complex, responsible for the blue color in crustaceans (e.g., *Cambarellus diminutus*). The endocuticle is the broadest and most calcified layer of the cuticle (Travis, 1965). $CaCO_3$ occurs in form of calcite or as poorly crystalline amorphous calcium carbonate in the three cuticle layers (Travis, 1963). The innermost layer of the cuticle is the epidermal layer or membranous layer. It mainly consists of protein and chitin without any minerals (Travis, 1955a).
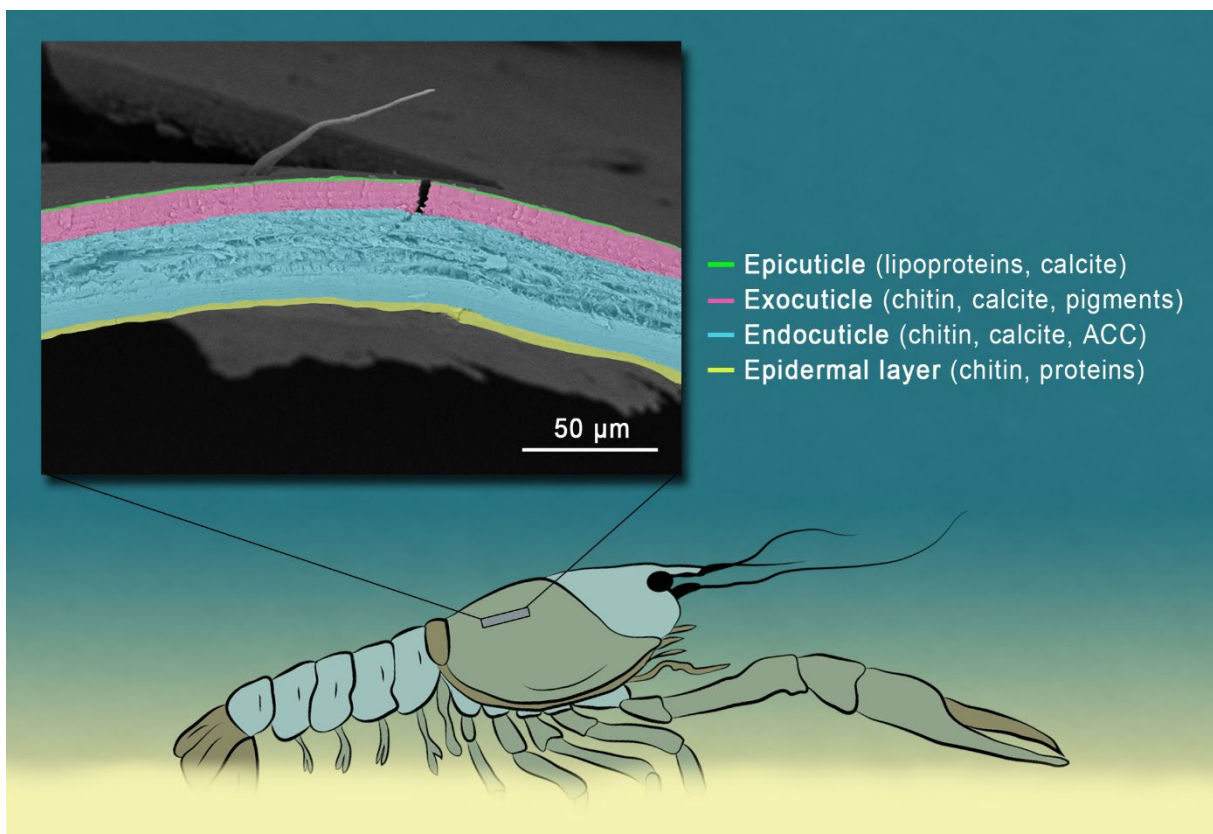
FIGURE 3. General construction of the crustacean cuticle. BSE-image of a cross section of a fresh crayfish cuticle with colored layers.

1.2.5 Astaxanthin

The ketocarotenoid Astaxanthin (AXT) [3,3'-dihydroxy-β,β carotene-4,4' dione] is an omnipresent pigment in nature (Yuan et al., 2011) and the main carotenoid in aquatic animals e.g., crustaceans (Miki, 1991; Hussein et al., 2006; Higuera-Ciapara et al., 2006). AXT, like other carotenoids, cannot be produced by the animals themselves and will be taken up by nutrition (Jyonouchi et al., 1995). In nature AXT is biosynthesized by microalgae, phytoplankton, fungi and bacteria, particularly in marine environments (Yuan et al., 2011). But it is also produced by freshwater microalgae, e.g., *Haematococcus pluvialis* (Harker et al., 1996) and *Chlorella sorokiniana* (Raman & Mohamad, 2012). In living crustaceans AXT is ligated to the α-crustacyanin protein complex, located in the upper cuticle layer of the exocuticle. If the protein complex is intact the carapace shows a blue coloration. During the decay process the protein complex can be denaturized, caused by autolytic enzymes and/or bacterial degradation. If the protein complex is denaturized AXT molecules will be uncombined from the α-crustacyanin protein complex resulting in a red coloration of the cuticle (Korger, 2005) (**Figure 4**).

AXT is well known for its anti-inflammatory (Bennedsen et al., 1999) and antioxidative properties (Miki,1991) and has positive effects on cancer, diabetes, and the immune system in human health (Hussein et al., 2006; Higuera-Ciapara et al., 2006 and references therein). AXT is a carotenoid that works against a variety of gram + and gram – pathogens like *Pseudomonas* sp., *Bacillus* sp., *Salmonella* sp., and *Staphylococcus* sp. (Ushakumari & Ramanuja, 2013) and further on, against *Helicobacter* sp. (Bennedsen et al., 1999; Wang et al., 2000), *Clostridium* sp. and *Enterobacteriaceae* (Waldenstedt et al., 2003; Zhang et al., 2020).
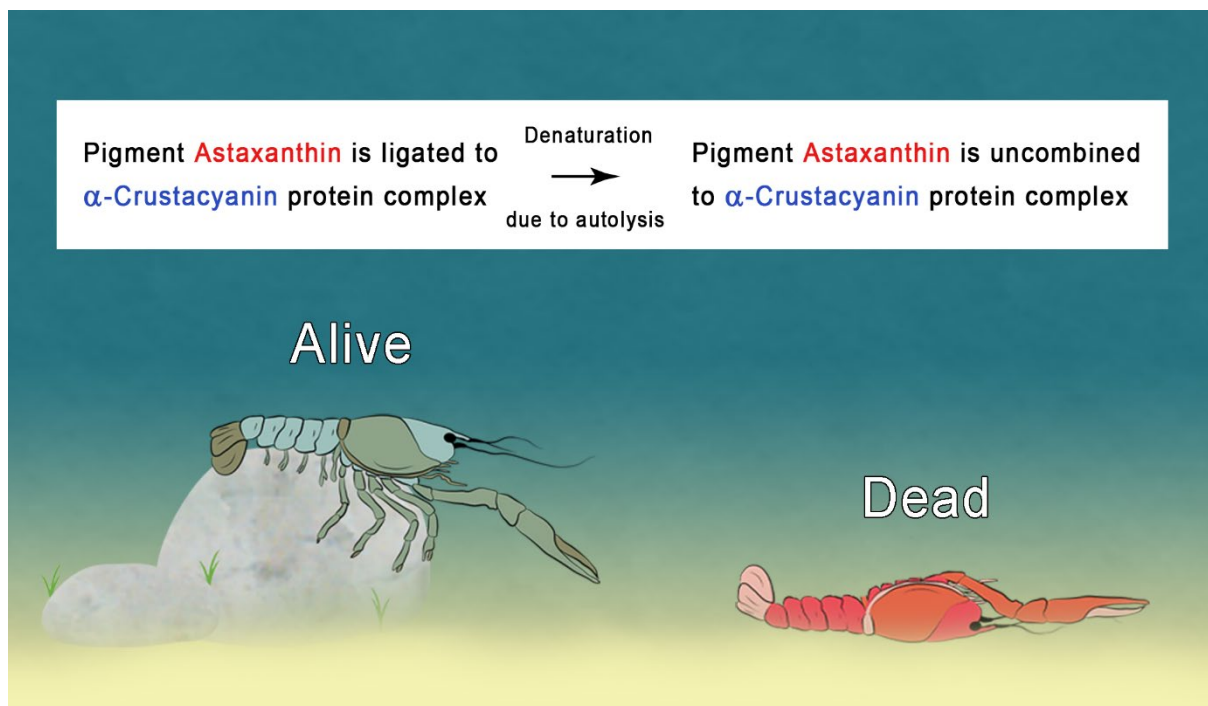
FIGURE 4. Sketch with a short explanation why crayfish individuals change their coloration after death. Living crayfish individual sitting on a stone. The living crayfish is blue-green in colour because of the ligation of Astaxanthin to the α-crustacyanin protein complex. The dead crayfish individual with red coloration is lying on its dorsal side at the bottom of a lake. The pigment Astaxanthin is uncombined to the α-crustacyanin protein complex, caused by autolytic processes.

1.2.6 Moulting cycle in crayfish

Caused by the calcified exoskeleton crayfish have to pass four main stages of a moulting cycle for growing. (i) Intermoult, (ii) premoult, (iii) moult, and (iv) postmoult phase. Most of their lifetime adult crayfish individuals spend their time in the intermoult phase (**Figure 5.1**), in which the three first cuticle layers (epi-, exo-, and endocuticle) are complete and calcified (Roer and Dillaman, 1984). During the premoult phase the calcified cuticle layers were separated from the epidermal layer (Bade and Stinson, 1978) and new epicuticle and exocuticle are build but not calcified until after the moult (Travis, 1963). Further on, minerals as well as organic substances were reabsorbed from the old cuticle layers (Drach, 1939). During the resorption calcium ions are dissolved out of the cuticle layers of the carapace and transported via the haemolymphatic circulatory system to the stomach (Ahearn et al., 2004). Inside the gastrolith cavity located inside the cardiac stomach wall (two anterior lateral specific discoid areas of the monolayered epithelium) (Shechter et al., 2008), $CaCO_3$ solidifies as amorphous calcium carbonate (ACC) under basic conditions to form gastroliths (Travis, 1960; Travis, 1963;

33

Luquet, 2013) which are separated from digestive secretions by a cuticular lining (Ueno and Mizuhira, 1983) (**Figure 5.2**).

After the moulting (**Figure 5.3 and 5.4**) gastroliths drop into the gastric lumen where they are digested and calcium ions can be reabsorbed (Ueno and Mizuhira, 1983) and the epicuticle and exocuticle are calcified. Simultaneously a new endocuticle is build up and calcified, whereby the calcification is not a homogenous distribution and can vary within and between species (Waugh et al., 2009).
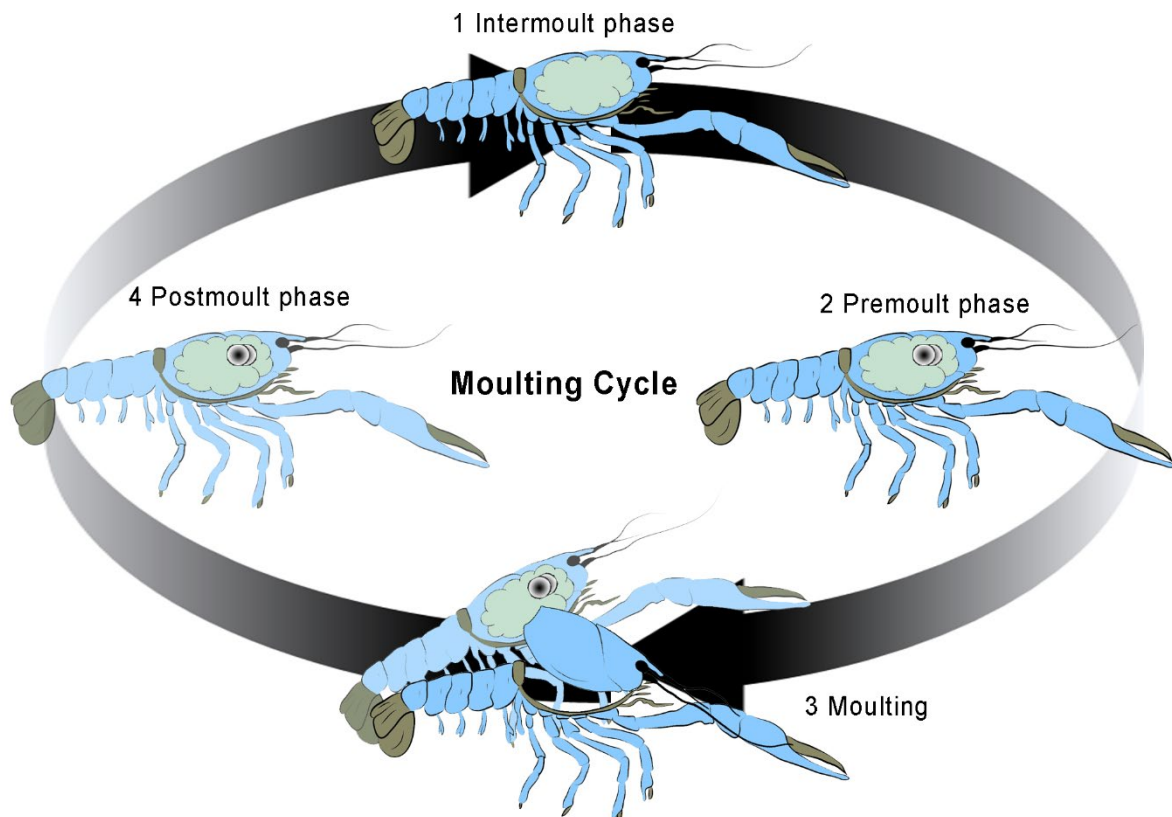
FIGURE 5. Moulting cycle of the freshwater crayfish *C. diminutus*. **5.1** Individual with completely hardened cuticle during the intermoult phase. **5.2** Individual with one pair of gastroliths inside the stomach during the premoult phase. **5.3** Crayfish individual is slipping out of the old cuticle during the moulting. **5.4** Individual with a not fully hardened cuticle right after the moulting.

1.3 Applied methods

1.3.1 Micro-Computed Tomography (μ-CT)

Micro-computed tomography is an X-ray based analyzing technique, in which roentgen radiation is generated by an X-ray tube, transmitted through an object and recorded by an X-ray detector as a two-dimensional (2D) projection image. The object is rotated for a fraction of a degree and another image is taken. This step will be repeated through 360-degree turn. Afterwards, the image stack, which is composed out of X-ray projection images, will be computed into cross-sectional images and processed into a three-dimensional (3D) model containing volumetric information.

In the field of paleontology, more precisely in actuo-paleontological studies, virtual autopsy using a μ-CT device is used for the observation of body interior changes in carcasses during the decomposition in time. This method is called 4D-virtopsy, in which time is the fourth dimension (Mähler et al. 2015).

The first virtopsy controlled decomposition experiment was conducted by Schwermann et al. (2012) in an actuo-paleontological study of a dormouse. The same method was further used by Mähler et al. (2015) for the observation of body interior changes in mole carcasses during the decomposition under freshwater conditions.

1.3.2 Inductively Coupled Plasma Mass Spectrometry (ICPMS)

ICPMS is a sensitive element analyzing method, in which ionized argon gas is induced by a high-frequency current and a sample is heated up to several thousand degrees. The atoms are then ionized and a plasma is created. In the next step ions generated in the plasma are accelerated in the direction of the analyzer and the individual elements and their isotopes are metrological recorded (Lippold, 2022, March 24).

1.3.3 Confocal Raman Spectroscopy (CRS)

Raman spectroscopy is an analyzing method that is based on the interaction of light with the chemical bonds of a sample. By the help of this technique information about the molecular correlations, the degree of crystallization, the chemical structure and the current phase of the sample can be obtained. A high intensity source of laser light is used to induce a molecule so that it scatters a small amount of incident light with a different wavelength as the laser light. The wavelength is addicted to the chemical structure of the sample.

The Raman spectrum displays several peaks, that show the position of the wavelength and the intensity of the scattered light. Each peak is related to a specific vibration of a molecule bond. A confocal Raman spectroscope is a Raman device coupled with a microscope to analyze particles of micron size, to measure contaminations or chemical changes inside a sample, and to analyze different layers of a multi-layered sample (Plank, R., Cansiz, E., Urabe, H., Bode, M., Nagano, T., Nakamura, H. & Habe, T., 2022, March 24).

1.3.4 Scanning Electron Microscopy (SEM)

By SEM imaging a sample surface is scanned with a beam of electrons focused by magnetic coils inside a vacuum. The beam is scanning the surface in a raster in which the electrons of the beam interact with the atoms of the sample to get information of the topography. The scan signal is then transformed into a grey value information and simultaneously presented on the screen (Lippold, 2022, March 24).

Chapter 2

Published in *Biological Reviews*

<u>Title:</u> The complex role of microbial metabolic activity in fossilization

Authors: Janssen, K.*, **Mähler, B.***, Rust, J., Bierbaum, G. & McCoy, V.E.

*Authors contributed equally to this work.

Kathrin Janssen and *Bastian Mähler* wrote the main part of the article and were supported by *Victoria E. McCoy. Bastian Mähler* designed the figures.

Summary

The fossilization of soft tissues is a complex interplay between the processes of decay and mineralization (Briggs, 2003). Rapidly post-mortem endogenous enzymes start a process called autolysis that can influence the preservation or decomposition of tissues (Penning, 2006, Krause & Jachau, 2002). But the main drivers in decay and preservation of soft tissues are bacteria (Raff et al., 2008) and it is widely assumed that a successful fossilization of these tissues is correlated with anaerobic conditions (Parry et al., 2017), high pH-values and high salinity (Gäb et al., 2020), because these abiotic factors can inhibit bacterial activity. However, bacteria are highly divers and adapted their metabolic activity to extreme environments (Rampelotto, 2013), or bacteria like *Pseudoalteromonas tunicata* are able to adapt their metabolic pathways to the current oxygen level and changes their behavior (Raff et al., 2014). Further on, experimental studies conducted by Briggs & Kear (1993a) showed a higher preservation potential of soft tissues under anaerobic conditions than under aerobic. On the other hand, experiments on cnidarian tissues revealed that certain tissues were most likely preserved when oxygen is available (Hancy & Antcliffe, 2020). In conclusion, the preservation and later fossilization of soft tissues seems to be a complex interplay of abiotic factors, involved microorganisms and the tissue type.

Bacteria produce several exoenzymes that lead to decomposition and influences environmental conditions, which in turn can lead to mineralization (Hirschler et al., 1990). The two most important processes of bacterial mediated fossilization are biologically induced mineralization (BIM) and mineralization of organic matter, which normally works together. An example for BIM is the hydrolysis of urea by bacterial ureases, that leads to an increase of the pH-value and can result in a precipitation of calcium carbonate (Hammes & Verstraete, 2002). Preservation pathways that lead to pyritized tissues, as it is known from the Hunsrück Slate fossils serve as

a prominent example for a combination of BIM and mineralization of organic matter. The decomposition of organic material leads to the release of sulfate (Schoenen, 2019), that can be reduced to hydrogen sulfate by bacteria like *Desulfovibrio*, which then react further with iron from the environment via several intermediate stages to pyrite (Berner, 1970; 1984; Canfield & Raiswell, 1991). Bacteria are able to produce biofilms and microbial mats (complex type of biofilms) in which oxygen, pH-value, osmolarity and redox potential influence the microbial activity (Arp et al., 2012). If a dead organism is quickly enveloped by a biofilm or microbial mat the conditions around the carcass will change due to microbial activity and can lead to a precipitation of minerals and a replication of soft tissues (Iniesto et al., 2016). A preservation of soft body organisms by microbial mats is assumed for the well-preserved Ediacaran fossils and was prominent as the death mask model (Gehling, 1999). Gehling (1999) assumed that biofilms and microbial mats were ubiquitous on the seafloor in Ediacaran times and therefore dead organisms, which lay on the seafloor were quickly enveloped by microbial mats and preserved as casts and moulds.

To shed light on the processes that lead to fossilization, experimental studies on taphonomy are of great importance. A lot of fossil examples show, that these processes are more complex than previously thought and that general simple assumptions on the role of bacteria during the preservation of soft tissues are unable to explain the processes that lead to fossilization (e.g., (i) the preservation of certain cnidarian tissues under aerobic conditions (Hancy & Antcliffe, 2020), (ii) the formation of siderite concretions around jellyfish found at the Mazon Creek fossil site (Clements et al., 2019) and (iii) the preservation of arthropod nerve tissue found in many Cambrian fossils (Ma et al., 2012; 2015).

Chapter 3

Published in *Palaeontologia Electronica*

Title: Calcite precipitation forms crystal clusters and muscle mineralization during the decomposition of *Cambarellus diminutus* (Decapoda: Cambaridae) in freshwater.

Authors: **Mähler, B.**[*], Janssen, K., Menneken, M., Tahoun, M., Lagos, M., Bierbaum, G., Müller, C.E. & Rust, J.

*Corresponding author

Bastian Mähler designed the study and prepared the manuscript. He did analysis with µ-CT, SEM, ICPMS and virtual reconstruction. He also designed the figures (except Figure 7).

Kathrin Janssen wrote a part in the discussion about urea and bacteria.

Martina Menneken did CRS analysis, wrote the text parts and did figure 7.

Mariam Tahoun did AAS analysis and wrote the text parts.

Markus Lagos prepared the calibration solution and calibrated the device. *Bastian Mähler* prepared the sample solutions and did ICPMS analysis. *Markus Lagos* wrote the methods part and *Bastian Mähler* did the evaluation of the data.

Summary

The preservation of soft tissue is often the replacement of organic material by minerals (e.g., phosphates, carbonates and pyrite) (Briggs, 2003; Briggs et al., 2005; Briggs et al., 2011). Taphonomic experiments with shrimps (*Crangon crangon*) and prawns (*Palaemon elegans*) revealed that during the decomposition in artificial seawater muscle tissues were replaced by calcium phosphate in which the sole source of phosphate were the carcasses themselves (Briggs & Kear 1994; Sagemann et al., 1999). Beneath the soft tissue preservation calcium carbonate crystals precipitated inside the specimens (Briggs & Kear, 1993a) as it is known from several crustacean fossils (Briggs & Wilby, 1997). The study presented here was conducted with twenty dead individuals of the extant crayfish *Cambarellus diminutus* raised in our lab. Each specimen was placed in one sterile Falcon tube and fixed in place with synthetic filter floss. Afterwards, ten tubes were filled with tank water and ten tubes were filled with distilled water, then sealed and stored in an incubator at a constant temperature of 30°C for 11 days. The carapaces of each specimen changed its coloration from greenish-brown to red and appeared soft and jellylike

with progressive decay. Muscles shrank and became soft and crumbling. Observations with micro-computed tomography (μ-CT) of decomposing crayfish in tank water and distilled water over time showed an early diagenetic mineral precipitation of crystal clusters only at the inner side of the cuticle. With scanning electron microscopy (SEM), a crystal structure found inside the dactyl of the left chela of the first left pereiopod, could be identified as mineralized muscle tissue. Further analyses of the crystal structures and the muscle tissue by confocal Raman spectroscopy (CRS) revealed that the crystals and the muscle tissue consist of well-ordered calcite. Inductively coupled plasma mass spectrometry (ICPMS) of distilled water showed a calcium content below the detection limit at the beginning of the experiments, which indicates that the sole source of calcium, needed for the precipitation of calcite, were the carcasses themselves. Ten specimens used in this study were in one of the two moulting phases (premoult or postmoult) at the time of death. During this time calcium storages called gastroliths can be found inside the cardiac stomach wall (Shechter et al., 2008). Initially to each premoult phase calcium ions from the cuticle layers are dissolved out of the cuticle and transported via the haemolymphatic circulatory system to the stomach, where they precipitated as amorphous calcium carbonate (ACC) and form gastroliths (Travis, 1960). After ecdysis gastroliths were dissolved and calcium ions were transported via the haemolymphatic circulatory system to the fresh build cuticle layers for restabilization (Ueno & Mizuhira, 1983). Volume measurements of 3D reconstructed calcite clusters and gastroliths showed an increase of the total volume of calcite (TVC) and a simultaneously volume reduction of gastroliths with progressive decay. In addition, specimens which were in the premoult phase or intermoult phase showed a higher TVC than individuals that were in the postmoult phase. Measurements of the total amount of body calcium by atomic absorption spectrophotometry (AAS) revealed a lower amount of calcium inside individuals that contain gastroliths than in individuals without gastroliths. The results further show, that the higher the body size, the higher the volume of precipitated calcite, if the individuals were in the intermoult phase at the time of death. If the individuals were in the premoult phase or postmoult phase, the stage of each phase was important and the body size played a subordinated role. The mineralization of muscle tissue by calcite could only be noticed in one individual that was in the intermoult phase. Whether the absence of gastroliths favors the mineralization of muscle tissue has to be proven in further experiments.

Chapter 4

Review in progress *Scientific Reports*:

<u>Title:</u> Adipocere formation in biofilms as a first step in soft tissue preservation

Authors: **Mähler, B.***, Janssen, K., Tahoun, M., Tomaschek, F., Schellhorn, R., Müller, C.E., Bierbaum, G. & Rust, J.

*Corresponding author

Bastian Mähler designed the study and prepared the manuscript. He did analysis with μ-CT, SEM, virtual reconstruction, took the photos, prepared the samples for further analysis with CRS, did general observation and dissections. He also designed Table 1 and the figures (except Figure 3.3, 5, 11 and 12, as well as Supplementary Figure S1 and S2).

Kathrin Janssen did DNA extraction, 16S rRNA gene amplicon sequencing wrote the text parts and designed Figure 5.

Mariam Tahoun did HPLC-UV/MS analysis, wrote the text parts and designed Table S1, Figure 11 and 12, as well as Supplementary Figure S1 and S2.

Frank Tomaschek did CRS analysis, wrote the text parts and designed Figure 3.3.

4.1 Introduction

In aquatic environments, dead organisms are often covered by biofilms (Briggs, 2003). The effects of microbial activity on fossilization processes are still being investigated. Taphonomic studies under laboratory conditions revealed various pathways how bacteria can influence the decomposition and lead to preservation (Briggs & Kear, 1994; Sagemann et al., 1999). The preservation of soft tissues (e.g., muscles) occurs in form of pseudomorphs, in which the original muscle tissue is replaced by calcium phosphate ($CaPO_4$) (Briggs & Kear, 1993a; 1994; Hof & Briggs, 1997; Sagemann et al., 1999), or calcite (Mähler et al., 2020). In a recent experiment, the midbrain of a frog, that had been placed on a microbial mat was replaced by calcium carbonate ($CaCO_3$) after 1.5 years (Iniesto et al., 2017). In other studies, the hepatopancreases (digestive glands) of the shrimps *Crangon crangon* and *Neogonodactylus oerstedii* were mineralized by $CaPO_4$ (Briggs & Kear, 1993a; 1994; Hof & Briggs, 1997). Briggs and Kear (1993a) even assumed that the mineralization was initiated in the hepatopancreas. Taphonomic experiments have shown that these mineralization processes are early diagenetic and dynamic, because tissue mineralized by $CaPO_4$ can be covered by $CaCO_3$ crystals if the pH switches to more alkaline conditions (Briggs & Kear, 1994; Wilby & Briggs,

1997). In addition, the pH-values in a decaying carcass might vary in different parts of the organism and result in the precipitation of various minerals (e.g., apatite, calcite, aragonite) in the same carcass (Wilby & Briggs, 1997) or lead to the dissolution of minerals (e.g., amorphous calcium carbonate) (Mähler et al., 2020). For example, the fossils of the crustacean-like specimen *Dollocaris ingens* from the Jurassic Konservat-Lagerstätte of La Voulte-sur-Rhône in France show a variation of different minerals inside the body cavity (Jauvion et al., 2020).

In this study we describe the transformation of the hepatopancreas of *Cambarellus diminutus* into adipocere only inside a biofilm. Adipocere is the result of incomplete hydrolysis of fat in animal tissue by bacteria under mainly anaerobic conditions (Schoenen & Schoenen, 2013). Caused by the ability of adipocere to slow down or inhibit decay processes (Forbes et al., 2005) it has been suggested as a key component in the outstanding preservation of fossils in Konservat-Lagerstätten like Messel, Holzmaden (Schwermann et al., 2012) or Solnhofen (Reisdorf & Wuttke, 2012). It is also assumed, that adipocere formation preceded the phosphatization of insects discovered at Quercy (France) as a shaping component (Flach, 1980). Berner (1968) as well hypothesized, that well-preserved fossils in calcium carbonate ($CaCO_3$) concretions may have formed originally as adipocere, which was later converted into $CaCO_3$.

4.2 Material and methods

Individuals of the extant crayfish *Cambarellus diminutus* were taken from a settled tank community raised in our lab. The animals were kept in 54 L tanks of 60 x 30 x 30 cm in size, at a constant water temperature of 26°C. Tanks were filled with pipe water and fortified with "Biotopol C" water conditioner (JBL, GmbH & Co. KG, Neuhofen, Germany) to neutralize zinc (Zn) and lead (Pb) and to remove chlorine (Cl) and bind copper (Cu). The crayfish were fed with nothing but "Crab Natural" (Sera, GmbH, Heinsberg, Germany), a main food for crayfish (ingredients can be found in **Supplement 1**).

Thirteen individuals with partly filled guts, were sacrificed by placing them in an atmosphere of carbon dioxide (CO_2). Specimens were not dried before weighing them on a micro scale. Lengths were measured from the anterior tip of the cephalothorax to the end of the abdomen without the telson (**Table 1**).

TABLE 1. Specimen information

sample	wet weight	body size	sample	wet weight	body size
C1	0.26 g	2.50 cm	C8	0.28 g	1.80 cm
C2	0.17 g	1.80 cm	C9	0.22 g	1.80 cm
C3	0.42 g	2.10 cm	C10	0.13 g	1.70 cm
C4	0.37 g	1.90 cm	C11	0.43 g	2.40 cm
C5	0.32 g	2.10 cm	C12	0.34 g	2.00 cm
C6	0.34 g	2.10 cm	C13	0.32 g	2.10 cm
C7	0.30 g	2.30 cm	-	-	-

At the beginning of each experiment oxygen saturation and pH-value were measured with an oxygen probe, OXPB-11 and pH-meter, PCE-PHD 1 (both PCE Deutschland GmbH, Meschede, Germany). Images of decomposing crayfish were taken by an i-Phone 12 mini. Images have 4032 x 3024 pixel and 24 bit with an exposure time of 1/50 sec. The hepatopancreases (digestive glands) of sample C4 and C8 were lying in tank water at room temperature when they were photographed by using a stereomicroscope (Stemi 2000, Carl Zeiss Microscopy Deutschland GmbH, Oberkochen, Germany) combined with an iPhone 12 mini holding by a Gosky Universal Digiscoping Smartphone Adapter, FBA_QHAPO21 (Gosky-optics, USA). The image of the calcite conglomerate in Figure 4.1 was photographed with a stereo-zoom-microscope (Axio Zoom. V16, Carl Zeiss Microscopy Deutschland, Oberkochen, Germany). Final figures were created by using Adobe Photoshop CS5 (Adobe, Dublin, Republic of Ireland) with 300 dpi.

Experiment 1

The first experiment was conducted twice with first 3 and secondly 4 dead crayfish samples (C1 to C7) that were placed on artificial sediment inside a 54 L tank (tank 1) filled with pipe water and fortified with "Biotopol C" water conditioner, under a constant water temperature of 28°C for a duration of 9 days. The pH of the water was 8 and had an oxygen saturation of 8 mg/L. In order to obtain a suitable biofilm, a piece of the crab food "Crab Natural" was placed next to the dead individuals. This was done because it was observed that food rings have the potential to induce biofilms. Individuals were photographed once per day.

After 9 days, crayfish remains were removed from the tank and analyzed by using a stereomicroscope. In addition, crayfish remains were scanned by using a μ-CT device, if possible.

Experiment 2

The second experiment was conducted with 3 crayfish individuals (C8 to C10) after experiment 1 inside the same tank (tank 1) and water under a constant water temperature of 28°C for a duration of 8 days. The pH of the water was 8 with an oxygen saturation of 8 mg/L. The individuals were photographed once per day and after 8 days, crayfish remains were analyzed by using a stereomicroscope. Contrary to experiment 1, the water was colonized by a large number of ostracods (**Figure 1**), which had been introduced by the crab food used in experiment 1.
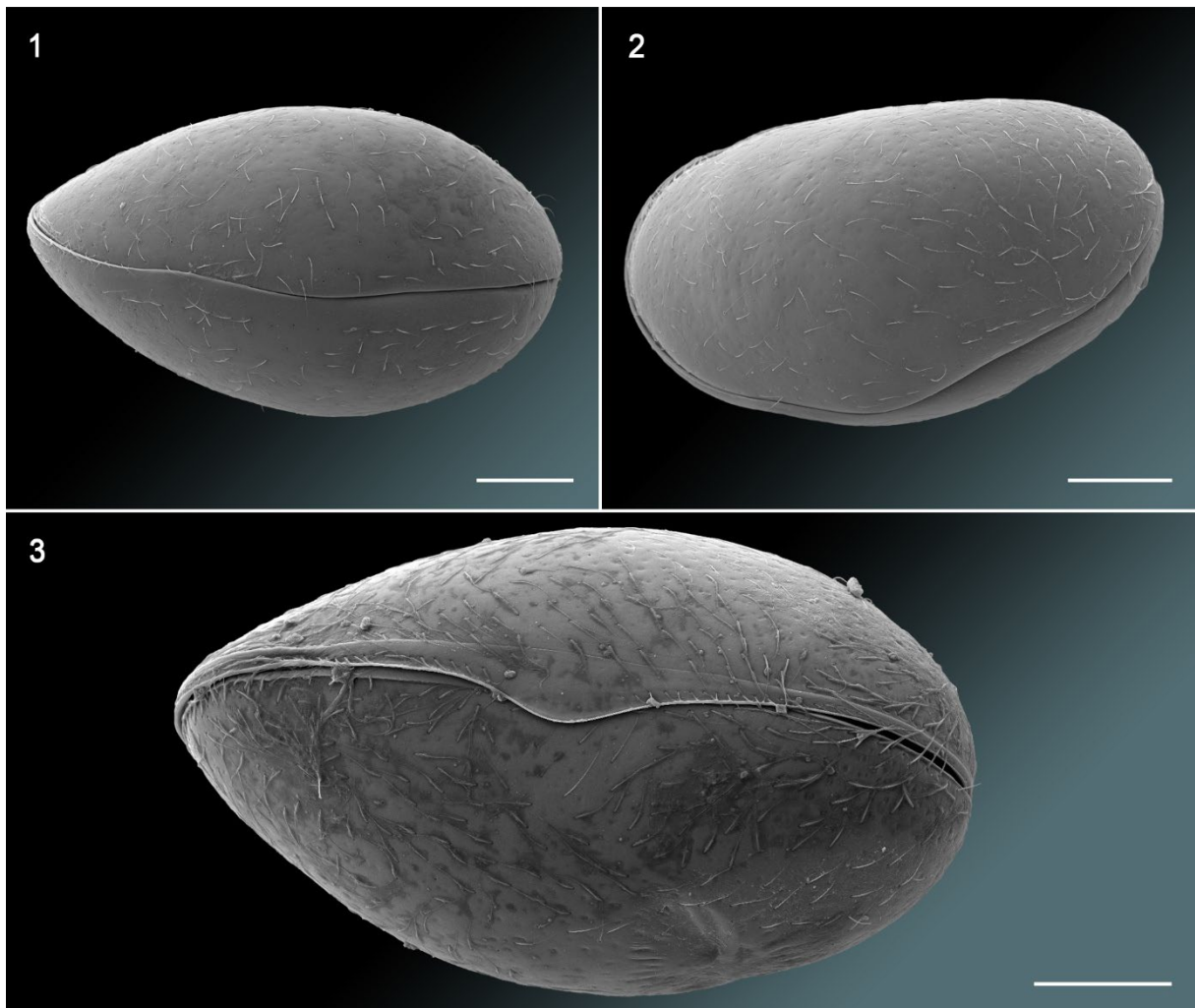
FIGURE 1. SEM-images of ostracods found on decomposing crayfish samples and biofilms. *Scale bar* 100 µm.

Experiment 3

In the third experiment crayfish individuals C11 to C13 were placed inside another tank (tank 2) filled with pipe water, which was also fortified with "Biotopol C" water conditioner. The experiment was conducted under a constant water temperature of 28°C for a duration of 7 days. The pH of the water was 8 with an oxygen saturation of 8 mg/L. The water was free from ostracods and no crab food was add to the experiment. Afterwards, the crayfish remains were removed from the tank and analyzed by stereomicroscopy.

At the beginning of each experiment carcasses were fully articulated and blue in color. In addition, no symbiotic, parasitic or commensally organisms were found on the carcasses.

DNA extraction

DNA was extracted from the biofilm with the ZymoBIOMICS DNA/RNA Miniprep Kit (Zymo Research, Irvine, USA). Biofilm samples of C1, C2 and C4 were transferred into ZR BashingBead™ Lysis Tubes (0.1 & 0.5 mm) with 750 µL ZymoBIOMICS Lysis solution. Bead beating was performed with a Precellys® homogenizer (Bertin Technologies S.A.S., Montigny Le Bretonneux, FR), 6000 x g for 30 s. Samples were subsequently processed according to the manufacturer's instructions. DNA was eluted in 50 µL DNase/RNase-free water and DNA concentration and quality was checked using a NanoDrop One/OneC Microvolume-UV/VIS-spectrophotometer (Thermo Fisher Scientific, Waltham, Massachusetts, USA).

16S rRNA Gene Amplicon Sequencing

For 16S rRNA gene sequencing, the V4 variable region of the 16S rRNA gene sequence was amplified with the specific 16S primers of 16S-515F (GTG CCA GCM GCC GCG GTA A) and 16S-806R (GGA CTA CVS GGG TAT CTA AT) (Caporaso et al., 2011). Fungal ITS-region was amplified with specific ITS-primers (for: CTT GGT CAT TTA GAG GAA GTA A rev: GCT GCG TTC TTC ATC GAT GC). The PCR reaction was performed as a single-step PCR with the HotStarTaq Plus Master Mix Kit (Qiagen, USA) including an initial denaturation at 95°C for 5 min, followed by 30–35 cycles of 95°C for 30 s, 53°C for 40 s, and 72°C for 1 min, with a final elongation step at 72°C for 10 min. Paired end sequencing (bTEFAP®) was performed by MR DNA (www.mrdnalab.com, Shallowater, TX, USA) on a MiSeq following the manufacturer's guidelines (Dowd et al., 2018). Raw sequence data was processed via the QIIME2 pipeline (Boylen et al., 2019) with default parameters unless otherwise noted. DADA2 pipeline was used for sequence quality control, denoising and chimeric filtering (Callahan et al., 2016). Taxonomy classification of the final bacterial ASVs (amplicon sequencing variant),

clustered at 99 % identity, was performed with a naive Bayesian classifier which was trained against SILVA database release 138 especially for 515F/806R rRNA region (Bokulich et al., 2018; Quast et al., 2012). ASVs of fungal composition analysis were aligned to a curated database derived from NCBI which was performed by the sequencing facility. For prediction of metabolic characteristics of the bacteria, the sequences were taxonomically classified with the Greengenes database (McDonald et al., 2012). The allocation of the phenotypes was then performed with BugBase (Ward et al., 2017).

All raw sequence data related to this study are deposited in the European Nucleotide Archive (ENA) (European Bioinformatics Institute, EMBL-EBI) database a collaboration partner of the International Nucleotide Sequence Database (INSD), [Study-Accession Number: PRJEB43756].

Micro-Computed Tomography (μ-CT)

The propodus of the right chela of sample C4 and the complete carcasses of sample C1, C2 and C6 were removed from the tank and were scanned by using a phoenix|x-ray v|tomex s 240 micro-computed-tomography scanner (GE Measurement & Control, Wunstorf, Germany) located at the Institute of Geosciences of the University of Bonn. The data set has a resolution of 12.66 μm; the scans were carried out at 80 kV and 100 μA. Three frames per projection were acquired by a timing of 500 ms for a total of 1000 projections. The CT data were processed using the software VG Studio Max 3.2 (Volume Graphics, Heidelberg, Germany) and Avizo 8.1 (Thermo Fisher Scientific, Schwerte, Germany) to reconstruct and visualize the precipitated crystal clusters inside the specimens and specimen remains.

Confocal Raman Spectroscopy (CRS)

Cambarellus diminutus hepatopancreas samples and reference materials as well as crystal clusters were analyzed using a Horiba Scientific LabRam HR800 (located at the Institute of Geosciences, University of Bonn). Raman scattering was excited with a 784 nm diode laser as excitation source. The spectrometer was calibrated with the first-order Si Raman band at 520.7 cm^{-1}. Data in the spectral region of 300 to 1800 cm^{-1} (hepatopancreas) and 100 to 1800 cm^{-1} (crystal clusters) were collected with a 100 x long working distance objective, a confocal hole size set to 1000 μm, spectrometer entrance slit size of 100 μm, and a grating of 600 grooves/mm. The exposure time was 42 min per window with 50 accumulations of 50 s for the hepatopancreas samples, and 4.2 min with 50 accumulations of 5 s for saturated fatty acid

reference materials, respectively. The exposure time for crystal clusters was 2 min with 4 accumulations of 30 s.

Scanning Electron Microscope (SEM)

The right propodus and the dactylus, as well as a part of the hepatopancreas of sample C4 and crystal clusters were dissected and coated by a thin layer of gold with a cool sputter coater (Cressington Sputter Coater 108 manual, Tescan GmbH, Dortmund, Germany). Samples were subsequently scanned with an 'environmental' scanning electron microscope (SEM) unit (TESCAN VEGA 4 LMU) by using the SE detector at 20 keV. Images have 1536 x 1331 pixel and 16 bit.

High Performance Liquid Chromatography Coupled to Ultraviolet and Mass Spectrometry Detection (HPLC-UV/MS)

Materials and analytical conditions

Measurements were performed on an Agilent 1260 Infinity HPLC coupled to an Agilent Infinity Lab LC/MSD single quadrupole mass spectrometer with an electrospray ion (ESI) source and a diode array UV detector (DAD-UV, 200-600 nm, Agilent Technologies Germany GmbH & Co. KG, Waldbronn, Germany). Chromatographic separation was performed on an EC 50/3 Nucleodur C18 Gravity column, 3 μm (Macherey-Nagel, Dueren, Germany). Standard solutions of palmitic acid, oleic acid, and stearic acid (Sigma Aldrich Chemie GmbH, Taufkirchen, Germany) were prepared in a 1:1 solution of dichloromethane/acetonitrile, and known amounts were added to a sample for confirmation of retention times. A triglyceride mixture containing glyceryl trimyristate as the main component (Sigma Aldrich Chemie GmbH, Taufkirchen, Germany) was employed as a further standard. All solvents used were HPLC grade. Mobile phase A consisted of methanol with 2 mmol/L ammonium acetate, and mobile phase B consisted of water with 2 mmol/L ammonium acetate. The run started with 50% A and 50% B for 1 min, followed by a gradient that reached 100 % of eluent A after 15 min. Then, the column was flushed for 10 min with 100 % of mobile phase A followed by 50% A and 50% B for 5 min before starting the next run. Positive and negative full scan MS was obtained from 100 to 1000 m/z. The column temperature was set at 40°C, the injection volume was 5 μl, and the flow rate was adjusted to 0.5 ml/min. Identification of the peaks was performed using the data analysis program of the OpenLab CDS 2.5 software (Agilent Technologies Germany GmbH & Co. KG, Waldbronn, Germany). The extracted ion chromatogram (EIC)

was used to evaluate peak areas and to provide a semi-quantitative estimate of the detected compounds.

Extraction of adipocere components

A part of the hepatopancreas of sample C4, taken approximately 9 days post-mortem and hypothesized to be adipocere based on its visual appearance, was extracted and analyzed by HPLC-(DAD-UV)-ESI-MS with the aim to identify the different fatty acid components of adipocere from the resulting chromatographic peaks and mass spectra. A 0.9 mg sample was extracted with 5 ml of dichloromethane to obtain the lipophilic constituents present. Then, aliquots were diluted 1:1 with acetonitrile and subsequently analyzed by HPLC-(DAD-UV)-ESI-MS. Equal volumes of sample were measured with and without adding a mixture of palmitic acid, stearic acid and oleic acid as reference compounds (final concentration of each fatty acid was 1 µmol/L). This standard addition technique was used for confirmation of the presence of the individual fatty acids and to identify possible matrix effects affecting their retention times.

4.3 Results

General Observations

Experiment 1

On day 1, specimens C1 to C7 were blue in color and articulated, lying with the lateral bodyside on the sediment (**Figure 2.1-4**). The cephalothorax of each individual had changed its coloration from blue to dark red-brown on day 2. In addition, a translucent to milky translucent biofilm had formed on the carcasses and the carcasses of samples C1, C3, C5 and C6 were twisted by about 90 degrees due to the formation of the biofilm (**Figure 2.1 and 2.3**). On day 3 the samples were completely covered by the biofilm (**Figure 2.1-4**). An accumulation of putrefaction gas could be noticed around the branchial area of samples C1 and C5, which resulted in a floating of the carcasses inside the biofilm, however, the biofilms held the carcasses to the ground (**Figure 2.1**). A gas accumulation could also be noticed in samples C2, C6 and C7 but was not sufficient to let the carcasses "float" inside the biofilm. On day 4 the carcasses of samples C1 and C5 had risen further within the biofilm, but were still fixed to the sediment. From day 5 to day 7 the gas accumulation increased and, in all samples, the abdominal muscles had changed their coloration from white to pink. On day 7, ostracods had populated the carcasses and had started to degrade the biofilms. Most of the biofilms were degraded on day 8 and ostracods started to feed on the carcasses. On day 9 nearly the complete inner organs of the carcasses had been consumed by the ostracods. In all samples the complete

hepatopancreases remained, which looked mineralized and were hard and crumbly (**Figure 3.1**). In addition, crystal clusters were found in all carcasses (**Figure 4**).

Experiment 2

On day 1, specimens C8 to C10 were blue in color and articulated, with the left half of the body lying on the sediment. The cephalothorax of the individuals had changed their color from blue to red on day 2, and sample C9 was floating at the water surface, this was probably caused by putrefaction gas, which accumulated at the branchial area. On day 3, a light white biofilm could be noticed around the cephalothorax of specimen C8 (**Figure 2.5**) and around the pleon of specimens C9 and C10, both lying on the ground. The abdominal muscles of each specimen had changed their coloration from white to pink. Cuticles of all individuals were completely red in color and ostracods had populated the carcasses. On day 4 organs inside the cephalothorax of sample C8 had been consumed up by the ostracods, except the hepatopancreas and the biofilms had been completely degraded (**Figure 2.5**). On day 5 nearly the whole carcass of sample C8 had been consumed by the ostracods and only the chelipeds without any tissue inside as well as the hepatopancreas were left over (**Figure 2.5**). The anterior part of the cephalothorax of samples C9 and C10 were degraded and gastroliths of sample C9 were exposed. On day 8 nearly the complete carcasses of samples C9 and C10 had been consumed by the ostracods and only the hepatopancreases of both samples and the gastroliths of sample C9 remained. The hepatopancreas of all samples were slightly yellow, soft and fragile.

Experiment 3

On day 1, specimens C11 to C13 were blue in color and articulated, with the left half of the body lying on the sediment. With progressive decay cuticles became translucent, reddish and the muscles were pink (**Figure 2.6**). On day 7 internal organs had been mostly decomposed except the intestine and ganglia. Hepatopancreases could not be detected. In addition, muscles were pulpy and the cuticles of the cephalothorax and pleon were soft and jellylike. The chelipeds were still solid after 7 days. During the whole time, biofilm formation could not be detected and no gas accumulation occurred at the branchial area. The individuals were still articulated at the end of the experiment but ruptured at the transition from the cephalothorax to the pleon and the legs disarticulated quickly during the attempt to move them out of the tank.

FIGURE 2. Decomposing crayfish individuals of three different experimental setups lying on artificial sediment at a constant water temperature of 28°C. **2.1** <u>Day 1</u> Dead articulated crayfish sample C1, lying on its right body side in tank water. <u>Day 2</u> Dead crayfish was moved by the development of a biofilm and the cephalothorax had changed its coloration from blue to red-brown. <u>Day 3-7</u> Envelopment of the carcass by a biofilm with some slimy structures (blue arrow) and gas accumulation at the branchial area (green arrows), resulting in a "floating" carcass inside the biofilm. **2.2** <u>Day 1</u> Dead articulated crayfish sample C2, lying on its right body side in tank water. <u>Day 2</u> Development of a biofilm around the cephalothorax, which had changed its coloration from blue to red-brown. <u>Days 3 - 7</u> Envelopment of the carcass by a biofilm and gas accumulation at the branchial area (green arrow), resulting in a light "floating" carcass inside the biofilm. **2.3** Crayfish sample C3 lying in tank water for a duration of nine days. <u>Day 1</u> Dead articulated, blue crayfish lying on its right body side. <u>Day 2</u> Cephalothorax had changed its coloration from blue to red-brown and is covered by a light, white biofilm. <u>Day 3</u> The complete carcass was covered by a white biofilm and abdominal muscles had changed their coloration from white to pink. <u>Days 6 - 9</u> Biofilm population by ostracods and its complete degradation. <u>Day 9</u> Degraded cuticle of the pleon and some remains of the branchiae. **2.4** Crayfish sample C4 in tank water for a duration of nine days. <u>Day 1</u> Dead articulated, blue crayfish lying on its left body side. <u>Day 2</u> Cephalothorax had changed its coloration from blue to red-brown and is covered by a light, white biofilm. <u>Day 3</u> The complete carcass was covered by a white biofilm and abdominal muscles had changed their coloration from white to pink. <u>Days 6 - 9</u> Biofilm population by ostracods and its degradation. <u>Day 9</u> Remains of the biofilm and degraded cuticle. Chelipeds still intact and filled with pulpy muscles. **2.5** Crayfish sample C8 in tank water for a duration of five days. <u>Day 1</u> Dead articulated, blue crayfish lying on its left body side. <u>Day 2</u> Cephalothorax had changed its coloration from blue to red. <u>Day 3</u> The cephalothorax was covered by a white biofilm and abdominal muscles had changed their coloration form white to pink. <u>Day 4</u> Carcass was populated by ostracods and the biofilm was completely degraded. <u>Day 5</u> Only empty chelipeds and the hepatopancreas were left. **2.6** Crayfish sample C11 lying in tank water for a duration of seven days. <u>Days 1 – 7</u> Decomposing crayfish lying on its left bodyside. Cuticles of the cephalothorax and the pleon became light red and translucent. Muscles were pink in color. Individuals were still articulated at day 7. All *scale bars*: 1 cm except the *scale bars* of the last two pictures in 2.5 on day 5 which is 0.5 cm.
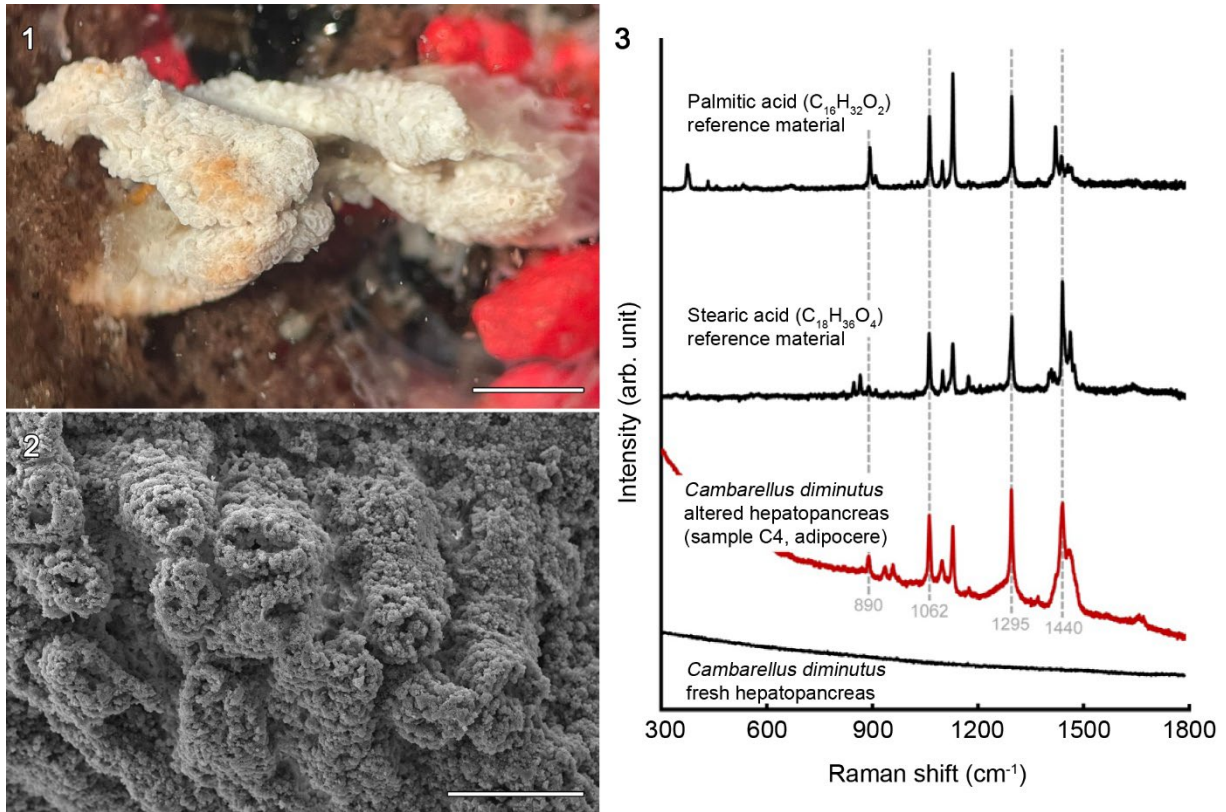
FIGURE 3. Images of the hepatopancreas (digestive gland) of crayfish sample C4 after nine days in tank water covered by a biofilm and Raman spectra. **3.1** Stereomicroscopic image of the hepatopancreas in water. *Scale bar* 1 mm **3.2** SEM-image of an enhanced part of the dried hepatopancreas. *Scale bar* 200 μm. **3.3** Representative Raman spectra of an altered *Cambarellus diminutus* hepatopancreas (sample C4, adipocere), reference data for saturated fatty acids (stearic and palmitic acids), and the hepatopancreas of a freshly killed *C. diminutus*. Raman bands typical for saturated fatty acids have developed post-mortem.
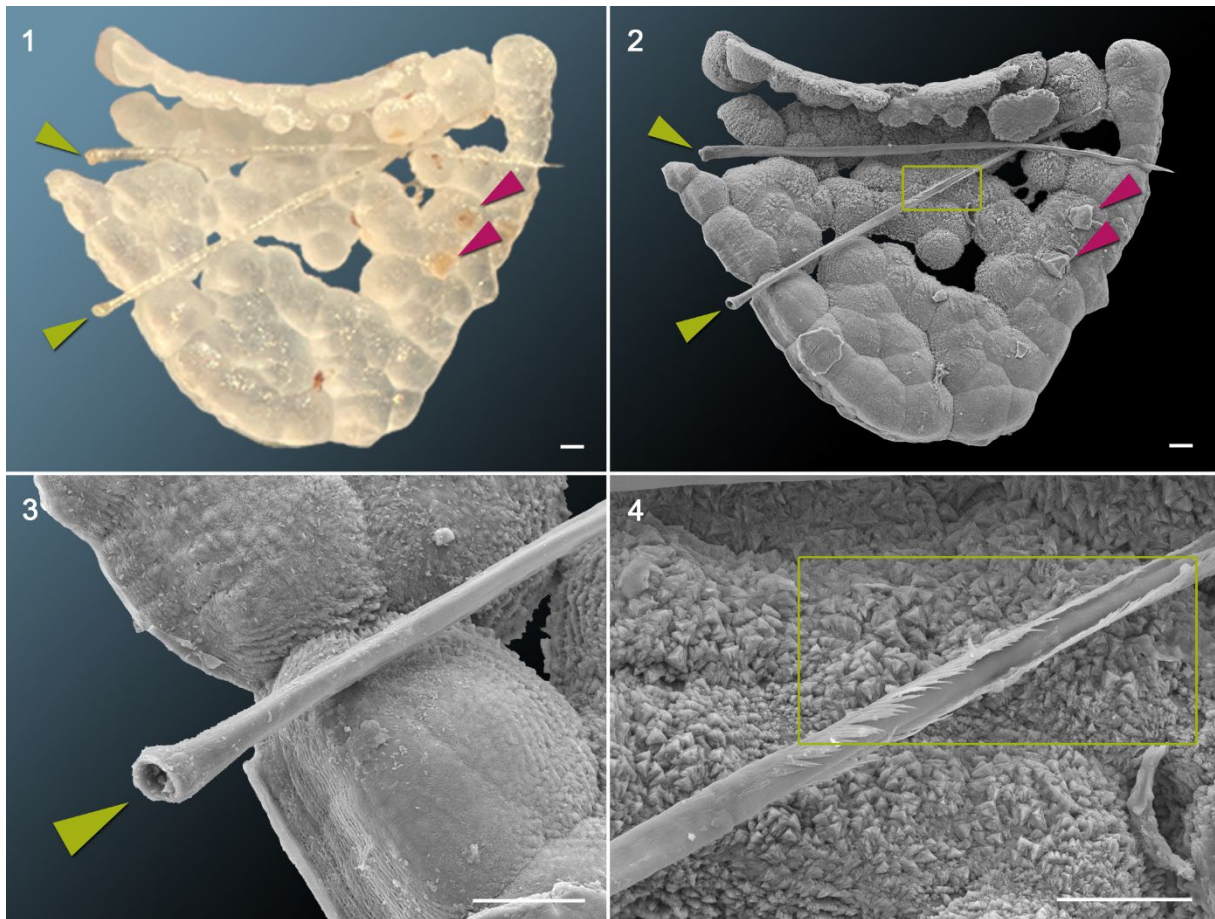
FIGURE 4. A calcite conglomerate of crayfish sample C4 **4.1** A stereomicroscopic image of a calcite conglomerate with two calcified setae (green arrows) and calcified cuticle remains (purple arrows). *Scale bar* 100 μm. **4.2** SEM-image of the conglomerate shown in 4.1 with two complete calcified setae (green arrows) and calcified cuticle remains (purple arrows). *Scale bar* 100 μm. **4.3** and **4.4** SEM-images show parts of a complete calcified seta. *Scale bars* 50 μm.

16S rRNA Gene Amplicon Sequencing

The 16S rRNA and ITS amplicon analyses of C1, C2 and C4 revealed that bacteria of the phyla γ-Proteobacteria, α-Proteobacteria, Bacteroidetes, and the class Clostridia were present in the biofilm. In particular, the samples were mainly composed of Gram-negative genera, such as *Sphaerotilus, Azospirillum, Hydrogenophaga,* or *Novispirillum* (**Figure 5.1**). In addition, the fungal colonization was almost completely dominated by species of the genus *Pluteus* (**Figure 5.2**). Further on, almost all bacterial individuals exhibited biofilm forming ability in a bioinformatic analysis with the prediction tool BugBase (**Figure 5.3**).
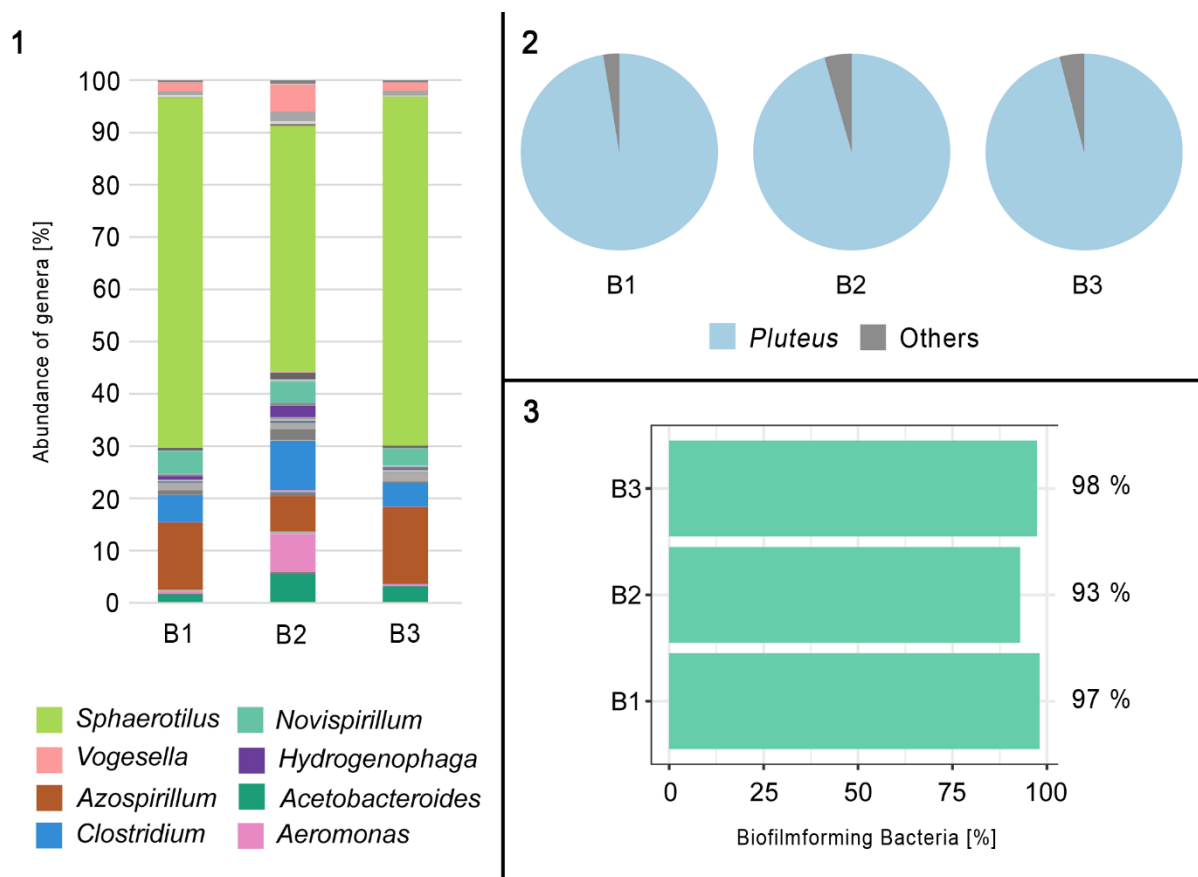
FIGURE 5. Microbial community composition of three biofilm samples taken from experiment 1 (B1 = C1; B2 = C2 and B3 = C4) **5.1** Abundance of bacterial genera (%). **5.2** Composition of fungal genera, which was dominated by the genus *Pluteus*. **5.3** Comparison of predicted biofilm forming ability of the bacteria detected in the three biofilm samples.

Micro-Computed Tomography (μ-CT)

In contrast to coarse-grained calcite precipitations which occur in decomposing crayfish without a biofilm (**Figure 6.2 and 6.5**), μ-CT observations of the chela of sample C4 and the complete carcasses of samples C1, C2 and C6 revealed a precipitation of fine-grained crystal structures mostly inside the cuticle but also inside the pereiopods and chelipeds (**Figure 6.3-4**).
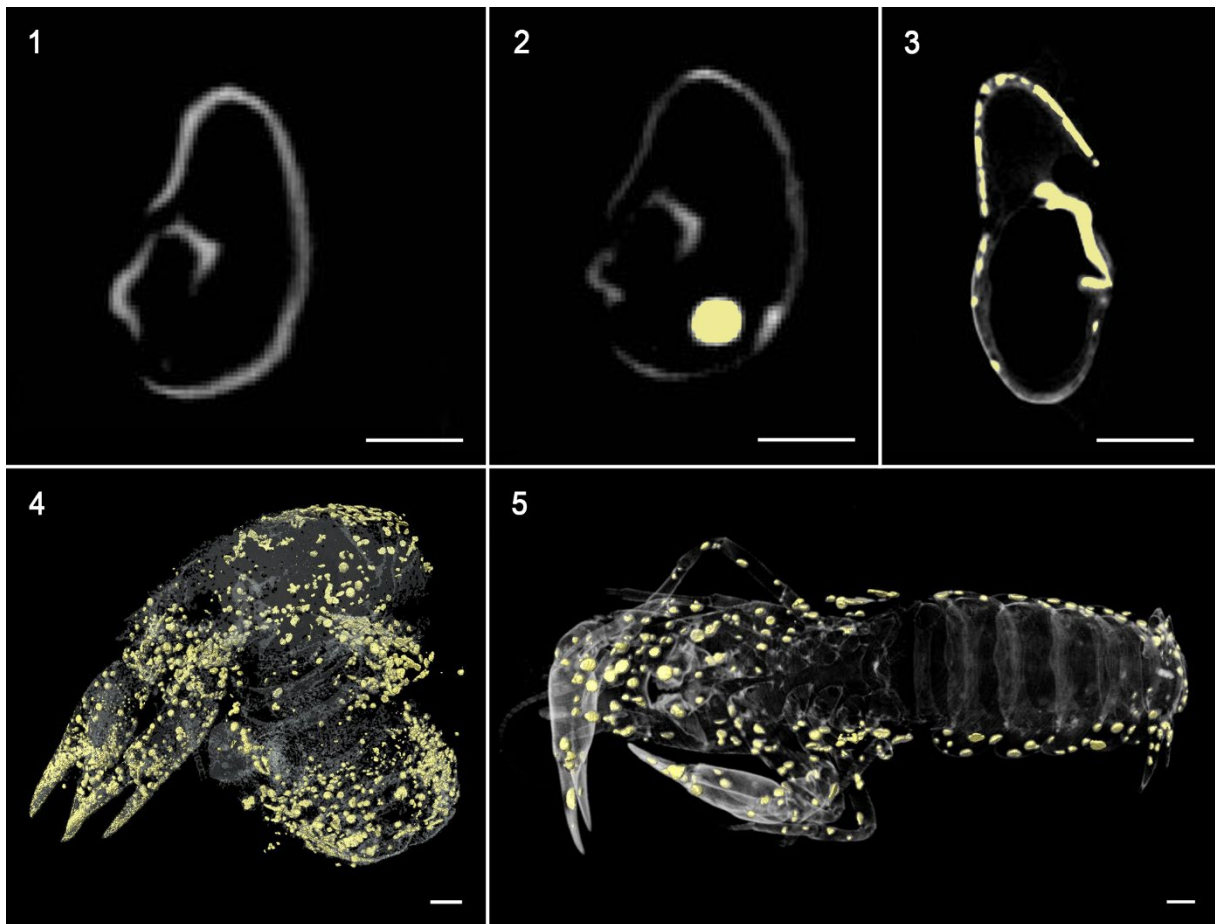
FIGURE 6. μ-CT images and 3D models of crayfish individuals and precipitated crystal clusters. **6.1** μ-CT image of a cross section of the right chela of an individual of *Cambarellus diminutus* (C7$_{tank}$) in tank water of an experiment described in Mähler et al. (2020) on day 1, with calcified cuticle. **6.2** The same chela as in 6.1 on day 7 with less calcified cuticle and a crystal cluster (yellow spot). **6.3** μ-CT image of a cross section of the left chela of C4 on day 9 with recrystallized cuticle (yellow structures). **6.4** Translucent 3D-model of C6 on day 9 with 3D-models of precipitated clusters (yellow spots). **6.5** Translucent 3D-model of an individual of *C. diminutus* (C7$_{tank}$) in tank water of an experiment described in Mähler et al. (2020) on day 7 with 3D-models of precipitated clusters (yellow spots). *Scale bars* 1 mm.

Confocal Raman Spectroscopy (CRS)

Raman spectra were obtained for an altered *C. diminutus* hepatopancreas (sample C4, adipocere) and saturated fatty acid reference materials (solid stearic and palmitic acids). All strong Raman bands obtained for sample C4 (at 890, 1062, 1098, 1128, 1295, 1440, and 1460 cm^{-1}) are typical for Raman spectra of saturated fatty acids (De Gelder et al., 2007; Allen et al., 2018) (**Figure 3.3**). In addition, there are unassigned bands at 935 and 958 cm^{-1}, and a broad shoulder around ~1250 cm^{-1}, which may point to the presence of some additional compound(s). It was also observed, that none of the Raman-active bands could be detected in a fresh hepatopancreas, indicating that saturated fatty acids must have formed post mortem.

Raman analyses clearly revealed that the crystal clusters consist of well-ordered calcite (**Figure 7)**, which can be identified by the fully symmetric $v_1(CO_3)$ carbonate band near 1085 cm^{-1}, as well as the presence of lattice vibrations near 154 and 281 cm^{-1}, with the latter being absent in amorphous calcium carbonate (ACC). A mixed spectrum of crystalline calcite and the β-carotene, astaxanthin (AXT) could be identified at calcified cuticle remains on the clusters (**Figure 7**) by the typical high intensity modes at ~1157 and ~1517 cm^{-1} that are assigned to the C=C and C-C stretching vibrations of the polyene chain bonds, respectively (Kaczor & Baranska, 2011; Subramanian et al., 2014; Saito & Tasumi, 1983). In comparison to the spectrum obtained from the AXT standard, a small derivation in the frequency of the ~1517 cm^{-1} signal was observed. Such a shift can presumably be linked to the structural differences of AXT.
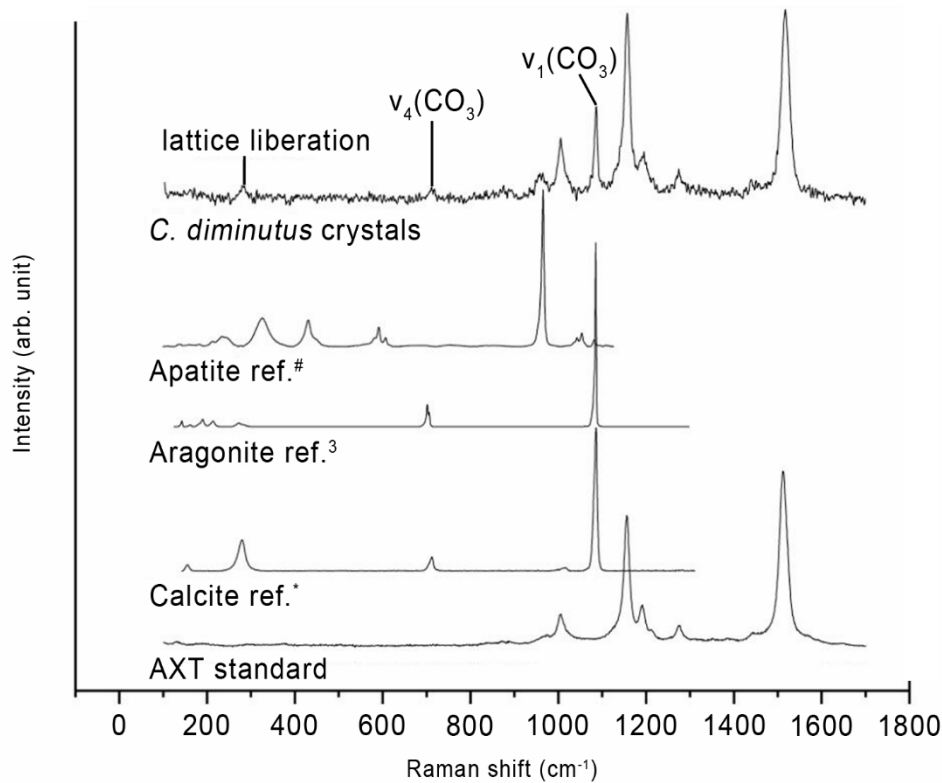
FIGURE 7. Representative Raman spectra of observed crystal clusters compared to Raman reference spectra of crystalline apatite, aragonite and calcite, taken from the RRUFF Raman data base ([#]R060070, [°]R060070, [*]R040170 Laetsch & Downs, 2006). Raman spectra of the crystal clusters exhibit main Raman bands typically for crystallized calcite and the β-carotene, astaxanthin.

Scanning Electron Microscopy (SEM)

SEM analyses of the thoracic skeleton reveal the presence of fungi inside the biofilm (**Figure 8**). Crystal clusters of C1 to C7 varying in size from ~100 μm to ~200 μm with the largest conglomerate measuring 1200 μm (**Figure 4**) at the end of the experiment. Most of the structures were spherical or bispherical (**Figure 9**). The largest structure presented a conglomerate of layered calcite structures combined with calcite bundles and two perfectly mineralized setae found between the pulpy remains of sample C4 (**Figure 4.2-3**). The dactylus of the right chela of sample C4 showed a lot of calcite clusters instead of the original cuticle (**Figure 10.2 and 10.4**). SEM images of the hepatopancreas of sample C4 showed in contrast to crystalline structures a pattern resembling to cauliflower (**Figure 3.2**).
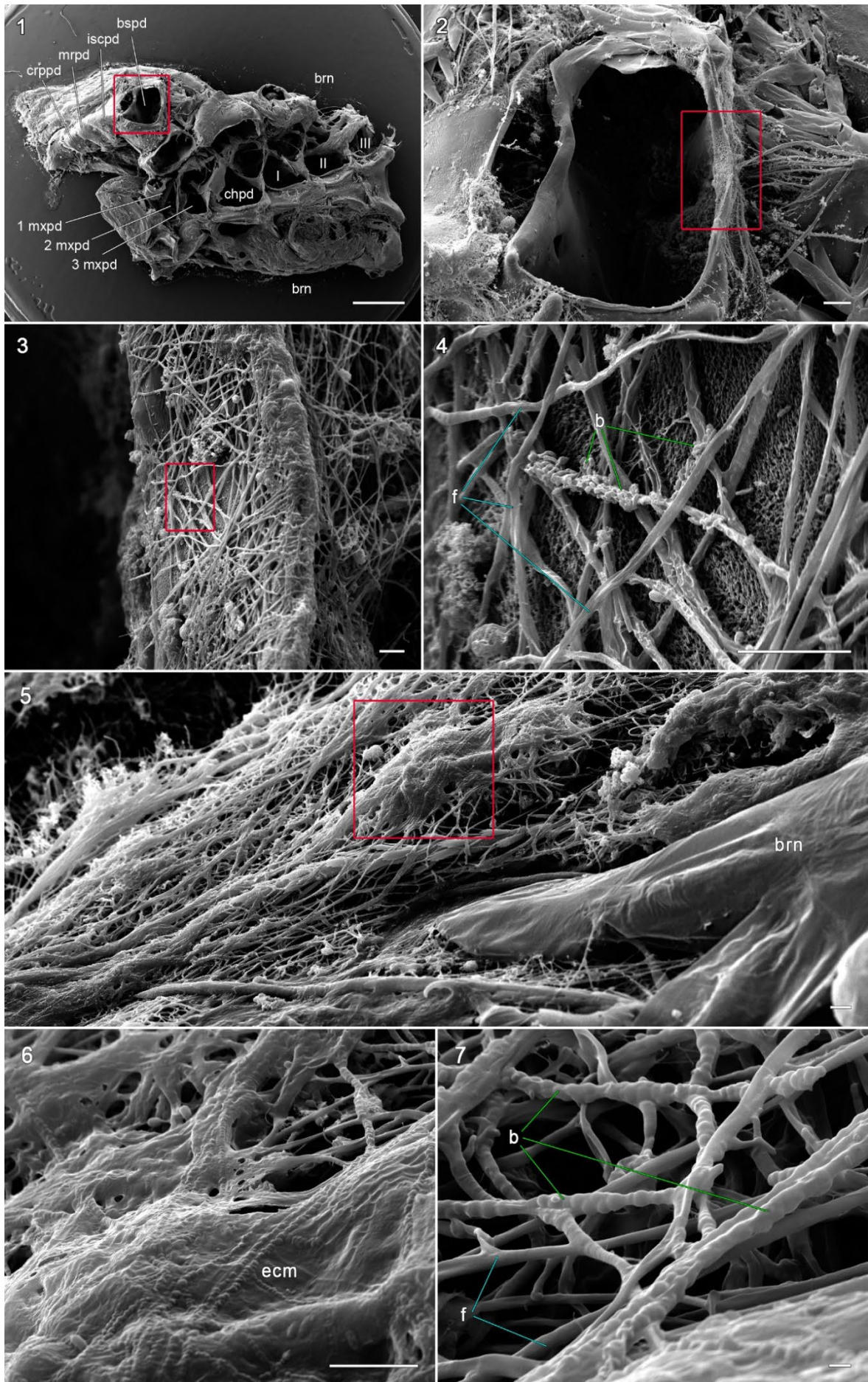
FIGURE 8. SEM-images of the thoracic skeleton of a crayfish with fungal infestation. **8.1** Remains of the thoracic skeleton. *Scale bar* 1 mm. **8.2** Enlargement of the red box from 8.1 showing the right basipod. *Scale bar* 100 μm. **8.3** Enlargement of the red box from 8.2 showing the fungal infestation of the cuticle. *Scale bar* 10 μm. **8.4** Enlargement of the red box of 8.3 showing the fungal infestation with some kind of bacteria. *Scale bar* 10 μm. **8.5** Fungal biofilm around the branchiae. *Scale bar* 10 μm. **8.6** Enlargement of the red box from 8.5 showing the increase of the extracellular matrix. *Scale bar* 10 μm. **8.7** Enlargement of the fungal branches in combination of bacteria. *Scale bar* 1 μm. **b** bacteria; **brn** branchia; **bspd** basipodite; **chpd** cheliped; **crppd** carpopodite; **ecm** extra cellular matrix; **f** fungi; **iscpd** ischiopodite; **mrpd** meropodite; **mxpd** maxilliped; **I-III** pereiopods.
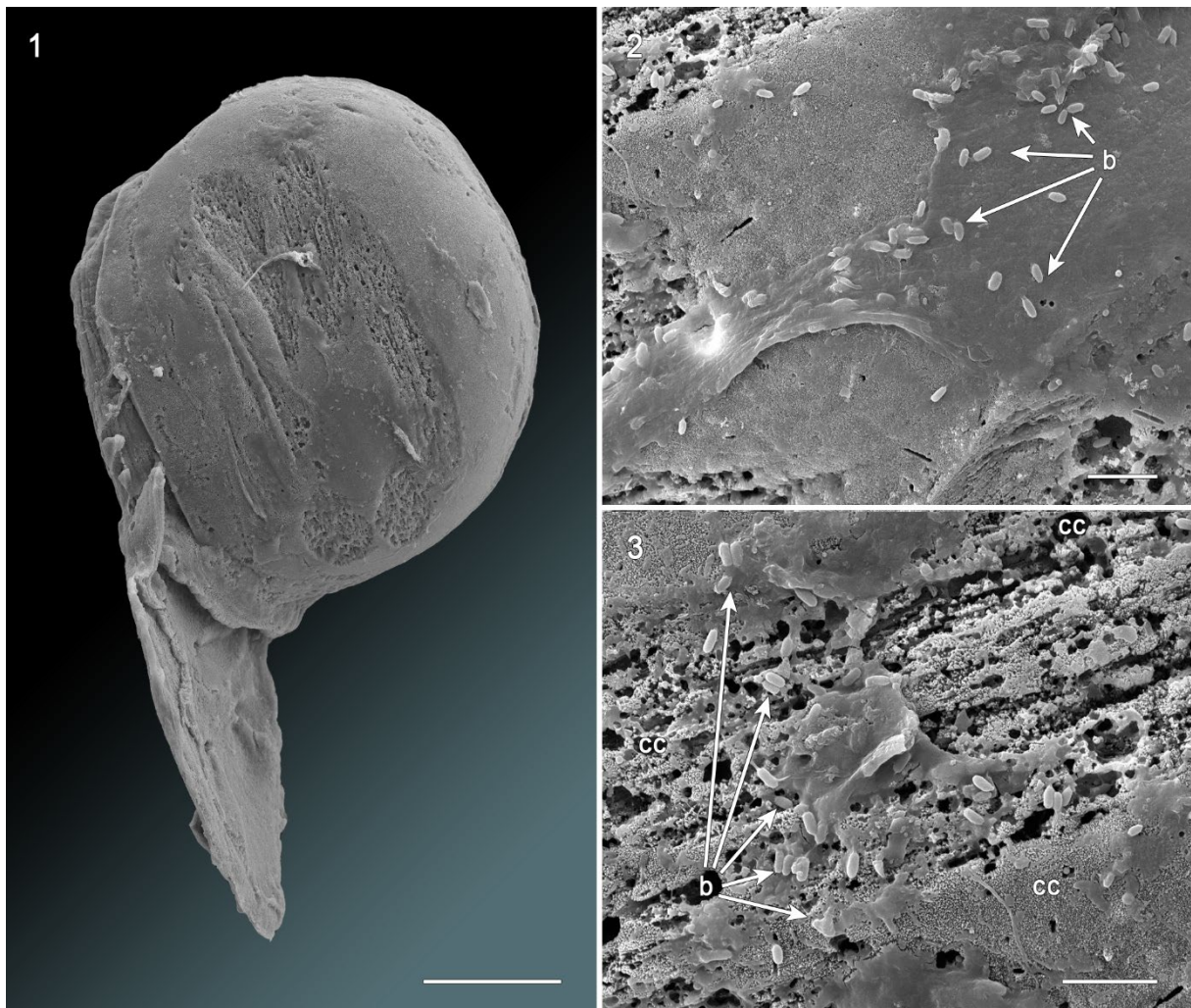
FIGURE 9. SEM-images of a spherical calcite cluster. **9.1** Calcite cluster of C4. *Scale bar* 100 μm **9.2** SEM-image of an enhanced part of the cluster with parts of a biofilm and bacteria. *Scale bar* 10 μm. **9.3** SEM-image of an enhanced part of the cluster with parts of a biofilm and bacteria. *Scale bar* 10 μm. **b** bacteria; **cc** calcite cluster.
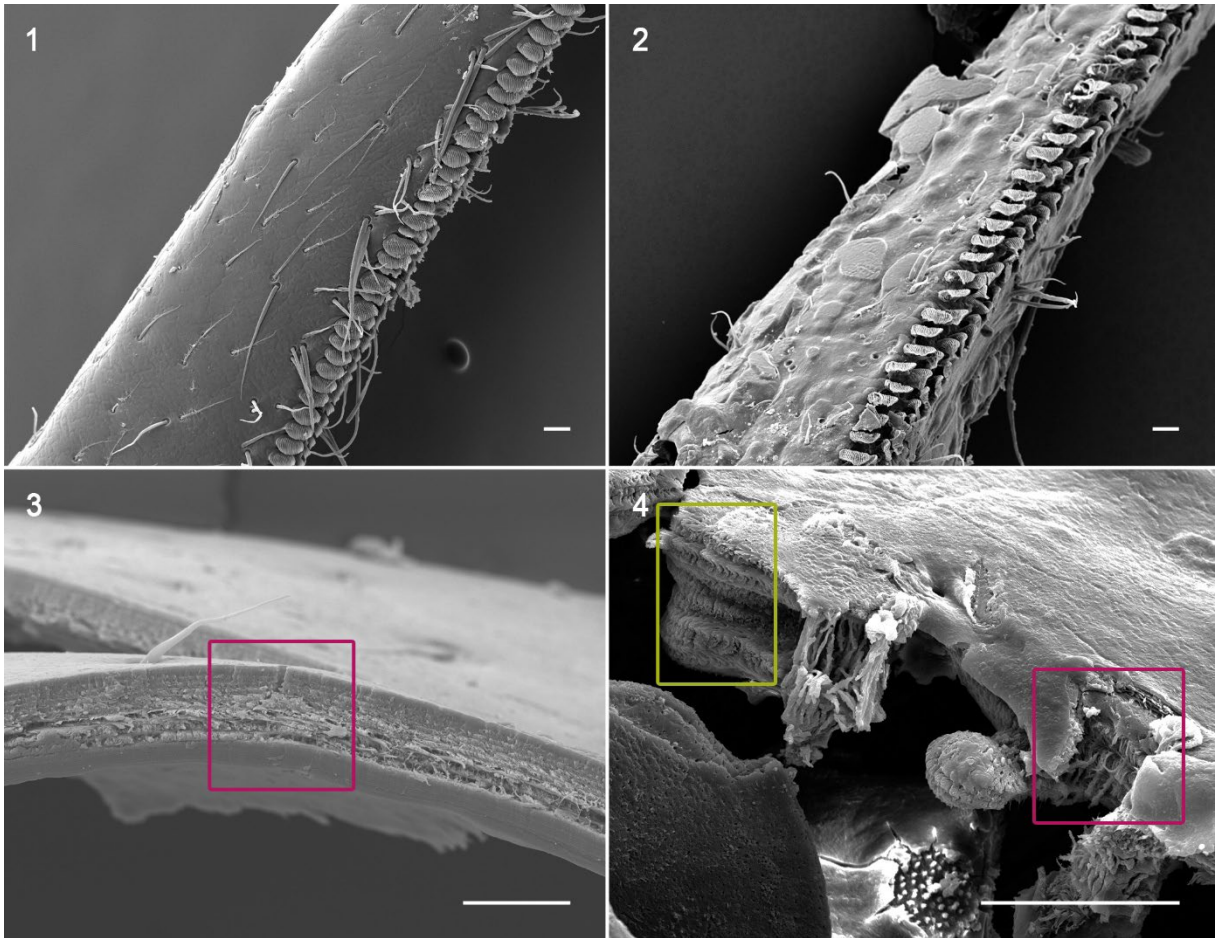
FIGURE 10. SEM-images of fresh and decomposed crayfish structures. **10.1** Middle section of a fresh crayfish dactylus. **10.2** Middle section of the decomposed crayfish dactylus of sample C4 after nine days covered by a biofilm in tank water. **10.3** Cross section of a fresh crayfish cuticle. **10.4** Cross section of the cuticle of the dactylus of sample C4 showing a recrystallized part of the cuticle by calcite clusters (green box) and "unaltered" cuticle structures (pink box). All *scale bars* 50 μm.

High Performance Liquid Chromatography Coupled to Ultraviolet and Mass Spectrometric Detection (HPLC-UV/MS)

Identification of free fatty acids

HPLC-MS analysis of the untreated hepatopancreas extract of sample C4 detected six of the free fatty acids typically found in adipocere, namely palmitic acid, stearic acid, oleic acid, myristic acid, linoleic acid, and palmitoleic acid. Peaks corresponding to each of the six fatty acids were visible in the extracted ion chromatograms (EIC) at the respective mass-to-charge ratio (**Figure 11.1**). To confirm their identity, a standard method, also known as spiking, was used in case of oleic acid, palmitic acid and stearic acid. Here, a defined amount of the fatty acid standard was added to the sample. An increase in the peak area was observed in the extracted ion chromatograms corresponding to the spiked fatty acids (**Supplementary Table S1**). Furthermore, there were no new peaks detected in the extracted ion chromatograms after spiking, confirming that the increase in peak area was due to the added free fatty acid standard. Moreover, free fatty acids originally present in the sample could be readily detected in the negative ion mode of the mass spectrometer as deprotonated ions with a mass-to-charge ratio of $[M–H]^-$, where M is the monoisotopic mass of the acid (for details, see **Supplementary Figure S1** and **Supplementary Figure S2**). Observation of the full scan electrospray ion (ESI)-mass spectra of the peaks (**Figure 11.1**) further confirmed the presence of palmitic acid, stearic acid and oleic acid in the sample. Although standard compounds for further fatty acids were not studied, myristic acid, palmitoleic acid and linoleic acid could be identified based on their mass (**Figure 11.1-2**).

Analysis of triglycerides

Since myristic acid was present in the sample, glycerol trimyristate (M = 721.6) was studied as a standard compound potentially present in the living crayfish. Mass spectra of triglycerides, determined under the applied conditions, show the ammonium adduct of the intact triglyceride in highest abundance, corresponding to M+18 in the positive ion mode, where M is the monoisotopic mass of the triglyceride. Glyceryl trimyristate was not detected in the hepatopancreas sample, as shown in **Figure 12.1-4**. We only observed an unknown mass of 900.8 ± 0.3 m/z (**Figure 12.3-4**). The inability to detect glyceryl trimyristate or closely related triglycerides in the sample indicates that these must have been degraded. The lack of triglycerides, and the detection of free fatty acids expected to be present in adipocere confirms that the analyzed hepatopancreas sample is indeed adipocere.
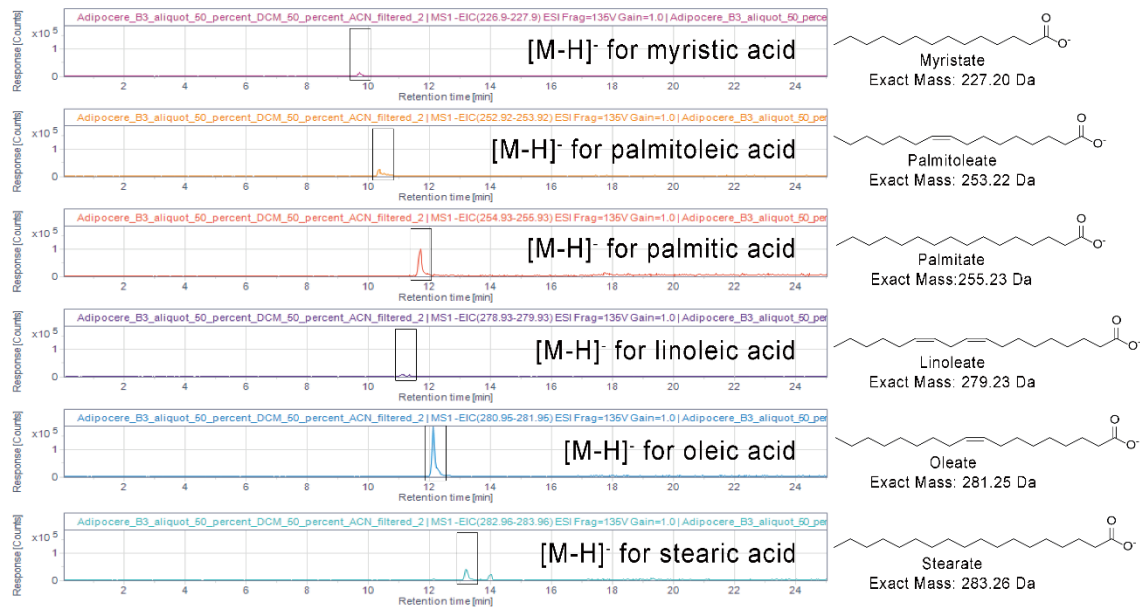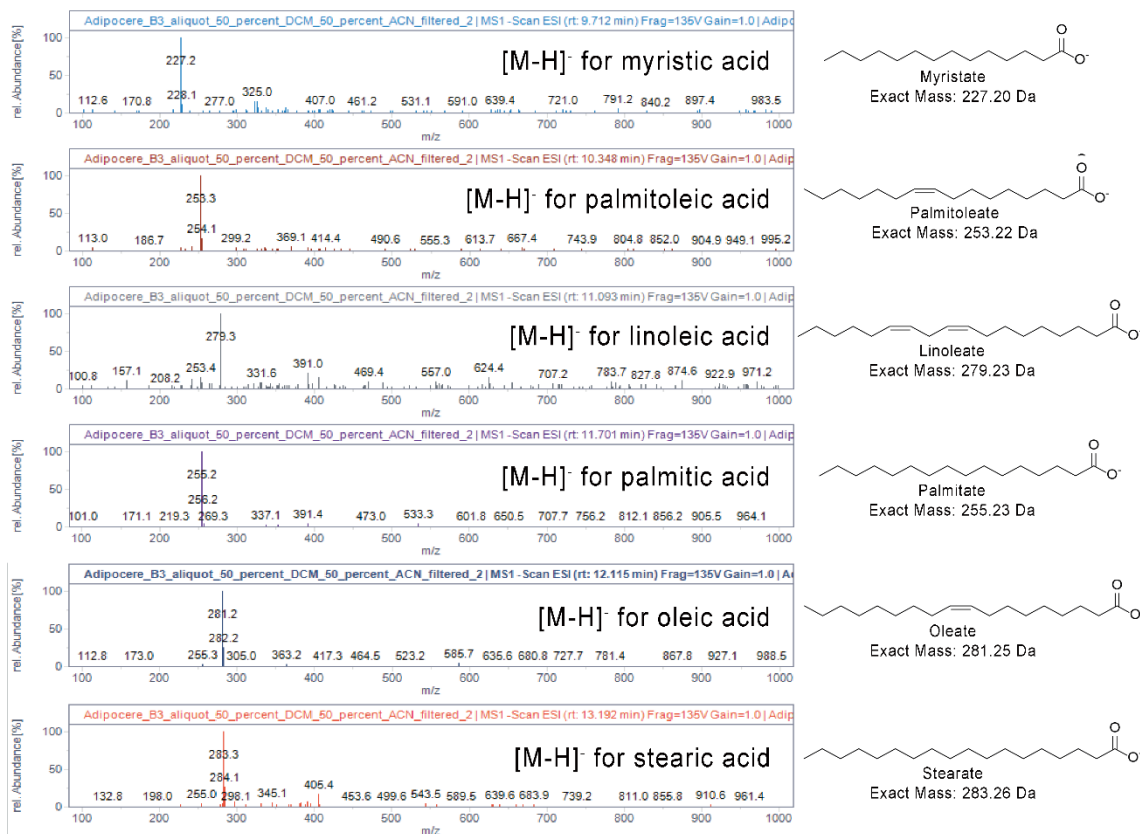
FIGURE 11. 11.1 Extracted ion chromatograms (EIC) showing the deprotonated ion of myristic acid (myristate, 227.2 ±0.7 m/z), palmitoleic acid (palmitoleate, 253.2 ±0.7 m/z), palmitic acid (palmitate, 255.2 ±0.7 m/z), linoleic acid (linoleate, 279.2 ±0.7 m/z), oleic acid (oleate, 281.3 ±0.7 m/z) and stearic acid (stearate, 283.3 ±0.7 m/z) in the adipocere extract, proving the presence of all of these free fatty acids in the adipocere extract. The peak areas observed in the chromatograms are shown indicating the relative amounts of acids present in the sample. **11.2** Electrospray negative ion mass spectra (ESI-MS) showing the deprotonated ions of myristic acid (myristate, 227.2

± 0.3 m/z), palmitoleic acid (palmitoleate, 253.2 ± 0.3 m/z), palmitic acid (palmitate, 255.2 ± 0.3 m/z), linoleic acid (linoleate, 279.2 ± 0.3 m/z), oleic acid (oleate, 281.3 ± 0.3 m/z) and stearic acid (stearate, 283.3 ± 0.3 m/z) in the adipocere extract, proving the presence of these free fatty acids in the extract. The mass-to-charge ratios (m/z) are shown in relative abundance.
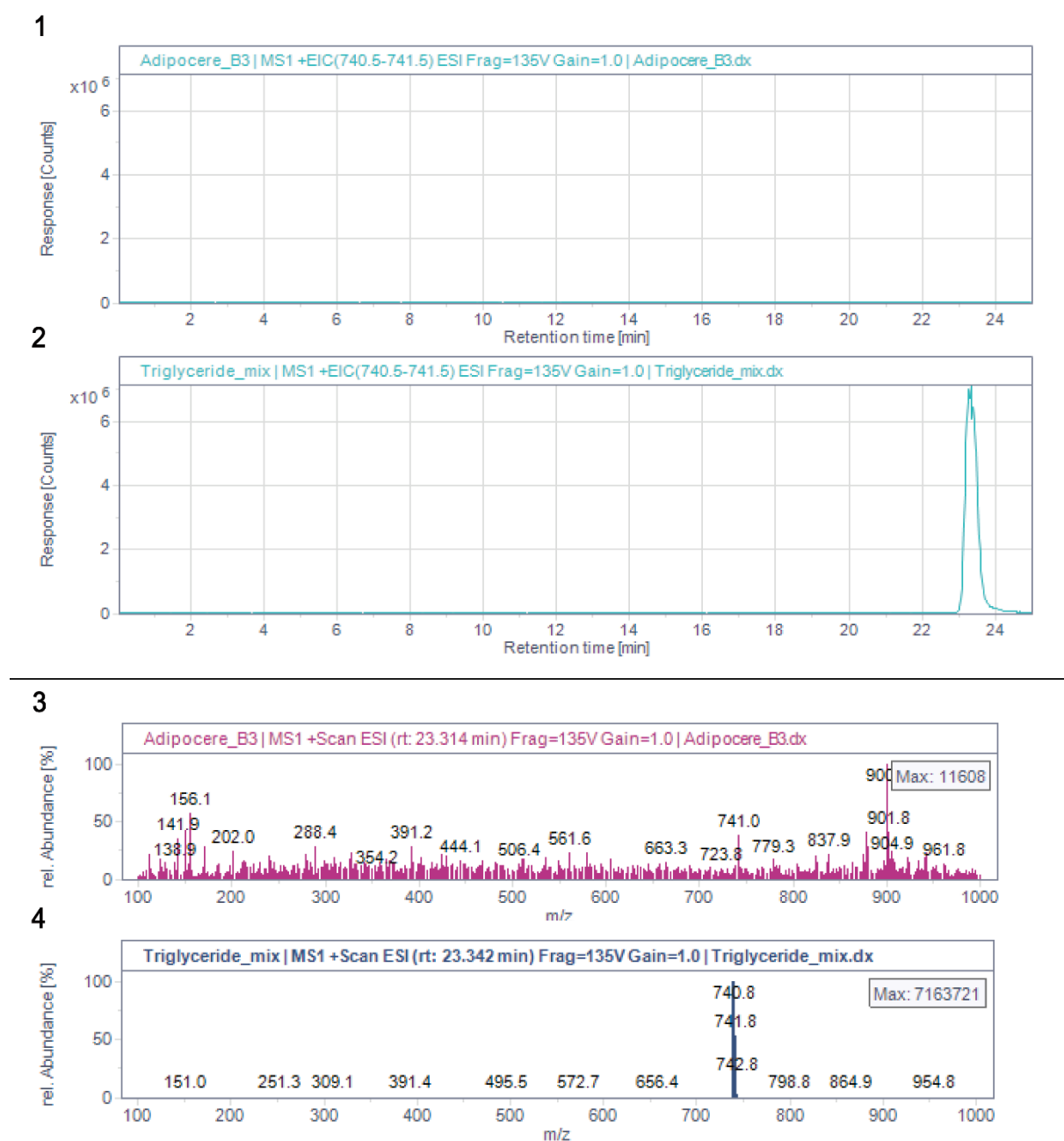
FIGURE 12. 12.1-2 Extracted ion chromatograms (EIC) showing the ammonium adducts (M+18) of the glyceryl trimyristate (722.6 +18 = 740.6 ± 0.7 m/z), in the adipocere extract **12.1** and in the standard solution containing glyceryl trimyristate **12.2**. **12.3-4** Electrospray positive ion mass spectra (ESI-MS) showing the ammonium adduct of glyceryl trimyristate (740.6 ± 0.3 m/z) indicated that the triglyceride was not present in the adipocere extract **12.3**, but only in the standard solution **12.4**. The mass-to-charge ratios (m/z) are shown in relative abundance.

4.4 DISCUSSION

The results of the study show, the fragility of the conditions that lead to a preservation of soft tissues or their complete decomposition. Experiment 1 and 3 were conducted under the same abiotic water conditions (temperature [28°C]; pH [8]; oxygen saturation [8 mg/L]) and the same aquatic sediment (Dehner GmbH & CoKG, 86641 Rain, Germany), and water type. However, the course of decomposition of crayfish individuals of the same species, which had been raised in the same tank community, was completely different. While in tank 1 of experiment 1 biofilm formation and envelopment of the whole carcass occurred and gas accumulation in the branchial area could be detected, none of these occurrences could be observed in any other crayfish, which decomposed in tank 2 during experiment 3. In addition, the tissue transformation of the hepatopancreases into adipocere occurred only in individuals which were covered by a biofilm. It is assumed that the microbial composition inside the tanks was different and therefore extrinsic bacteria were responsible for the significant differences in decay. It is assumed further, that inside the biofilm oxygen was metabolized by microbial activity, resulting in anaerobic conditions which favored the adipocere formation, since fatty acids are stabilized by these conditions (Mant, 1987). Other requirements, e.g., high temperatures (28°C) and a wet environment (tank water) were also fulfilled (Prokop & Göhler, 1975; Penning, 2006). Furthermore, the genus *Clostridium* was detected inside the biofilm, which is commonly associated with the formation of adipocere (O´Brian & Kuehner, 2007), since these bacteria are strong hydrolysers of triglycerides. It is assumed, that the initial formation of adipocere is mainly driven by Gram-positive bacteria, whereas it is important that in the final stages Gram-negative bacteria dominate due to adipocere degradation (Pfeifer et al., 1998; Ueland et al., 2014). The bacterial composition in and on the biofilm of individuals of experiment 1, was dominated by Gram-negative organisms and some of these might be involved in biofilm formation, e.g., *Sphaerotilus*. This genus contains species which settle on surfaces and form filaments that are covered by a sheath and slime (Veen van et al., 1978). SEM-images of crayfish remains from experiment 1, that was enveloped by a biofilm show the presence of fungi that formed branched mycelia (**Figure 8**) and 16S rRNA analyses of the biofilm show that the fungi genus *Pluteus* was the most abundant genus. Therefore, it is assumed that *Pluteus* might play an important role in the biofilm environment in experiment 1.

The genus *Pluteus* is mostly known from wood remains and food, but was also first identified by Niu et al. (2017) as the most abundant genus in activated sludge of eastern waste water treatment plants in China. But its metabolic activity is still unknown. In 2019, Booth et al. (2019) investigated the role of fungi in heterogenous sediment microbial networks in Mangrove

sediments and found out that fungi play the major role in all microbial network interactions. They further showed, that the genus *Pluteus* (as a saprophyte (= heterotrophic organism that live in decomposing organic substances)) formed significant keystone nodes in the subsurface sediments and was one of the most important fungi genera in the microbial network (Booth et al., 2019). Booth et al. (2019) assumed that the fungi acting synergistically with other environmental variables and determine the overall microbial community structure. If the genus *Pluteus* was important for the biofilm formation and/or the adipocere occurrence will be investigated in further studies.

Adipocere is the result of the incomplete hydrolysis of fat in animal tissue by bacteria under mainly anaerobic conditions, because the degradation of fatty acids is restricted to respiratory processes (Schoenen & Schoenen, 2013). Under anaerobic conditions fatty acids cannot undergo β-oxidation and are degraded only very slowly.

Caused by the ability of adipocere to slow down or inhibit decay processes (Forbes et al., 2005) it has been suggested as a key component in the outstanding preservation of fossils in Konservat-Lagerstätten like Messel, Holzmaden (Schwermann et al., 2012), or Solnhofen (Reisdorf & Wuttke, 2012). It is also assumed, that adipocere preceded the phosphatization of insects discovered from Quercy (France), as a shaping component (Flach, 1980).

In 2020, the crustacean-like specimens of the arthropod *Dollocaris ingens*, found in the Jurassic Konservat-Lagerstätte of La Voulte-sur-Rhône (France), were reinvestigated to clarify their preservation pathway (Jauvion et al., 2020). These fossils show an exceptional morphological preservation of inner structures (e.g., muscles and hepatopancreas), which were preserved by fluorapatite and pyrite. Here, the transformation of the inner structures must have happened rapidly post mortem, when the sediment was still moist, loose and not complete anaerobic (Jauvion et al., 2020). Jauvion et al. (2020), as well as Wilby et al. (1996) state, that the fossilization process occurred simultaneously with the biodegradation and was influenced by the tissue type and local microenvironments. This assumption is supported by the results of Grimes et al. (2001), which show that the pyritization of plant cells depends on the plant type and the specific conditions.

In view of the fact, that the structure of the hepatopancreas of *Dollocaris ingens* was very similar to that of modern crustaceans (Esteve & Herrera, 2000), and the fast transformation of the hepatopancreas into adipocere (only in 9 days) in experiment 1 of this study, it is assumed that the hepatopancreases of *Dollocaris ingens* might also first have been stabilized by adipocere before they were preserved in pyrite. This assumption is also supported by the study of Grimes et al. (2001), in which the pyritization did not directly replace the original tissue.

Here, fossilization was a result of precipitation of crystals on and between cells resulting in filling out of extracellular spaces. Grimes et al. (2001) hypothesized that, as microbial decay continued, more space would become available for pyrite crystals resulting in a cast of the original material. For *Dollocaris ingens* it is conceivable that during the decay under partly aerobic conditions triglycerides were hydrolytically split into glycerol and fatty acids and the sulfur-containing amino acids (cysteine and methionine) were degraded, whereby sulfur of the sulfide group was oxidized to sulfate or released as hydrogen sulfide deeper in the tissue (Schoenen, 2019). In the anaerobic environment the fatty acids were degraded very slowly resulting in the formation of adipocere. However, over the years, bacterial syntrophic communities or bacterial species that are able to perform both reactions, use sulfate as alternative electron acceptors and degrade fatty acids (*Desulfobacteriaceae*, *Desulfarculaceae*, *Desulfohalobiaceae*, *Syntrophobacteraceae*, and *Peptococcaceae*) (Rabus et al., 2006; Sousa et al., 2009; Sousa et al., 2010), degraded adipocere and released hydrogen sulfide. From the field of forensic science, it is known that hydrogen sulfide is able to react abiotically with iron from the hemoglobin to form iron sulfide (Fiedler et al., 2015), which might later react to pyrite (Berner, 1976). In *Dollocaris ingens* hydrogen sulfide might have reacted with the iron from the hemolymph and/or the surrounding medium. It must be investigated, whether the increase of the iron content inside the hemolymph of decapods during the moulting process (Recio & Léon, 1976) might have a positive effect on the formation of iron sulfide and later the formation of pyrite.

The adipocere theory might also be interesting for the preservation of neural tissues in the arthropods of *Fuxianhuia* from the early Cambrian Chengjiang Lagerstätte in southwest China. It is assumed that the organic macromolecules of the central nerve system, where the tissue is enriched in lipids (Ma et al., 2015), were first stabilized by adipocere. Adipocere can be formed out of muscle tissue, fat and sphingosine (Schoenen, 2019). Sphingosine is a carbon rich amino acid (C-18) which forms the primary part of sphingolipids in the membrane of myelin sheaths that surround nerve cell axons (Kolter & Sandhoff, 1999).

The results of the study presented here, further show that a biofilm might influence the type of calcite precipitation. Calcite clusters appeared coarse-grained with a size of 260 to 470 μm in the absence of biofilms (Mähler et al., 2020), and appeared fine grained (100 to 200 μm) if a biofilm was present (**Figure 6**). In addition, the results show that a strong biofilm is able to prevent a carcass from floating if a gas accumulation occurred, but will not protect it against small scavengers, like ostracods.

4.5 CONCLUSIONS

It seems that the preservation of *Cambarellus diminutus* soft tissue or its complete decomposition was mainly influenced by the extrinsic microbial community of the tank water in the experiments. The hepatopancreas of the crayfish individuals were completely transformed into adipocere only in the presence of a biofilm. The biofilm was mainly composed of the bacterial genus *Sphaerotilus* and the fungi genus *Pluteus*. It is assumed that the combination of these microbial genera might play an important role in soft tissue preservation. The analyses of the altered hepatopancreas sample revealed that it contains a mixture of saturated (palmitic, stearic, and myristic acids) and unsaturated fatty acids (oleic, linoleic, and palmitoleic acids). The inability to detect glyceryl trimyristate or similar triglycerides in the sample indicates that most triglycerides have been degraded, which is typical for adipocere. It is assumed that, because of the early diagenetic transformation of soft tissue into adipocere (9 days) and the shape-retaining ability of this substance, adipocere might be a first step in soft tissue preservation under certain conditions.

Chapter 5

The decomposition of *Cambarellus diminutus* in lake water and lake sediment under different environmental conditions

5.1 Introduction

"Konservat-Lagertätten" like the middle Eocene Messel- or the Upper Oligocene Enspel Formation harbor a distinct soft tissue fossil record. The different steps which lead to such a fossilization of soft tissues remain unclear and especially the role of bacterial activity is not yet fully understood. Immediately after death autolytic enzymes (e.g., lipases, proteases) start a self-digestion of the dead cells and nutrient rich liquids are released (Penning, 2006; Vass, 2001). Released tissue fluids serve microorganisms as a source of nutrition and they continue to decompose the organic matter. Microorganisms, such as bacteria, spread over the entire body, starting from the most densely populated body regions, as the gastric, intestine or respiratory systems and the body surface. It is assumed that rapid heterotrophic decay and autolysis of soft tissue release high amounts of ions from the organic material and the surrounding medium, which lead to a stabilization of soft tissue remains and authigenic mineralization (Jauvion et al., 2020; Wilson & Butterfield, 2014).

Phosphatization, pyritization, silification as well as the preservation by carbonate minerals e.g., calcite and aragonite are some of the main processes for outstanding preservation (Muscente et al., 2017 and references therein), and can sometimes be identified together in one fossil (Jauvion et al., 2020). Therefore, the mineralization- and decay process might occur simultaneously and are specific to the tissue type (Jauvion et al., 2020; Wilby & Whyte, 1995; Wilby et al., 1996). Different tissues may offer different potential for microbial colonization during decay and local environmental conditions influence the mineralization process (Raff et al., 2013). In addition, in living animals different body parts (e.g., intestine, gills) are colonized by different microbial communities (Zhang et al., 2016), which might differ in their mineralization potential.

Preservation of soft tissues is often associated with anaerobic conditions that reduce autolytic activity and influence microbial degradation (Briggs & Kear, 1993a; 1994; Butler et al., 2015; Eagon et al., 2017). This did not consider that several bacteria exhibit various adaptions to reduced oxygen conditions. For example, the bacterium *Pseudomonas tunicata* formed pseudomorphs of marine embryos under aerobic conditions, but destroyed the internal structure of the cells when oxygen was not available or depleted (Raff et al., 2013).

While some studies revealed faster decomposition of soft tissue under aerobic conditions (Briggs & Kear, 1993a; Martin et al., 2003; Gostling et al., 2009), other experimental results show no differences in comparison to anaerobic decay (Allison, 1988) or only rare differences under various oxygen conditions (Briggs & Kear, 1994). Especially, one study highlighted that some cnidarian tissues decayed even faster under anaerobic conditions (Hancy & Antcliffe, 2020).

There is no knowledge about the individual bacteria that impact the important decay and preservation processes and if they derive from the carcass itself (gastro intestinal / integumental flora) or from the extrinsic surrounding (environment). First results indicated a stabilizing influence of endogenous microorganisms presumably from the gastro intestinal tract of bilaterian organisms (Butler et al., 2015), whereas Eagan et al. (2017) highlighted that each organism exhibits an individual microbiome that can either support preservation or fasten decay. Therefore, taphonomic experiments focusing on microbial activity and associated organic changes under different environmental conditions are necessary to identify the phases of decay that must either be suppressed or must proceed first to ensure conditions responsible for soft tissue maintenance. The following study was divided into two parts in order to obtain as much information as possible. The part presented here deals with the description of outer and inner changes of the crayfish carcasses with progressive decay, pH-values and oxygen conditions. A detailed description of the microbiological part of the following study can be found in the dissertation of Janssen (2021) entitled "Der Einfluss bakterieller Aktivität auf die Präservierung und den Abbau von Weichgewebe".

5.2 Material and methods

96 individuals with partly filled guts, were sacrificed by placing them in an atmosphere of carbon dioxide (CO_2). Specimens were not dried before weighing on a micro scale. Lengths were measured from the anterior tip of the cephalothorax to the end of the abdomen without the telson (**Supplementary Table S1**).

In the study 8 different experimental setups were conducted. Four experiments were conducted under a constant temperature of 24°C and four experiments under 4°C. 128 sterile Falcon tubes (50 mL), were filled with ~ 6 g of near shore sediment, taken from a freshwater lake called "Alte Tongrube" in Bonn-Röttgen, Germany (50°40'24.7"N / 7°04'29.6"E). Each experiment was conducted on a different time of the year. Therefore, experimental setup conditions might differentiate in the composition of microbial communities in water and sediment, and also in the presence of shell remains of e.g., gastropods, bivalves and ostracods (**Figure 1**).
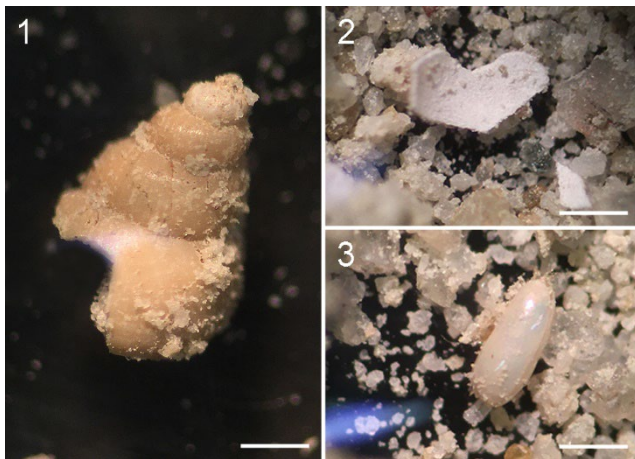
FIGURE 1. Contaminations inside the sediment. **1.1** Shell remain of a gastropod. **1.2** Shell remain of a bivalve. **1.3** A complete ostracod. *Scale bar* 1 mm.

96 dead specimens were each placed on the sediment in one of these Falcon tubes. The tubes were filled with 40 mL of lake water, taken from the same locality. For each experiment, which was conducted under 24°C, 13 dead crayfish individuals were used and 3 blank samples (without crayfish) were steeped. For experiments under 4°C only 12 individuals were used. Each experiment had 6 time slots at which 2 samples were tested on pH-value, oxygen saturation, olfactory and optical changes. Attention was paid on the color of the cuticle, gas accumulation and disarticulations. Oxygen saturation and pH-values were measured with an oxygen probe, OXPB-11 and pH-meter, PCE-PHD 1 (both PCE Deutschland GmbH, Meschede, Germany). Further on, samples were dissected and examined by using a stereomicroscope, Stemi 2000 (Carl Zeiss Microscopy Deutschland GmbH, Oberkochen,

Germany). During the dissection attention was paid to internal changes. The focus was on the following organs: Branchiae, hepatopancreas, gastric, intestine, ganglion and muscle tissue (**Figure 2**). Images of the decomposing crayfish were taken by using a stereomicroscope (Stemi 2000) combined with an iPhone 12 mini holding by Gosky Universal Digiscoping Smartphone Adapter, FBA_QHAPO21 (Gosky-optics, USA). Images have 4032 x 3024 pixel and 24 bit with an exposure time of 1/50 sec. The images of the calcite structures shown in Figure 17.1 and 17.3 were photographed with a stereo-zoom-microscope (Axio Zoom V16, Carl Zeiss Microscopy Deutschland, Oberkochen, Germany). Final figures were created by using Adobe Photoshop CS5 (Adobe, Dublin, Republic of Ireland) with 300 dpi. In experiments which were conducted in an incubator (Memmert GmbH & Co. KG, Schwabach, Germany) under a constant temperature of 24°C (Exp. 1 and 2 as well as Exp. 5 and 6), samples were investigated on day 2, 3, 4 and day 7, 14 and 21. Blank samples were investigated on day 1 and 21. In experiments which were conducted in a cooling chamber (Viessmann Kältetechnik AG, Saale, Germany) at a constant temperature of 4°C (Exp. 3 and 4 as well as Exp. 7 and 8), samples were investigated on day 7, 14, 21, 49, 77 and 105. Blank samples were investigated on day 1 and 105.
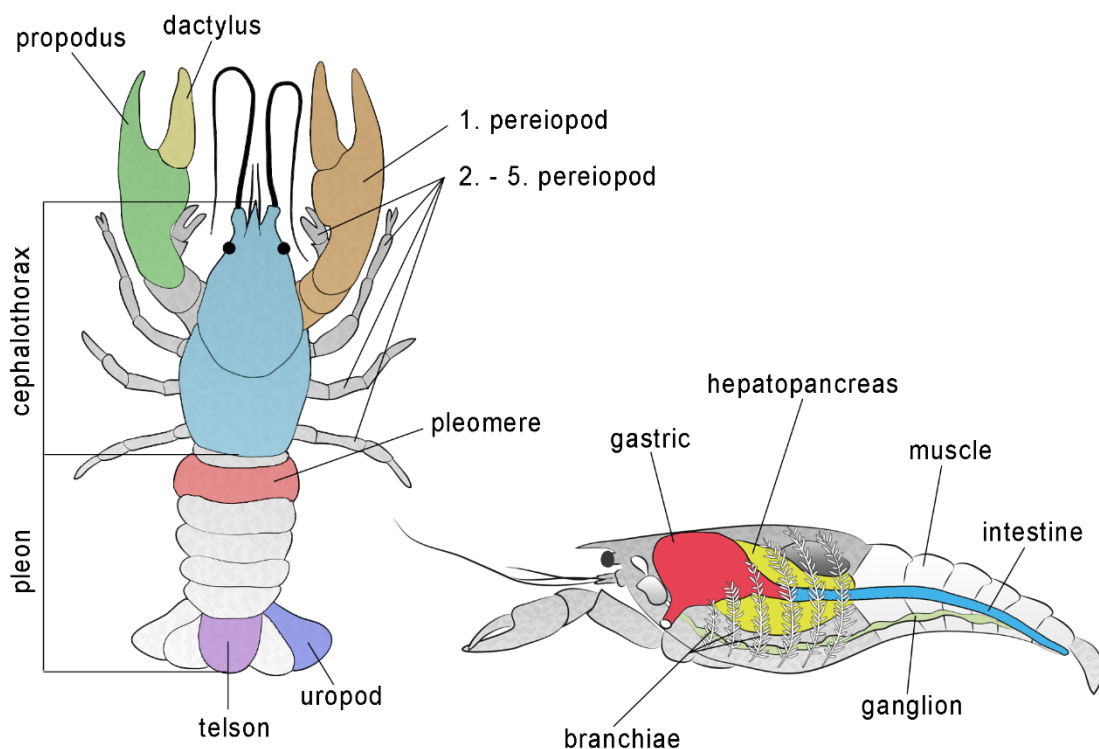
FIGURE 2. Anatomical characteristics of crayfish. **2.1** Dorsal view of a crayfish sketch showing general morphological features. **2.2** Lateral view of a crayfish sketch showing general inner anatomical features.

In addition, experiment 1 and 3 (Exp. 1 and Exp. 3) were conducted with untreated sediment and water under aerobic conditions. Experiment 2 and 4 (Exp. 2 and Exp. 4), were conducted with sterile sediment and water under aerobic conditions. Experiment 5 and 7 (Exp. 5 and Exp. 7), were conducted with untreated sediment and water under partly anaerobic conditions. Experiment 6 and 8 (Exp. 6 and Exp. 8), were conducted with sterile sediment and water under partly anaerobic conditions. For sterile experiments the water and sediment were autoclaved for at least 20 min at 121°C. All experiments were set up under a laminar flow hood. Experiments under anaerobic conditions were prepared with the addition of 10 mM β-mercaptoethanol (Sigma-Aldrich Chemie GmbH, Germany) as a reducing agent. Further on, partly anaerobic conditions were established with gas generating systems BD Difco^{TM} GasPak^{TM} EZ Anaerobier Pouch System (BD Becton, Dickinson and Company, USA). Experimental setup is also shown in **Figure 3**.

At the beginning of each experiment carcasses were fully articulated and blue in color. In addition, no symbiotic, parasitic or commensally organisms were found on the carcasses.
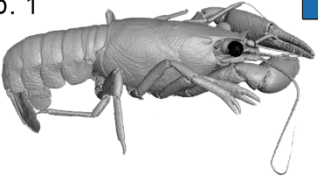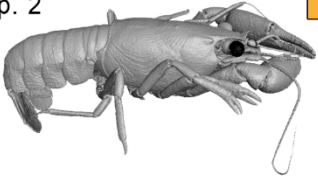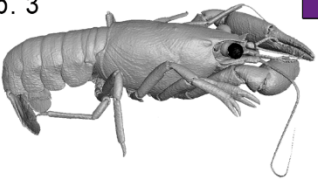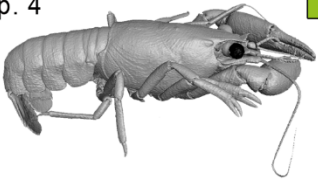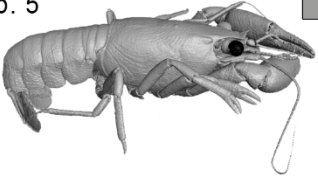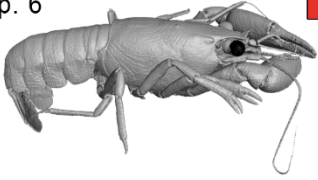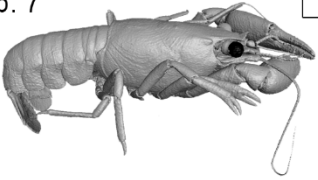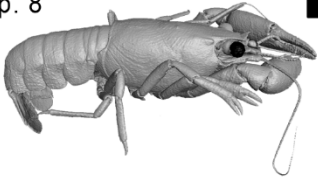
FIGURE 3. Experimental setup design. **Exp. 1** was conducted under aerobic conditions with untreated water and sediment at 24°C. **Exp. 2** was conducted under aerobic conditions with sterile water and sediment at 24°C. **Exp. 3** was conducted under aerobic conditions with untreated water and sediment at 4°C. **Exp. 4** was conducted under aerobic conditions with sterile water and sediment at 4°C. **Exp. 5** was conducted under partly anaerobic conditions with untreated water and sediment at 24°C. **Exp. 6** was conducted under partly anaerobic conditions with sterile water and sediment at 24°C. **Exp. 7** was conducted under partly anaerobic conditions with untreated water and sediment at 4°C. **Exp. 8** was conducted under partly anaerobic conditions with sterile water and sediment at 4°C.

Micro-Computed Tomography (μ-CT)

During the first four days, three samples of Exp. 1, 2, 5 and 6 (E1-21.1 - 21.3; E2-21.1 - 21.3; E5-21.1 – 21.3 and E6-21.1 – 21.3) were initially scanned once per day, followed by scans after 7, 14 and 21 days using a phoenix|x-ray v|tomex s 240 micro-computed tomography (μ-CT) scanner (GE Measurement & Control, Wuntsdorf, Germany) located at the Institute of Geosciences of the University of Bonn. Two samples of Exp. 3, 4, 7 and 8 (E3-105.1 – 105.2; E4-105.1 – 105.2; E7-105.1 – 105.2 and E8-105.1 – 105.2) were scanned on day 1, followed by scans after 7, 14, 21, 49, 77 and 105 days. Each data set has a resolution of 38 μm; the scans were carried out at 80 kV and 100 μA. Three frames per projection were acquired by a timing of 500 ms for a total of 1000 projections. The CT data were processed using the software VG Studio Max 3.2 (Volume Graphics, Heidelberg, Germany) and Avizo 8.0 (Thermo Fisher Scientific, Schwerte, Germany) to reconstruct and visualize precipitated crystal clusters inside the specimens, and gastroliths located inside the gastric. In addition, Avizo 8.0 was used for volume measurements of polygonal 3D-surface models.

Inductively Coupled Plasma Mass Spectrometry (ICPMS)

On each time slot of the experiments two samples were analyzed. Therefore, 4 mL of each test tube were taken and filled in a 5 mL tube, which had been previously cleaned twice by deionized water [MilliQ] (18.2 MΩ*cm at 25°C) and dried for two days. Afterwards, water samples in 5 mL tubes were acidified by 0.2 mL of concentrated nitric acid (HNO_3 [65 %]) and stored at 4°C. The calcium (Ca) content of the sample solutions was determined with an Element 2/XR Sector Field ICP-MS instrument (Thermo Fisher Scientific) at medium resolution mode in order to avoid contributions from interfering species on the monitored Ca masses (^{43}Ca and ^{44}Ca). All solutions (including sample solutions, blank solutions, calibration solutions and reference materials) were measured twice and concentration data were derived from both signals which were finally also compared for consistency. However, only concentrations based on ^{43}Ca signal intensities were eventually used because of generally higher precision. Prior to analysis all solutions were further diluted and adjusted to ~2 vol. % HNO_3. To correct for instrumental drift, rhodium (Rh) was added as an internal standard (all solutions were adjusted to a final Rh content of 1 μg/L). In addition to the internal standard, drift monitors were measured repeatedly throughout the analytical sequence to allow, if necessary, for additional drift that could not be compensated by the internal standard. To evaluate the Ca content of the sample solutions, a 5-point linear calibration (covering the concentration range between 1 and 10 mg/L) was used with calibration solutions that were diluted from a Merck Certipur VI certified multi element

solution. The calibration was validated with SPS-SW2 (a certified reference material for element analysis in surface water). For this purpose, 2 different dilutions of SPS-SW2 that lie within the calibrated concentration range (a 2- fold and 4-fold diluted solution with Ca contents of 2.5 mg/L and 5.0 mg/L) were freshly prepared and analyzed.

The calcium content in lake water at the beginning of each experiment could be found in **Supplementary Table S2.1-8**.

Confocal Raman Spectroscopy (CRS)

Crystal clusters (if present) were obtained from the carcasses and analyzed by a LabRam HR800 Raman spectrometer (Horiba Scientific) using a 784 nm laser as excitation source, a grating of 600 grooves/mm, and a 100 x objective with a numerical aperture of 0.9. The confocal hole size and the spectrometer entrance slit size was set to 1000 and 100 μm, respectively. With these settings the spectral resolution was 4.55 cm^{-1}. The total exposure time was 2 min with four accumulations of 30 s.

Scanning Electron Microscope (SEM)

Crystal clusters (if present) were dissected and coated by a thin layer of gold by using a cool sputter coater (Cressington Sputter Coater 108 manual, Tescan GmbH, Dortmund, Germany). Afterwards, samples were subsequently scanned with an 'environmental' scanning electron microscope (SEM) unit (TESCAN VEGA 4 LMU) by using the SE detector at 20 keV. Images have 1536 x 1331 pixel and 16 bit.

5.3 Results

General observations

Exp. 1 (24°C / untreated water and sediment / aerobic)

On day 2 samples exhibited olfactory changes and cuticles of all samples had changed their coloration from blue to red. The cuticles were still solid and no internal changes could be detected. On day 3 only the gastrice were decomposed and muscles appeared pink on day 4. From day 7 forward cuticles were soft, jellylike and translucent, muscles were pulpy and branchiae, hepatopancreases, intestines and ganglia were decomposed. After two weeks the water around the carcasses was gloomy grey to black in color and the sediment, as well as the carcasses were covered by a black layer. In addition, an accumulation of putrefaction gas could be noticed around the branchial area and a flower (biofilm) could be detected at the water surface. On day 24, three days after the regular study-period, the cephalothorax of E1-21.1 was detached from the carcass floating on the surface (**Figure 4.1**). In sample E1-21.3, also on day 24, the cephalothorax was partly detached from the carcass and floated, holding the rest of the dangling body (**Figure 4.2**). Every internal structure was decomposed except some pulpy muscle tissues (**Figure 4.2**). See also **Supplementary Table S3.1** and **S4.1**.
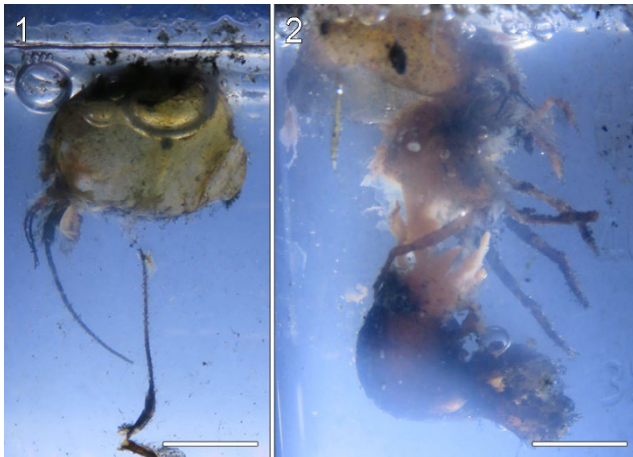
FIGURE 4. Remains of decomposing crayfish on day 24. **4.1** Floating cephalothorax of crayfish sample E1-21.1 with gas bubbles inside. **4.2** Partly detached cephalothorax floating and holding the rest of the dangling carcass of crayfish sample E1-21.3. *Scale bar* 1 cm.

Exp. 2 (24°C / sterile water and sediment /aerobic)

First changes could be mentioned on day 3. The cuticle of the cephalothorax of all samples was still blue in color, whereby the cuticle of the pleon changed its coloration into red. Every internal structure was visible except the decomposed gastric. From this time forward all samples exhibited olfactory changes and the water was gloomy grey. On day 4 muscles had changed their coloration from white to pink and all cuticles were red in color. On day 7 cuticles of the carcasses appeared soft, jellylike and translucent. Hepatopancreases, intestines and ganglia were now decomposed, whereas the branchiae were still visible. In addition, muscles were

pulpy and the pleon of the samples (E2-7.1 and E2-7.2) was completely articulated, but separated from the cephalothorax. After two weeks the sediment, as well as the carcasses were covered by a black layer and all internal structures were decomposed. On day 21 the water was gloomy dark grey and a flower (biofilm) could be detected on the water surface (**Figure 5**). See also **Supplementary Table S3.2** and **S4.2**.
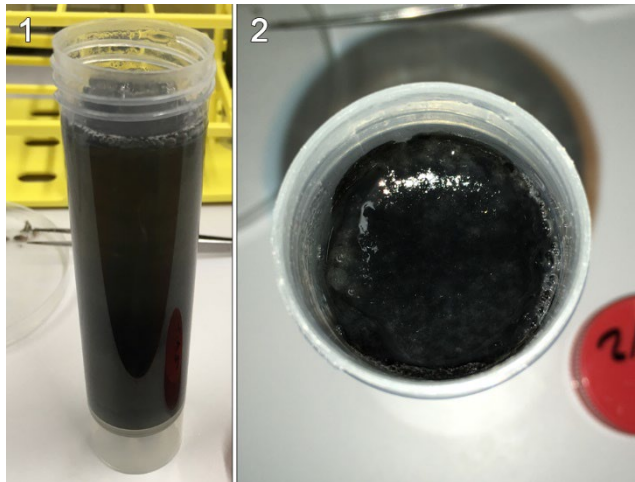
FIGURE 5. Falcon tube of E2-21.2 with water and sediment on day 21. **5.1** Frontal view of the falcon tube with gloomy dark grey water. **5.2** Falcon tube from above with flower (biofilm) on the water surface.

Exp. 3 (4°C / untreated water and sediment /aerobic)

From day 21 to 105 sediments and carcasses were covered by a black layer and olfactory changes were noticed. The first changes of the carcasses could be noticed on day 49. In sample E3-49.2 the gastric and the hepatopancreas were decomposed and muscles were pink in color. A change in cuticle coloration was only mentioned in sample E3-49.2, whereby the cephalothorax was still blue, but the pleon showed a red coloration. No optical changes could be mentioned in sample E3-49.1. On day 77 cuticles were completely red, soft, jellylike and translucent. During the extraction of sample E4-77.1 chelipeds disarticulated and the cephalothorax was slightly detached from the body (**Figure 6**). Gastrice and hepatopancreases were decomposed and muscles were pink in color. Branchiae, intestines and ganglia were still visible. On day 105 intestines and ganglia were still visible, whereby branchiae, hepatopancreases and gastrice were decomposed. See also **Supplementary Table S3.3** and **S4.3**.

FIGURE 6. Carcass of sample E3-77.1 with slightly detached cephalothorax and disarticulated chelipeds. *Scale bar* 1 cm.

Exp. 4 (4°C / sterile water and sediment /aerobic)

The first changes were mentioned after three weeks. In all samples of experiment 4 cuticle coloration of the cephalothorax had changed from blue to red and pleons were still blue in color till the end of the experiment (**Figure 7**). From day 49 forward olfactory changes were noticed in all samples. The hepatopancreas and the gastric were decomposed only in sample E4-49.1. On day 77 the sediment and the carcasses were covered by a white slimy layer and the hepatopancreases as well as the gastrice were decomposed. Muscles had changed their coloration from white to pink on day 105. Cuticles were still solid until day 105. **Supplementary Table S3.4** and **S4.4**.

FIGURE 7. Carcass of sample E4-49.1 with red cephalothorax and blue pleon on day 49. *Scale bar* 1 cm.

Exp. 5 (24°C / untreated water and sediment / anaerobic)

On day 3 muscles of both samples were pink in color. From this day forward, all samples of experiment 5 exhibited olfactory changes. On day 4 the cuticle of the pleon, as well as the muscles had changed their coloration, whereby the cephalothorax of the samples were still blue

in color. Cuticles were solid and only hepatopancreases and gastrice were decomposed (**Figure 8**). The cephalothorax of the samples was soft and jellylike on day 7, whereby the cuticle of the pleon was still blue in color. Muscles were pulpy and branchiae, intestines and ganglia were decomposed. On day 14 all internal structures were decomposed. Sediments and carcasses were covered by a black layer and the pleon of sample E3-14.1 was detached from the cephalothorax during the extraction. See also **Supplementary Table S3.5** and **S4.5**.
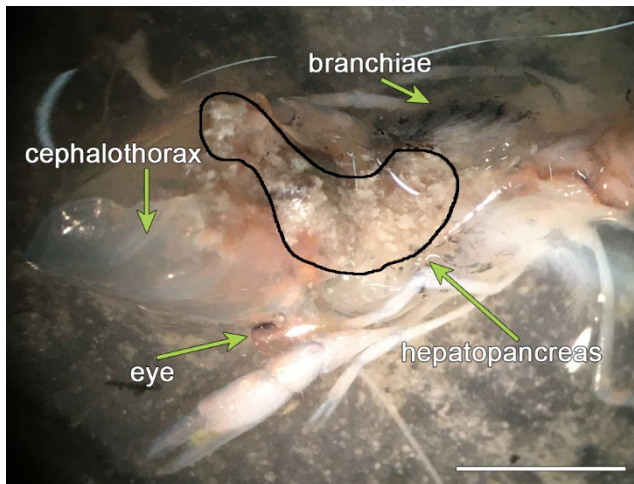
FIGURE 8. Carcass of sample E5-4.1 with decomposed hepatopancreas on day 4. Cephalothorax was detached for dissection *Scale bar* 0.5 cm.

Exp. 6 (24°C / sterile water and sediment / anaerobic)

Form day 3 forward in all samples olfactory changes were noticed and the water around the carcasses was gloomy grey. The muscles of carcass E6-3.1 and E6-3.2 were pink in color and only the pleon changed its cuticle coloration. On day 4 the hepatopancreases and the gastrice were decomposed. From day 7 forward all cuticles had changed their coloration from blue to red, were soft, jellylike and translucent (**Figure 9**). Muscles were pulpy and branchiae, intestines and ganglia were decomposed. On day 21 sediments and samples were covered by a black layer. **Supplementary Table S3.6** and **S4.6**.

FIGURE 9. Carcass of sample E6-7.1 with red carapace on day 7. *Scale bar* 0.5 cm.

Exp. 7 (4°C / untreated water and sediment /anaerobic)

On day 7 cuticles of all carcasses of experiment 7 had changed their coloration from blue to red, and were still solid until day 49. On day 7 the gastric and hepatopancreas of E7-7.1 were decomposed, but in E7-7.2 only the hepatopancreas decayed. Branchiae, intestines and ganglia of both samples were visible. On day 14 gastrice and hepatopancreases of both samples were decomposed and the muscles of sample E7-14.2 were pink in color. On day 21 muscles were pink in color and every internal structure could be identified. From this time foreword all samples smelled and sediments were covered by a black layer. From day 49 forward all cuticles of experiment 7 were soft, jellylike and translucent. In sample E7-49.1 and E7-49.2 branchiae, intestines and ganglia were visible, but hepatopancreases and gastrice were decomposed. Muscles were pink in color. On day 77 only the intestine of sample E7-77.1 was decomposed and muscles were pulpy. Muscles seemed to be unaltered in sample E7-77.2, where the intestine is still visible. On day 105 both carcasses were soft and jellylike, muscles were pulpy and every internal structure was decomposed except the branchiae. See also **Supplementary Table S3.7** and **S4.7**.

Exp. 8 (4°C / sterile water and sediment /anaerobic)

On day 7 both carcasses had changed their coloration from blue to red and only the hepatopancreases and gastrice were decomposed. On day 14 no changes could be detected in sample E8-14.1 and E8-14.2. On day 21, the cuticle of the cephalothorax of sample E8-21.1 showed an unnatural green color and the hepatopancreas as well as the gastric were decomposed. Sample E8-21.2 showed no changes. On day 49 only the digestive glands and the gastric were decomposed and muscles were pink in color. From this time forward all samples of experiment 8 had changed their olfactory properties and smelled. In addition, the cuticles of

the cephalothorax were blue in color and the cuticle of the pleons were red, except the cuticle of the cephalothorax of sample E105.1 and E105.2, which were unnatural green. On day 77 the hepatopancreas was decomposed in both samples but the gastric was only decomposed in sample E8-77.2. In addition, in both carcasses muscles were pink in color. On day 105 muscles were pink and the cuticles of the cephalothorax and the pleon were soft and jellylike. Chelipeds were still solid and every internal structure seemed to be unaltered (**Figure 10**) except the hepatopancreases and the gastrice, which were decomposed. See also **Supplementary Table S3.8** and **S4.8**.
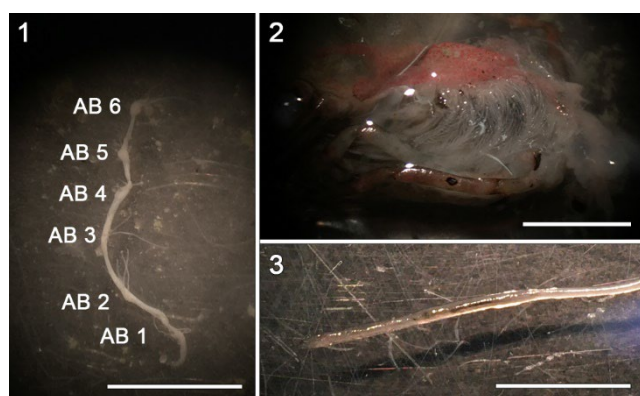
FIGURE 10. Crayfish remains of sample E8-105.1 on day 105. **10.1** Abdominal nerve cord (AB). **10.2** Left branchiae. **10.3** Part of the intestine. *Scale bar* 0.25 cm.

Micro-Computed Tomography (µ-CT)

µ-CT images revealed a precipitation of crystal clusters only inside the carcasses of experiments which were conducted under 24°C (Exp. 1; Exp. 2; Exp. 5 and Exp. 6). Crystal clusters precipitated in the chelipeds of sample E2-21.2 after two days already. As the decay proceeded, crystalline structures were observed at the ventral side of the cephalothorax, inside the pereiopods, inside the coxa of the pleopods, along the ventro-lateral side of the tergites, in the telson, and the uropods. In addition, µ-CT images revealed that these crystal clusters only precipitated at the inner side of the cuticles. All scanned specimens of Exp. 1 and Exp. 2 (E1-21.1 to E2-21.3) contained one pair of gastroliths inside their gastric. Volume measurements of polygonal 3D-surface models of crystal clusters and gastroliths showed an increase of the volume of crystal clusters and a simultaneous volume reduction of gastroliths with progressive decay (**Figure 11** and **Supplementary Table S5.1** and **S6.1**). In experiments which were conducted under sterile conditions (Exp. 2 and Exp. 6) a smaller total volume of crystal clusters was observed, as in experiments conducted with untreated sediment and water (Exp. 1 and Exp. 5). In addition, the TVC in Exp. 6 decreased before the end of the experiment (**Figure 12** and **Supplementary Table S5.1**).
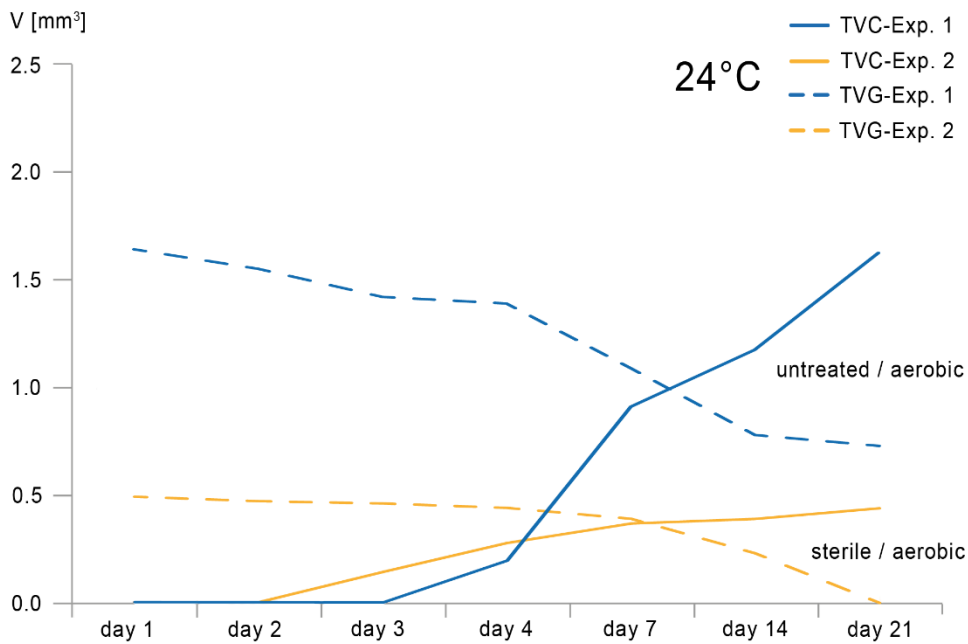
FIGURE 11. Mean values of volume increase of TVC and the volume decrease of TVG of samples of Exp. 1 in comparison to the values of samples of Exp. 2 for a duration of 21 days at 24°C (Dataset can be found in **Supplementary Table S5.1** and **6.1**). **TVC**, total volume of calcite; **TVG**, total volume of gastroliths.
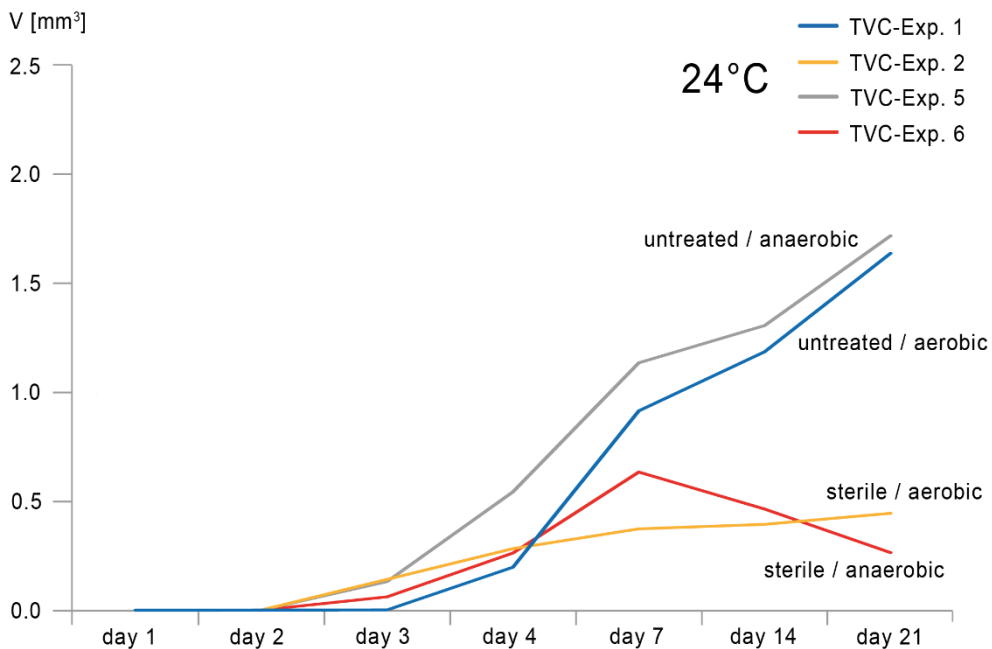
FIGURE 12. Comparison of mean values of volume increase of TVC of samples of Exp. 1, Exp. 2, Exp. 5 and Exp. 6 for a duration of 21 days at a constant temperature of 24°C (Dataset can be found in **Supplementary Table S5.1**). **TVC**, total volume of calcite.

Only E3-105.1 and E4-105.2 of the scanned specimen of Exp. 3 and Exp. 4 contained one pair of gastroliths inside their gastric. Volume measurements of polygonal 3D-surface models of gastroliths showed a "faster" volume reduction of gastroliths under 24°C than under 4°C, with progressive decay (**Figure 13** and **Supplementary Table S6.1-2**). In addition, no precipitation of calcite could be observed in individuals of experiments which were conducted at a temperature of 4°C (Exp. 3; Exp. 4; Exp. 7 and Exp. 8) (**Supplementary Table S5.2**).
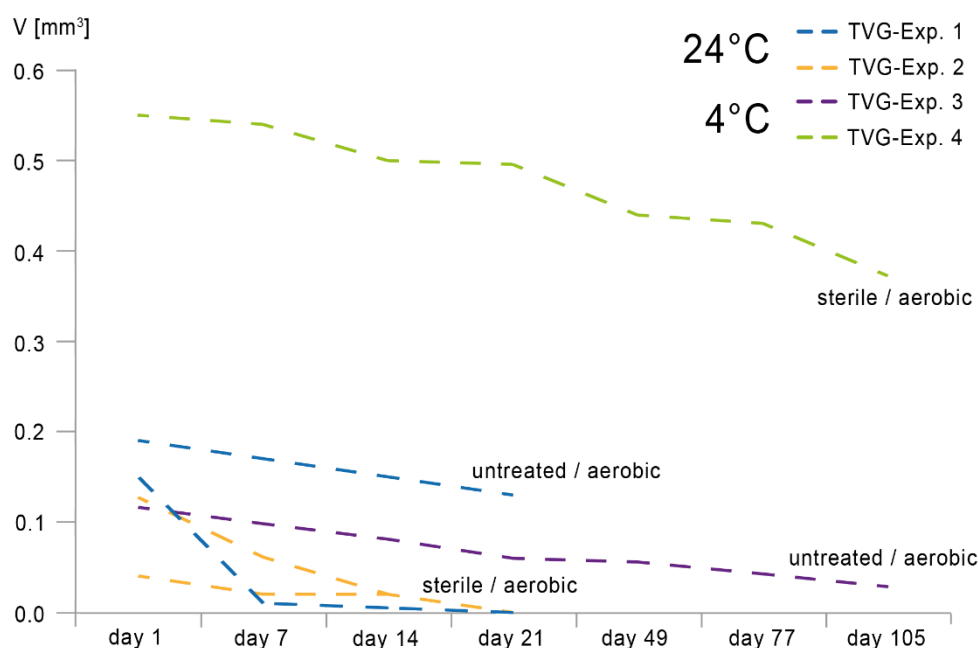
FIGURE 13. Comparison of median values of volume decrease of TVG of samples of Exp. 1 and Exp. 2 for a duration of 21 days at 24°C and of samples of Exp. 3 and Exp. 4 for a duration of 105 days at 4°C. (Dataset can be found in **Supplementary Table S6.1** and **S6.2**). **TVG**, total volume of gastrolith.

Inductively Coupled Plasma Mass Spectrometry (ICPMS)

ICPMS measurements revealed that in all experimental solutions the calcium content increased with progressive decay (**Figure 14** and **15**). In addition, solutions of Exp. 2 show the highest calcium content in experiments, which were conducted at a constant temperature of 24°C with a duration of 21 days (**Figure 14**). Further on, solutions of Exp. 3 show the highest calcium content in experiments, which were conducted at a constant temperature of 4°C with a duration of 105 days (**Figure 15**). At the end of the experiments the calcium content of all check plots was higher than at the start of the study (**Figure 14** and **15** and **Supplementary Table S2.1-8**).
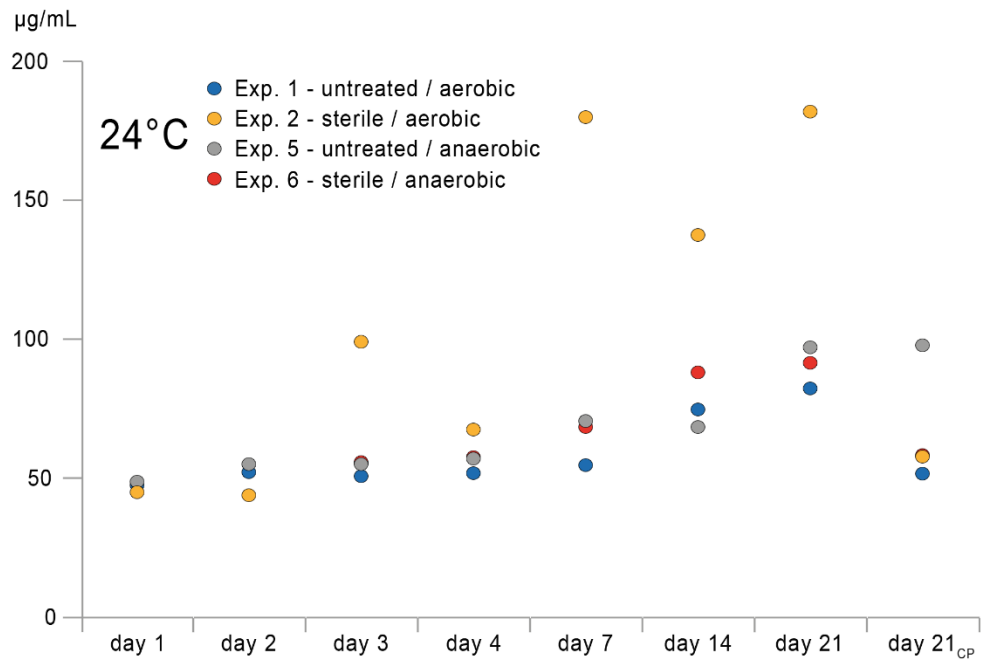
FIGURE 14. Mean values of calcium enrichment in solutions of Exp. 1, Exp. 2, Exp. 5 and Exp. 6 show an increase of calcium (^{43}Ca) with progressive decay. (Dataset can be found in **Supplementary Table S2.1-2** and **S2.5-6**).
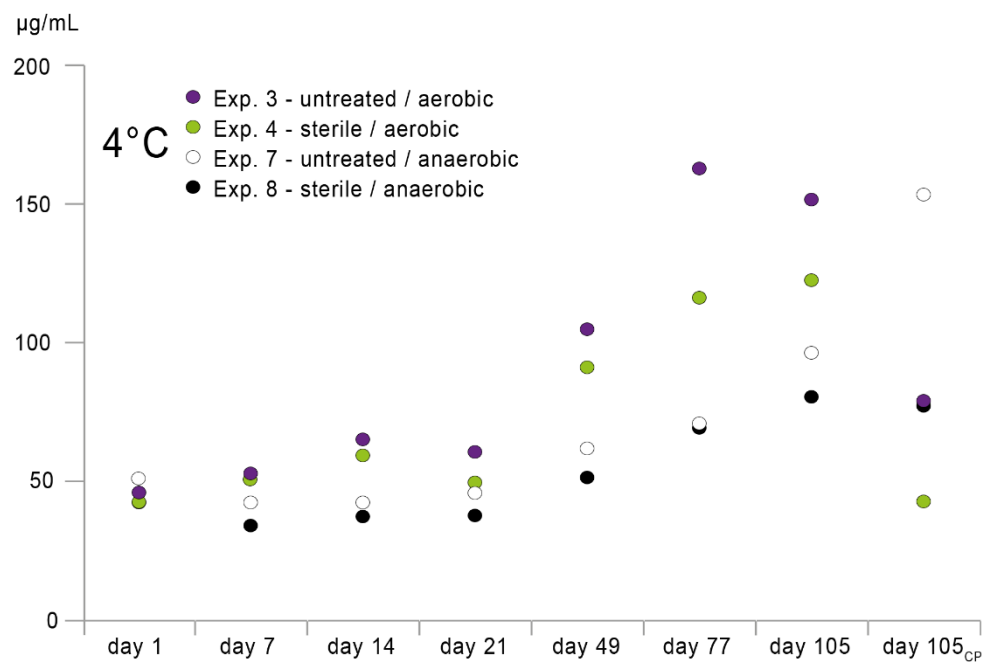
FIGURE 15. Mean values of calcium enrichment in solutions of Exp. 3, Exp. 4, Exp. 7 and Exp. 8 show an increase of calcium (^{43}Ca) with progressive decay. (Dataset can be found in **Supplementary Table S2.3-4** and **S2.7-8**).

Confocal Raman Spectroscopy (CRS)

Raman analyses clearly revealed that the crystal clusters (**Figure 16**) consist of well-ordered calcite (**Figure 16**), which can be identified by the fully symmetric $v_1(CO_3)$ carbonate band near 1085 cm^{-1}, as well as the presence of lattice vibrations near 154 and 281 cm^{-1}, with the latter being absent in amorphous calcium carbonate (ACC). Raman analyses clearly show that the crystal cluster consist out of crystalline calcite (**Figure 16**), whereby a mixed spectrum of crystalline calcite and the β-carotene, astaxanthin (AXT) could be identified by the typical high intensity modes at ~1157 and ~1517 cm^{-1} that are assigned to the C=C and C-C stretching vibrations of the polyene chain bonds, respectively (Kaczor et al. 2011, Subramanian et al. 2014, Saito & Tasumi 1983). In comparison to the spectrum obtained from the AXT standard, small derivation in the frequency of the ~1517 cm^{-1} are to observe. Such shift can be presumably linked to the structural differences in the AXT.
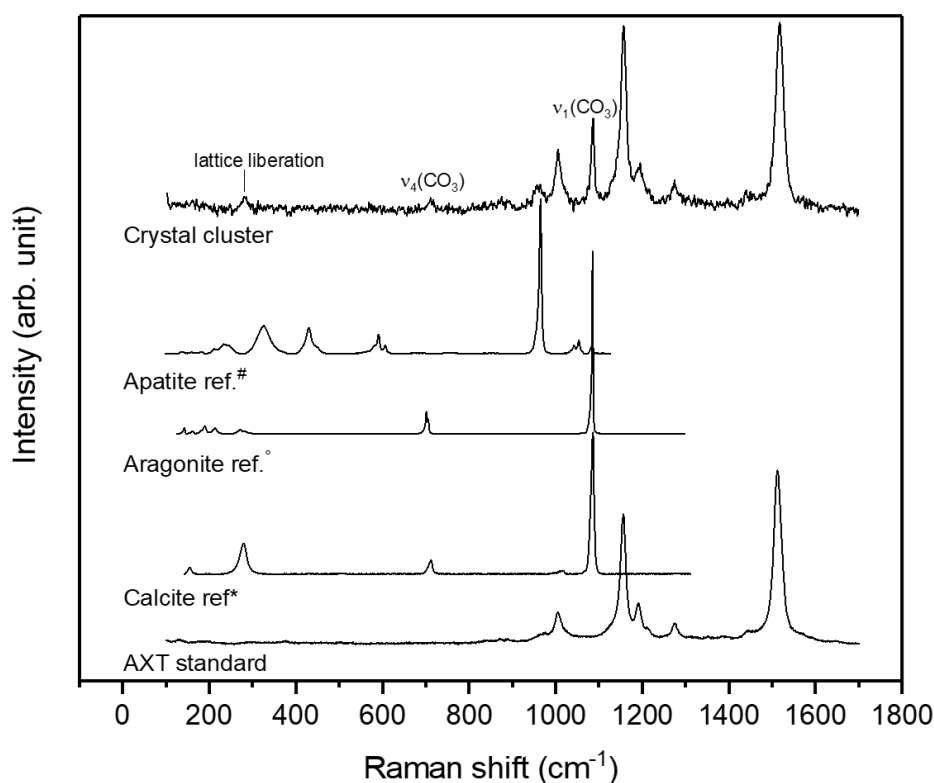
FIGURE 16. Representative Raman spectra of observed crystal clusters compared to Raman reference spectra of crystalline apatite, aragonite and calcite, taken from the RRUFF Raman data base ([#]R060070, [°] R060070, *R040170 Laetsch & Downs, 2006). Raman spectra of the crystal clusters exhibit main Raman bands typically for crystallized calcite and the β-carotene, astaxanthin.

Scanning Electron Microscopy (SEM)

SEM-images show several structures of precipitated calcite clusters varying in sizes from 100 μm to 900 μm at the end of the experiment. Most of these structures are spherical or bispherical. The largest cluster is semi-circular with mineralized cuticle remains and mineralized plumose setae (**Figure 17.1-2**). Another calcite cluster is of conical shape (**Figure 17.3-4**).
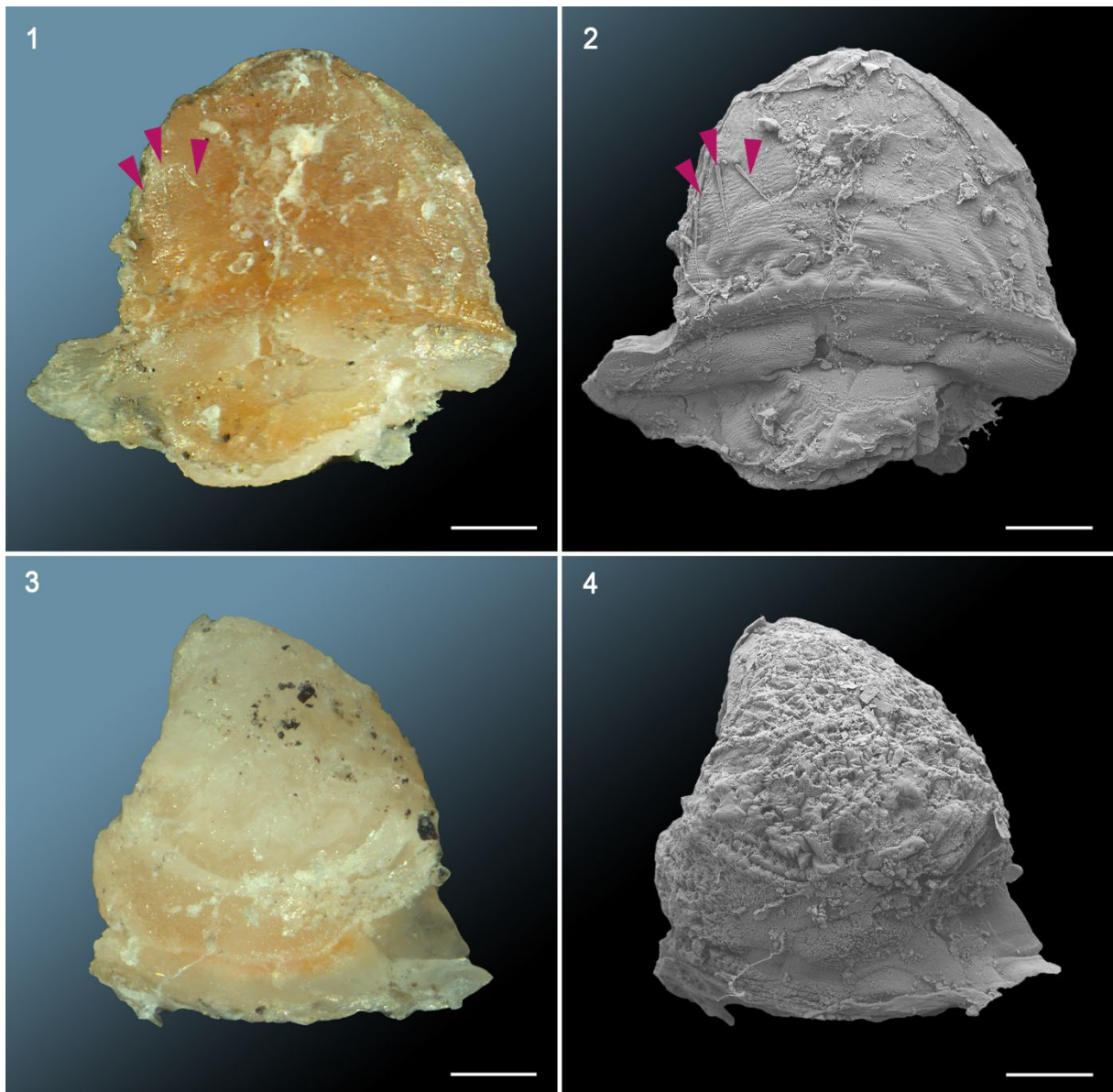
FIGURE 17. Stereoscopic and SEM images of calcite clusters found in *C. diminutus* E1-21.2 at the end of Exp. 1. **17.1** Stereoscopic image of a semi-circular calcite cluster with three mineralized setae (pink arrows). **17.2** SEM-image of the cluster shown 17.1. **17.3** Stereoscopic image of a conical calcite cluster. **17.4** SEM-image of the cluster shown in 17.3. *Scale bar* of **17.1-2** 200 μm, **17.3-4** 100 μm.

5.4 Discussion

During the optical observation it was noticed, that in all experimental setups (except Exp. 1) the crayfish carcasses remained articulated, nevertheless the internal organs decomposed and the cuticles became jelly-like (24°C) or soft (4°C) with progressive decay. Such fully articulated carcasses, that died under low temperature conditions with soft cuticles and decomposed organs might enter the fossil record and might be misinterpreted as moults. In experiments which were conducted under a constant temperature of 24°C crayfish carcasses collapsed while trying to get them out of the flacon tubes. In addition, smooth water movements resulted in a separation of pleon and cephalothorax, a disarticulation of the pereiopods and chelipeds and/or a twist of the chelipeds. These occurrences in combination with a poor preservation in the fossil record might result in misinterpretations of fossil decapods. In addition, with progressive decay an accumulation of putrefaction gas occurred at the gill area of sample E1-21.1 and E1-21.3 of Exp. 1 (24°C / aerobic / untreated). Caused by the decomposition of soft tissue and continuously gas accumulation, the cephalothorax of sample E1-21.1 was detached from the carcass and floated on the surface. In sample E1-21.3 the cephalothorax was partly detached and floated also on the surface holding the remains of the dangling body. Such crayfish remains seems to be rarely fossilized, but sometimes in the fossil record decapods were found often described as moults, in which the cephalothorax is detached or partly detached from the carcass (Feldmann and McPherson, 1980; **Figure 18.2**). Maybe in some rare cases these fossils are a result of gas accumulation around the gills during the decay process.
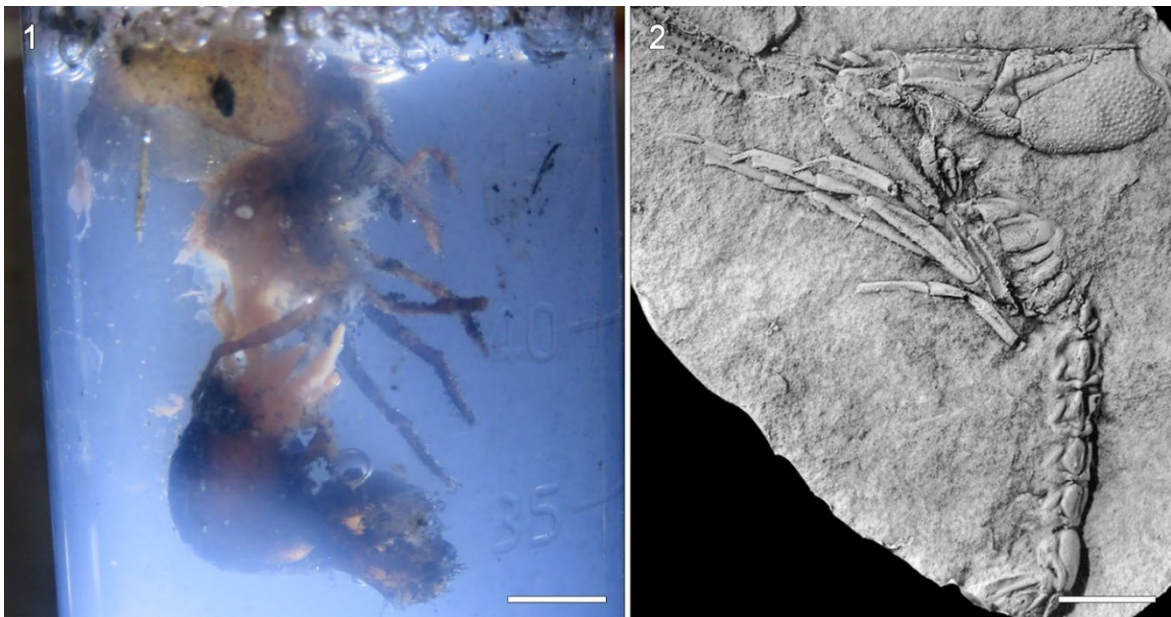
FIGURE 18. Comparison of a fresh decomposing crayfish with a fossil moult. **18.1** *Cambarellus diminutus* decomposing in freshwater on day 21. **18.2** *Glyphea robusta* collected from the Jurassic of northern Canada (Feldmann and McPherson, 1980). *Scale bar* 1 cm.

Anaerobic and especially reducing conditions are commonly assumed to slow soft tissue degradation (Raff et al., 2006, 2008; Gostling et al., 2009; Hippler et al., 2011; Butler et al., 2015; Eagan et al., 2017), by inhibiting autolytic enzymes responsible for initial decay processes and excluding external scavengers and thus bioturbation (Plotnick et al., 1986; Kidwell & Baumiller, 1990; Raff et al., 2014). However, the experiments of this study show a comparable tissue decomposition under aerobic as well as under partly anaerobic conditions at 24°C. Even if the water was not complete anaerobic in Exp. 3, 4, 7 and 8, the oxygen content was significantly lower than under aerobic conditions (**Supplementary Table S4.1-8**). In most cases inner organs were completely decomposed and muscle tissue were pulpy after 7 days. Only gastrice and hepatopancreases were decomposed 3 to 4 days earlier, whereby gastrice decomposed faster if more oxygen is available. At 4°C gastrice and hepatopancreases decomposed much faster under partly anaerobic (7 days) than under aerobic (49 days) conditions. Also, intestines and ganglia decomposed faster under partly anaerobic conditions at 4°C unless sterile conditions prevailed. It seems that the decomposition of soft tissues is not only addicted to oxygen but also depends on the temperature, the tissue type and of course the microbial community.

With progressive decay calcite precipitation occurred at the inner side of the cuticles in all individuals (except E2-21.1) which decomposed at 24°C. Mineral precipitation is often an important step in soft tissue preservation (Briggs & Kear, 1993a; 1994). The results of the experiments presented here, conducted with untreated sediment and water under aerobic (Exp. 1) and partly anaerobic (Exp. 5) conditions at 24°C, show a higher total volume of calcite (TVC) than the results of Exp. 2 (aerobic) and Exp. 6 (anaerobic), conducted with sterile sediment and water at 24°C. In addition, the TVC in Exp. 6 decreased inside the specimens after 7 days, which might be explained by an acidification of the pH-value through microbial activity inside the specimens.

For crayfish the precipitation of calcite depends on the body size, moulting cycle, and/or the moulting stage (Mähler et al., 2020). At the beginning of the moulting phase, calcium ions from the cuticle are transported through the haemolymphatic circulatory system into the cardiac stomach wall, where gastroliths are formed, which consist of a network of protein-chitin fibers and amorphous calcium carbonate (ACC) (Shechter et al., 2008; Luquet, 2013). These calcium ions are therefore only available to a limited extent for the calcite precipitation after death (Mähler et al., 2020). However, since the compared individuals rarely differed in body size (see **Supplementary Table S1)** and moulting stages, these factors cannot explain the significant differences in calcite precipitation.

Furthermore, ICPMS analysis revealed that the calcium content inside the lake water increased with progressive decay (**Figure 14** and **15**) and increased more in experiments with low calcite precipitation. However, it could not be clarified whether the dissolved calcium ions came from the animals themselves or form the sediment, which contained various calcium-rich shell remains of bivalves, snails, and small crustaceans such as ostracods (**Figure 1**).

The results of the microbiome sequencing revealed an occurrence of the genus *Proteocatella* in the samples of Exp. 1 and Exp. 3 (untreated) which was absent in Exp. 2 and Exp. 4 (sterile) (Janssen, 2021).

So far, only the type species, *Proteocatella sphenisci*, has been cultured; it was isolated from the excretions of the Magellan penguin (*Spheniscus magellanicus*, Pikuta et al., 2009) which feed on fish and crustaceans. Uncultured members of the genus *Proteocatella* have been described from wastewater, rivers and drinking water and gut microbiota (Slobodkin, 2014; Huang et al., 2014; Barragan-Trinidad and Buitron, 2020). However, the genus also forms a part of the microbiome of carbonized thrombolites found in shallow, subpolar freshwater Laguna Larga in southern Chile (Graham et al., 2014). Another interesting fact is that *Proteocatella spp.* is known as a component of feline (Dewhirst et al., 2015) and canine (Dehwirst et al., 2012; Ruparell et al., 2020) dental plaque. Therefore, species of the genus *Proteocatella* might have supported the calcite precipitation in crayfish carcasses of Exp. 1 and Exp. 3. A precipitation of calcite has not been observed under 4°C conditions, although it can occur even at such low temperatures by certain groups of bacteria (Elster et al., 2016). Psychrotolerant bacteria are able to tolerate temperatures from -15°C (Pearce, 2012) and might have the ability to degrade or mineralize organic matter.

During the experiments, cuticles changed their coloration from blue to red (**Supplementary Tables S3.1-8**). The coloration change is caused by the ketocarotenoid Astaxanthin (AXT) [3,3'-dihydroxy-β,β carotene-4,4' dione]. In living crustaceans AXT is ligated to the α-crustacyanin protein complex, located in the upper cuticle layer of the exocuticle (see chapter 1.2.4). If the protein complex is intact the carapace shows a blue coloration. During the decay process, the protein complex can be denaturized, caused by autolytic enzymes and/or bacterial degradation. If the protein complex is denaturized AXT molecules will be uncombined resulting in a red coloration of the cuticle (Korger, 2005). AXT, once uncombined from the α-crustacyanin protein complex, distributed throughout the cuticle layers from the outside (exocuticle) to the inside (endocuticle) (Mähler and Lönartz et al., in prep.). In the experiments described here AXT was additionally proved in precipitated calcite clusters, that were discolored by this ketocarotenoid (**Figure 16** and **17.1** and **17.3**).

Because, AXT works against a variety of gram + and gram – pathogens like *Pseudomonas* sp., *Bacillus* sp., *Salmonella* sp., and *Staphylococcus* sp. (Ushakumari & Ramanuja, 2013), *Helicobacter* sp. (Bennedsen et al., 1999; Wang et al., 2000), *Clostridium* sp. and *Enterobacteriaceae* (Waldenstedt et al., 2003; Zhang et al., 2020), the influence of AXT on bacteria and other microorganisms involved in decomposition or mineralization should be investigated in further studies. For example, whether AXT has an inhibitory effect on certain bacteria or if it could even act as a biofilm inhibitor from a certain concentration.

In this context, the amount of AXT taken up by nutrition, might be an interesting point, because AXT, like other carotenoids, cannot be produced by the animals themselves (Jyonouchi et al., 1995). In nature AXT is biosynthesized by microalgae, phytoplankton, fungi and bacteria, particularly in marine environments (Yaun et al., 2011), but it is also produced by freshwater microalgae e.g., *Chlorella sorokiniana* (Raman & Mohamad, 2012) and *Haematococcus pluvialis* (Harker et al., 1996). In *H. pluvialis* AXT production is even increased under extreme environmental conditions (e.g., low nitrate and phosphate or high salinity; Harker et al., 1996). If AXT had an influence on the decomposition process or bacterial growth in our experiments is not known. Although the feed contained components of the algae *H. pluvialis*, it was not known how much AXT was inside the "feeding loops" and how much AXT was taken up by each crayfish individually.

5.5 Conclusion

All crayfish carcasses stayed articulated till the end of the experiments, although inner organs decomposed and cuticles became soft (4°C) and jellylike (24°C) with progressive decay.

A gas accumulation which occurred 3 days after the regular study-period at 24°C in untreated lake water under aerobic conditions resulted in a floating of the carcass or detaching of the cephalothorax. At 24°C the oxygen content had a minimal influence on the decay whether the medium was untreated or sterile. At 4°C gastric, hepatopancreas, intestine and general nerve cord decomposed only or earlier under partly anaerobic conditions. Abdominal muscles decomposed only when intestines were decomposed. Calcite precipitation was higher in untreated water than in sterile water. Caused by microbiological investigations it is assumed that the bacterial genus *Proteocatella* might be responsible for the differences in calcite precipitations. Therefore, the decomposition of soft tissues in the here presented study is a complex interplay between tissue type, temperature, oxygen level and microbial composition.

Chapter 6

General Discussion and Conclusion

Mineral precipitation (e.g., calcite, aragonite) during the decomposition of crustacean in artificial seawater under laboratory conditions is early digenetic and often occur before soft tissues are mineralized (Briggs and Kear, 1993a; 1994; Hof and Briggs, 1997; Sagemann et al., 1999). This process is major controlled by pH alterations caused by autolysis and microbial activity during the decomposition. Mineral precipitations occur as calcite clusters in crustacean fossils with soft tissue preservation discovered from marine deposits but also from freshwater fossil sites (Briggs and Wilby, 1996).

ICPMS measurements of this study revealed that during the decomposition of *Cambarellus diminutus* in freshwater (tank, distilled and lake water (untreated and sterile)) calcium ions were dissolved out of the cuticle layers and were released into the surrounding medium (**Figure 14 and 15**; **Supplementary Table S2.1-8**; **Table AS 2** and **3**; **Figure AS 2**) and into the body cavity in order to precipitate as calcite clusters at the inner side of the cuticle (Mähler et al., 2020). It could be shown that the amount of body calcium can be sufficient for partial mineralization of soft tissues, because calcite precipitation and muscle mineralization (**Figure AI 3**) not only occurred in tank water, but also in distilled water, in which the amount of calcium ions was under the detection limit (Mähler et al., 2020). The cuticle of a crayfish hosts the highest amount of calcite during the intermoult phase where it can easily be dissolved after death. In living crayfish, initially to each premoult phase calcium ions are dissolved out of the cuticle layers and transported via the haemolymphatic circulatory system into the stomach (Ahearn et al., 2004). Inside the cardiac stomach wall calcium ions precipitated as amorphous calcium carbonate (ACC) and form gastroliths (Travis, 1963; Luquet, 2013). After moulting, where substantial quantities of calcium ions are released to the environment, gastroliths are dissolved and calcium ions are transported to the new cuticle for restabilization. So, the amount of precipitated calcite during the decomposition depends on the stage of moulting and therefore on the amount of calcium ions inside the haemolymphatic circulatory system and the cuticle layers (Mähler et al., 2020). In addition, if calcium ions are bound as gastroliths they are only available to a limited extant for precipitation. Another aspect might be the expression of calcium-binding peptides during the postmoult phase (Inoue et al., 2004). Depending on the amount of these peptides at the time of death, precipitation of calcite might be inhibited. In individuals that were in the intermoult phase at the time of death the cuticle hosts the highest amount of calcium ions and therefore the body size was an important factor (Mähler et al.,

2020). However, the amount of precipitated calcite may also depend on dietary calcium intake prior to death and possibly on sex, as Sourie and Chaisemartin (1961) found a higher amount of calcium in the hemolymph of male crayfish than of females.

ICPMS analyses revealed that in distilled as well as in tank water a comparable amount of calcium ions was released into the environment during the decomposition of *C. diminutus*. In addition, a higher volume of precipitated calcite was observed in individuals which decomposed in tank water than in distilled water. It is assumed that in tank water Ca^{2+} from the surrounded medium diffused inside the crayfish with a simultaneously calcium dissolution out of the carapace into the medium. But this thesis must be validated by further studies.

Another reason, which seems more plausible might be a different composition of microorganisms inside tank water and distilled water.

This assumption is supported by the results of chapter 5 in which less calcite precipitated under sterile conditions at the inner side of the cuticle of the crayfish than in individuals that decomposed in untreated lake water. 16S rRNA gene amplicon analysis of untreated and sterile lake water used in chapter 5 revealed that the bacterial genus *Proteocatella* was only proven in samples of untreated lake water and sediment (Janssen, 2021). So far only the type species *Proteocatella sphenisci* has been cultured and is known as a part of the microbiome of carbonized thrombolites found in the shallow, subpolar freshwater of Laguna Larga in southern Chile (Graham et al., 2014) and is a component of feline (Dehwirst et al., 2015) and canine dental plaque (Dehwirst et al., 2012; Ruparell et al., 2020). Therefore, it is assumed that *Proteocatella* promote or induced the precipitation of calcite during the experiments. The results of chapter 4 show that biofilms, composed out of bacteria and fungi (mainly composed of the bacterial genus *Sphaerotilus* and the fungi genus *Pluteus*) are able to manipulate calcite precipitation. Whereas inside a biofilm, calcite crystals precipitated fine grained in and at the inner side of the cuticle, with a better replication of the cuticle structure, they precipitated coarser in individuals that decomposed without a biofilm formation (Chapter 4 **Figure 6** and Mähler et al., 2020). In addition, the digestive glands were transformed into adipocere in all individuals, that were enveloped by a biofilm and were completely decomposed in any other crayfish without a biofilm formation (Chapter 4). Adipocere is the result of the incomplete hydrolyses of fat in animal tissue by bacterial activity and might be a key component in the outstanding preservation of fossils in Konservat-Lagerstätten (Schwermann et al., 2012; Reisdorf & Wuttke, 2012).

The question if extrinsic or intrinsic bacteria promote decay or preservation is difficult to answer. Whereas Butler et al. (2015) showed the mineralization of soft tissues only after the

gut wall ruptured and gut bacteria escaped into the body cavity, the results of chapter 5 show a decomposition of abdominal muscles, whenever the intestine was decomposed. Eagan et al. (2017) revealed that the individual microbiome can differ and therefore promote mineralization or decay.

It has been widely assumed that anaerobic conditions slow-down soft tissue degradation (Raff et al., 2006; Gostling et al., 2009; Eagan et al., 2017), as they inhibit autolytic enzymes and exclude scavengers. However, the results of the studies shown in chapter 5 revealed a comparable decomposition of soft tissues under partly anaerobic as well as under aerobic conditions at 24°C. But under lower temperatures (4°C) gastrice, hepatopancreases, intestines and ganglia decomposed faster under partly anaerobic conditions unless sterile conditions prevailed. It seems that soft tissue preservation in *C. diminutus* is a complex interplay of tissue type, abiotic factors and the composition of involved microbial communities.

During the decomposition of *C. diminutus* in freshwater (tank water, distilled water, sterile and untreated lake water) gastroliths were dissolved with progressive decay or replicated as pseudomorphs of cauliflower like structure (**Figure AI 4.3**). In contrast, fossil opalized gastroliths discovered from the Cretaceous Griman Creek Formation, in Australia (Bell et al., 2019) were of round shape and does not show any cauliflower like structure. Bell et al., (2019) assumed that premoult individuals were eaten by birds and fish, so that gastroliths were excreted and could later be opalized. Another theory might be the exposure of the gastroliths by ostracods. The results of chapter 4 revealed that gastroliths dropped out of the crayfish carcasses after the cephalothorax and main inner organs were degraded by ostracod invasion.

References

Ahearn, G.A., Mandal, P.K. & Mandel, A. (2004). Calcium regulation in crustaceans during the molt cycle: a review and update. *Comparative Biochemistry and Physiology* **Part A**, 247-257.

Allen, A.L.C., Romero-Mangado, J., Adams, S., Flynn, M., Chen, B. & Zhang, J. Z. (2018). Detection of saturated fatty acids associated with a self-healing synthetic biological membrane using fiber-enhanced surface enhanced Raman scattering. *The Journal of Physical Chemistry B* **122**, 8396-8403.

Allison, P.A. (1988). The role of anoxia in the decay and mineralization of proteinaceous macro-fossils. *Paleobiology* **2**, 139–154.

Arp, G., Reimer, J. & Reitner, J. (2003). Microbialite formation in seawater of increased alkalinity, Satonda Crater Lake, Indonesia. *Journal of Sedimentary Research* **73**, 105–127.

Bade, M.L. & Stinson, A. (1978). Activation of old cuticle chitin as a substrate for chitinase in the molt of Manduca. *Biochemical and Biophysical Research Communications* **84**, 381-388.

Barbieri, G., Albertini, A.M., Ferrari, E., Sonensheim, A.L. & Belitsky, B.R. (2016). Interplay of CodY and ScoC in the regulation of major extracellular protease genes of *Bacillus subtilis*. *Journal of Bacteriology* **198**, 907–920.

Barragán-Trinidad, M. & Buitrón, G. (2020). Hydrogen and methane production from microalgal biomass hydrolyzed in a discontinuous reactor inoculated with ruminal microorganisms. *Biomass and Bioenergy* **143**, 105825.

Bartley, J.K. (1996). Actualistic taphonomy of Cyanobacteria: Implications for the Precambrian fossil record. *PALAIOS* **11**, 571–586.

Bell, P.R., Bicknell, R.D.C. & Smith, E.T. (2019). Crayfish bio-gastroliths from eastern Australia and the middle Cretaceous distribution of Parastacidae. *Geological Magazine* **157**, 1023-1030.

Bennedsen, M., Wang, X., Willén, R., Wadström, T. & Anderson, L.P. (1999). Treatment of H. pylori infected mice antioxidant astaxanthin reduces gastric inflammation, bacterial load and modulates cytokine release by splenocytes. *Immunology Letters* **70**, 185-189.

Berner, R.A. (1968). Calcium carbonate concretions formed by the decomposition of organic matter. *Science* **159**, 195-197.

Berner, R.A. (1970). Sedimentary pyrite formation. *American Journal of Science* **268**, 1-23.

Bokulich, N.A., Kaehler, B.D., Rideout, J.R., Dillon, M., Boylen, E., Knight, R., Huttley, G.A. & Caporaso, J.G. (2018). Optimizing taxonomic classification of marker-gene amplicon sequences with QIIME 2′s q2-feature-classifier plugin. *Microbiome* **6**.

Booth, J.M.; Fusi, M., Marasco, R., Michoud, G., Fodelianakis, S., Merlino, G. & Daffonchio, D. (2019). The role of fungi in heterogenous sediment microbial networks. *Scientific. Reports.* **9**, 7537.

Boylen, E. *et al.* (2019). Reproducible, interactive, scalable and extensible microbiome data science using QIIME 2. *Nature Biotechnology* **37**, 848-857.

Briggs, D. E. G. (2003). The role of decay and mineralization in the preservation of soft-bodied fossils. *Annual Review of Earth and Planetary Sciences* **31**, 275–301.

Briggs, D.E.G. & Kear, A.J. (1993a). Fossilization of soft tissue in the laboratory. *Science* **259**, 1439–1442.

Briggs, D.E.G. & Kear, A.J. (1993b). Decay of *Branchiostoma*. Implications for soft tissue preservation in conodonts and other primitive chordates. *Lethaia* **26**, 275-287.

Briggs, D.E.G. & Kear, A.J. (1993c). Fossilization of soft tissue in the laboratory. *Science* **259**, 1439-1442.

Briggs, D.E.G. & Kear, A.J. (1994). Decay and mineralization of shrimps. *PALAIOS* **9**, 431–456.

Briggs, D.E.G., & Wilby, P.R. (1996). The role of the calcium carbonate-calcium phosphate switch in the mineralization of soft-bodied fossils. *Journal of the Geological Society* **153**, 665–668.

Briggs, D.E.G., Moore, R.A., Schultz, J.W. & Schweigert, G. (2005). Mineralization of soft-part anatomy and invading microbes in the horseshoe crab *Mesolimulus* from the Upper Jurassic Lagerstätte of Nusplingen, Germany. *Proceedings B* **272**, 627-632.

Briggs, D.E.G., Rolfe, W.D.I., Butler, O.D., Liston, J.J. & Ingham, J.K. (2011). Phyllocarid crustaceans from the Upper Devonian Gogo Formation, Western Australia. *Journal of Systematic Palaeontology* **9**, 399-424.

Brinkmann, B. (2003). Tod im Wasser. In *Handbuch gerichtliche Medizin*. (eds. B. Madea & B. Brinkmann), pp. 796-819. Springer, Berlin, Heidelberg.

Butler, A.D., Cunningham, J.A., Budd, G.E. & Donoghue, P.C.J. (2015). Experimental taphonomy of artemia reveals the role of endogenous microbes in mediating decay and fossilization. *Proceedings of the Royal Society B: Biological Sciences* **282**, 1–10.

Callahan, B.J., McMurdie, P.J., Rosen, M.J., Han, A.W., Johnson, A.J.A. & Holmes, S.P. (2016). DADA2: High-resolution sample inference from Illumina amplicon data. *Nature Methods* **13**, 581-587.

Canfield, D.E. & Raiswell, R. (1991). Pyrite formation and fossil preservation. In *Taphonomy: Releasing the data locked in the Fossil Record.* (eds. P.A. Allison & D.E.G. Briggs), pp. 337-387. Plenum Press, New York.

Caporaso, J.G., Lauber, C.L., Walters, W.A., Berg-Lyons, D., Lozupone, C.A., Turnbaugh, P.J., Fierer, N. & Knight, R. (2011) Global patterns of 16S rRNA diversity at a depth of millions of sequences per sample. PNAS **108**, 4516-4522.

Clements, T., Purnell, M. & Gabbott, S. (2019). The Mazon Creek Lagerstätte: A diverse late Paleozoic ecosystem entombed within siderite concretions. *Journal of the Geological Society* **176**, 1-11.

De Gelder, J., De Gussem, K., Vandenabeele, P. & Moens, L. (2007). Reference database of Raman spectra of biological molecules. *Journal of Raman Spectroscopy* **38**, 1133-1147.

Dehwirst, F.E., Klein, E.A., Bennett, M.-L., Croft, J.M., Harris, S.J. & Marshall-Jones, Z.V. (2015). The feline oral microbiome: A provisional 16S rRNA gene based taxonomy with full-length reference sequences. *Veterinary Microbiology* **175**, 294-303.

Dehwirst, F.E., Klein, E.A., Thompson, E.C., Blanton, J.M., Chen, T., Milella, L., Buckley, C.M.F., Davis, I.J., Bennett, M.-L. & Marshall-Jones, Z.V. (2012). The canine oral microbiome. *Plosone* **7**, e36067.

Drach, P. (1939). Mue et cycle d'intermue chez les Crustacés Décapodes. (Molting and the intermolt cycle in Decapod Crustaceans). *Annales de l′Institut océanographique, Paris* **19**, 103-391.

Dowd, S.E., Sun, Y., Secor, P.R., Rhoads, D.D., Wolcott, B.M., James, G.A. & Wolcott, R.D. (2018). Survey of bacterial diversity in chronic wounds using Pyrosequencing, DGGE, and full ribosome shotgun sequencing. *BMC Microbiology* **8**.

Eagan, J.L., Andrews, M.E., Pearson, R.L., Turner, F.R., Raff, E.C. & Raff, R.A. (2017). Identification and modes of action of endogenous bacteria in taphonomy of embryos and larvae. *PALAIOS* **32**, 206–217.

Edgecombe, G.D. (2020). Arthropod Origins: Integrating Paleontological and Molecular Evidence. *Annual Review of Ecology, Evolution, and Systematics* **51**, 1-25.

Elster, J., Nedbalova, L., Vodrážka, R., Láska, K., Haloda, J. & Komárek, J. (2016). Unusual biogenic calcite structures in two shallow lakes, James Ross Island, Antarktika. *Biogeosciences* **13**, 535-549.

Esteve, M. & Herrera, F.C. (2000). Hepatopancreas alterations in *Litopenaeus vannamei* (Boone, 1939) (Crustacea: Decapoda: Penaeidae) experimentally infected with a *Vibrio alginolyticus* strain. *Journal of Invertebrate Pathology* **76**, 1-5.

Fechner, M.G.T. (1827). *Lehrbuch der theoretischen und praktischen Chemie* (ed. L.J. Thenard). Druck J.B. Kirchfeld, Leipzig.

Feldmann, R.M. & McPherson, C.B. (1980). Fossil decapod crustaceans of canada. *Geological survey of Canada* **79**.

Fiedler, S., Berns, A.E., Schwark, L., Woelk, A.T. & Graw, M. (2015). The chemistry of death – Adipocere degradation in modern graveyards. *Forensic Sciences International* **257**, 320-328.

Flach, K. (1980). Über zwei fossile Silphiden (Coleoptera) aus den Phosphoriten von Caylux. *Deutsche Entomologische Zeitschrift* **1**, 105-109.

Flemming, H.-C. & Wingender, J. (2010). The biofilm matrix. *Nature Reviews Microbiology* **8**, 623-633.

Forbes, S.L., Dent, B.B. & Stuart, B.H. (2005). The effect of soil type on adipocere formation. *Forensic Science International* **154**, 35-43.

Gäb, F., Ballhaus, C., Stinnesbeck, E., Kral, A.G., Janssen, K. & Bierbaum, G. (2020). Experimental taphonomy of fish – role of elevated pressure, salinity and pH. *Scientific Reports* **10**, 7839.

Gehling, J.G. (1999). Microbial mats in terminal Proterozoic siliciclastics: Ediacaran death masks. *PALAIOS* **14**, 40-57.

Ghasemi, Y., Rasoul-Amini, S., Kazemi, A., Zarrini, G., Morowvat, M.H. & Kargar, M. (2011). Isolation and characterization of some moderately halophilic bacteria with lipase activity. *Microbiology* **80**, 483-487.

Giraud-Guille, M.M. (1984). Cacification initiation sites in the crab cuticle: The interprismatic septa. An ultrastructural cytochemical study. *Cell and Tissue Research* **236**, 413-420.

Gostling, N.J., Dong, X. & Donoghue, P.C.J. (2009). Ontogeny and taphonomy: An experimental taphonomy study of the development of the brine shrimp *Artemia salina*. *Palaeontology* **52**, 169–186.

Graham, L.E., Knack, J.J., Piotrowski, J., Wilcox, L.W., Cook, M.E., Wellman, C.H., Taylor, W., Lewis, L.A. & Arancibia-Avila, P. (2014). Lacustrine *Nostoc* (Nostogales) and associated microbiome generate a new type of modern glotted microbialite. *Journal of Phycology* **50**, 280-291.

Grey, K., Moore, L.S., Burne, R.V., Pierson, B.K. & Bauld, J. (1990). Lake Thetis, Western Australia: An example of saline lake sedimentation dominated by benthic microbial processes. *Australian Journal of Marine and Freshwater Research* **41**, 275-300.

Grimes, S.T., Brock, F., Rickard, D., Davies, K.L., Edwards, D., Briggs, D.E.G. & Parkes, R.J. (2001). Understanding fossilization: Experimental pyritization of plants. *Geology* **29**, 123-126.

Hammes, F. & Verstraete, W. (2002). Key role of pH and calcium metabolism in microbial carbonate precipitation. *Reviews in Environmental Science & Biotechnology* **1**, 3-7.

Hancy, A.D. & Antcliffe, J.B. (2020). Anoxia can increase the rate of decay for cnidarian tissue: Using *Actinia equina* to understand the early fossil record. *Geobiology* **18**, 167–184.

Harker, M., Tsavalos, A.J. & Young, A.J. (1996). Factors responsible for astaxanthin formation in the chlorophyte *Haematococcus pluvialis*. *Bioresource Technology* **55**, 207-214.

Hertel, R., Meyerjürgens, S., Voigt, B., Liesegang, H., & Volland, S. (2017). Small RNA mediated repression of subtilisin production in Bacillus licheniformis. *Scientific Reports* **7**, 1–11.

Higuera-Ciapara, I., Félix-Valenzuela, L. & Goycoolea, F.M. (2006). Astaxanthin: A review of its chemistry and applications. *Critical Reviews in Food Science and Nutrition* **46**, 185-196.

Hippler, D., Hu, N., Steiner, M., Scholtz, G., & Franz, G. (2011). Experimental mineralization of crustacean eggs leads to surprising tissue conservation: new implications for the fossilization of Precambrian-Cambrian embryos. *Biogeosciences Discussions* **8**, 12051–12077.

Hirschler, A., Lucas, J. & Hubert, J-C. (1990). Bacterial involvement in apatite genesis. *Federation of European Microbiological Societies Microbiology Ecology* **73**, 211-220.

Hof, C.H.J., & Briggs, D.E.G. (1997). Decay and mineralization of mantis shrimps (Stomatopoda; Crustacea); a key to their fossil record. *Palaios* **12**, 420–438.

Horikoshi, K. (1999). Alkaliphiles: Some applications of their products for biotechnology. *Microbiology and Molecular Biology Reviews* **63**, 735-750.

Huang, L., Chen, B., Pistolozzi, M., Wu, Z. & Wang, J. (2014). Inoculation and alkali coeffect in volatile fatty acids production and microbial community shift in the anaerobic fermentation of waste activated sludge. *Bioresource Technology* **153**, 87-94.

Hussein, G., Sankawa, U., Goto, H., Matsumoto, K. & Watanabe, H. (2006). Astaxanthin, a carotenoid with potential in human health and nutrition. *Journal of Natural Products* **69**, 443-449.

Iniesto, M., Lopez-Archilla, A.I., Fregenal-Martínez, M., Buscalioni, A.D. & Guerrero, M.C. (2013). Involvement of microbial mats in delayed decay: An experimental essay on fish preservation. *PALAIOS* **28**, 56-66.

Iniesto, M., Laguna, C., Florín, M., Guerrero, M.C., Chicote, A., Buscalioni, A.D. & López-Archilla, A.I. (2015). The impact of microbial mats and their microenvironmental conditions in early decay of fish. *PALAIOS* **30**, 792-801.

Iniesto, M.I. (2016). *Microbial Mats: The implication of these microbial communities in early stages of fossilization.* Dissertation, Universidad Autonoma de Madrid.

Iniesto, M., Villalba, I., Buscalioni, A.D., Guerrero, M.C. & Lopez-Archilla, A.I. (2017). The effect of microbial mats in the decay of Anurans with implications for understanding taphonomic processes in the fossil record. *Scientific Reports* **7**, 45160

Inoue, H., Ohira, T., Ozaki, N. & Nagasawa, H. (2004). A novel calcium-binding from the cuticle of the crayfish, Procambarus clarkii. *Biochemical and Biophysical Research Communications* **318**, 649-654.

Janssen, K. (2021). *Der Einfluss bakterieller Aktivität auf die Präservierung und den Abbau von Weichgewebe.* Dissertation. Rheinische Friedrich-Wilhelms-Universität Bonn.

Jauvion, C., Bernard, S., Gueriau, P., Mocuta, C., Pont, S., Benzerara, K. & Charbonnier, S. (2020). Exceptional preservation requires fast biodegradation: thylacocephalan specimens from La Voulte-sur-Rhône (Callovian, Jurassic, France). *Palaeontology* **63**, 395–413.

Jyonouchi, H., Sun, S. & Gross, M. (1995). Effect of carotenoids on *in vitro* immunoglobin production by human peripheral blood mononuclear cells: Astaxanthin, a carotenoid without vitamin A activity, enhances *in vitro* immunoglobulin production in response to a T-dependent stimulant and antigen. *Nutrition Cancer* **23**, 171-183.

Kaczor, A. & Baranska, M. (2011). Structural changes of carotenoid astaxanthin in a single algal cell monitored in situ by Raman spectroscopy. *Analytical chemistry* **83**, 7763-7770.

Kharlamova, A., Saveliev, S., Kurtova, A., Chernikov, V., Protopopov, A., Boeskorov, G., Plotnikov, V., Ushakov, V. & Maschenko, E. (2016). Preserved brain of the woolly mammoth (*Mammuthus primigenius* (Blumenbach 1799)) from the Yakutian permafrost. *Quaternary International* **406**, 86-93.

Kidwell, S.M., & Baumiller, T. (1990). Experimental Disintegration of Regular Echinoids: Roles of Temperature, Oxygen and Decay Thresholds. *Paleontology* **16**, 247–271.

Klatt, C.G., Liu, Z., Ludwig, M., Kühl, M., Jensen, S.I., Bryant, D.A. Ward, D.M. (2013). Temporal metatranscriptomic patterning in phototrophic Chloroflexi inhabiting a microbial mat in a geothermal spring. *International Society for Microbial Ecology* Journal **7**, 1775-1789.

Klompmaker, A.A., Hyžny, M., Portell, R.W., Jauvion, C., Charbonnier, S., Fussell, S.S., Klier, A.T., Tejera, R. & Jakobsen, S.L. (2019). Muscles and muscle scars in fossil malacostracan crustaceans. *Earth-Science Reviews* **194**, 306-326.

Kolter, T. & Sandhoff, K. (1999). Sphingolipide-Ihre Stoffwechselwege und die Pathobiochemie neurodegenerativer Erkrankungen. *Angewendete Chemie* **111**, 1632-1670.

Korger, M. (2005). *Aggregationsverhalten von Carotinoiden in Membranen unilamellare Liposomen.* Dissertation an der Mathematisch-Naturwissenschaftlichen Fakultät der Heinrich-Heine-Universität Düsseldorf.

Krauland, W. (1943). Fettwachsbildung unter ungewöhnlichen Bedingungen. *Deutsche Zeitschrift für die Gesamte Gerichtliche Medizin* **36**, 179-189.

Krause, D. & Jachau, K. (2007). Späte Leichenveränderungen. In *Praxis Rechtsmedizin* (ed. B. Madea), pp. 45-48. Springer, Berlin, Heidelberg.

Laetsch, T. & Downs, R.T. (2006). Software for identification and refinement of cell parameters from powder diffraction data of minerals using the RRUFF project and American mineralogist crystal structure databases. *Abstracts from the 19th General Meeting of the International Mineralogical Association*, Kobe, Japan, 23-28 July 2006.

Lee, S.-Y. & Eom, Y.-B. (2016). Analysis of microbial composition associated with freshwater and seawater. *Biomedical Science Letters* **22**, 150-159.

Lippold, B. (2022, March 24). *ICPMS*. https://www.chemie.de/lexikon/ICP-MS.html 24.03.2022

Lippold, B. (2022, March 24). *Rasterelektronenmikroskopi*e. https://www.bionity.com/de/lexikon/Rasterelektronenmikroskop.html#Elektronenstrahlerzeugung

Lourdes Moreno de, M., Pérez, D., García, M.T. & Mellado, E. (2013). Halophilic bacteria as a source of novel hydrolytic enzymes. *Life* **3**, 38-51.

Luquet, G., Fernández, M.S., Badou, A., Guichard, N., Le Roy, N., Corneillat, M., Alcaraz, G. & Arias, J.L. (2013). Comparative ultrastructure and carbohydrate composition of gastroliths from Astacidae, Cambaridae and Parastacidae freshwater crayfish (Crustacea, Decapoda). *Biomolecules* **3**, 18-38.

Ma, X., Edgecombe, G. D., Hou, X., Goral, T., & Strausfeld, N. J. (2015). Preservational Pathways of Corresponding Brains of a Cambrian Euarthropod. *Current Biology*, **25**, 2969–2975.

Ma, X., Hou, X., Edgecombe, G.D. & Strausfeld, N.J. (2012). Complex brain and optic lobes in an early Cambrian arthropod. *Nature* **490**, 258–261.

Mah, T.F.C. & O´Toole, G.A. (2001). Mechanisms of biofilm resistance to antimicrobial agents. *Trends in Microbiology* **9**, 34–39.

Mant, A.K. (1987). Knowledge acquired from post-war exhumations. In *Death, Decay and Reconstruction: Approaches to Archaeology and Forensic Science*. (eds. A. Boddington, A.N. Garland & R.C. Janaway), pp. 65-78. Manchester University Press.

Martin, D., Briggs, D.E.G. & Parkes, R.J. (2003). Experimental mineralization of invertebrate eggs and the preservation of Neoproterozoic embryos. *Geology* **31**, 39–42.

Mähler, B., Schwermann, A.H., Wuttke, M., Schultz, J. & Martin, T. (2015). Four-dimensional virtopsy and the taphonomy of a mole from the Oligocene of Lake Enspel (Germany). *Palaeobiodiversity and Palaeoenvironments* **95**, 115-131.

Mähler, B., Janssen, K., Menneken, M., Tahoun, M., Lagos, M., Bierbaum, G., Müller, C.E. & Rust, J. (2020). Calcite precipitation forms crystal clusters and muscle mineralization during the decomposition of *Cambarellus diminutus* (Decapoda: Cambaridae) in freshwater. *Palaeontologia Electronica* **23**, 1–17.

McAdams, H.H., Srinivasan, B., & Arkin, A.P. (2004). The evolution of genetic regulatory systems in bacteria. *Nature Reviews Genetics* **5**, 169–178

McCobb, L.M.E., Duncan, I.J., Jarzembowski, E.A., Stankiewicz, B.A., Wills, M.A. & Briggs, D.E.G. (1998). Taphonomy of the insects from the insect bed (Bembridge Marls), late Eocene, Isle of Wight, England. *Geological Magazine* **135**, 553-563.

McDonald, D., M. N. Price, J. Goodrich, E. P. Nawrocki, T. Z. Desantis, A. Probst, G. L. Andersen, et al. (2012). An improved Greengenes taxonomy with explicit ranks for ecological and evolutionary analyses of bacteria and archaea. *ISME Journal* **6**, 610–618.

Miki, W. (1991). Biological functions and activities of animal carotenoids. *Pure and Applied Chemistry* **63**, 141-146.

Muscente, A.D., Schiffbauer, J.D., Broce, J., Laflamme, M., O´Donnell, K., Boag, T.H., Meyer, M., Hawkins, A.D., Huntley, J.W., McNamara, M., MacKenzie, L.A, Stanley, G.D., Hinman, N.W., Hofmann, M.H. & Xiao, S. (2017). Exceptionally preserved fossil assemblages through geologic time and space. *Gondwana Research* **48**, 164-188.

Naimark, E.B., Kalinina, M.A., & Boeva, N.M. (2018). Persistence of external anatomy of small crustaceans in a long term taphonomic experiment. *Palaios* **33**, 154–163.

Nanikawa, R. (1973). Über die Bestandteile von natürlichen und experimentell hergestellten Leichenwachsen. *Zeitschrift für Rechtsmedizin* **72**, 194-202.

Niu, L., Li, Y., Xu, L., Wang, P., Zhang, W., Wang, C., Cai, W. & Wang, L. (2017). Ignored fungal community in activated sludge wastewater treatment plants: Diversity and altitudinal characteristics. *Environmental Science and Pollution Research* **24**, 4185-4193.

O`Brien, T.G & Kuehner, A.C. (2007). Waxing grave about adipocere: Soft tissue change in an aquatic context. *Journal of Forensic Sciences* **52**, 294-301.

Ohtsuka, T., Kudoh, S., Imura, S. & Ohtani, S. (2006). Diatoms composing benthic microbial mats in freshwater lakes of Skarvsnes ice-free area, East Antarctica. *Polar Bioscience* **20**, 113–130.

Oren, A. (2002). Molecular ecology of extremely halophilic archaea and bacteria. *Federation of European Microbiology Societies Microbiology Ecology* **39**, 1-7.

Ortega-Hernández, J., Lerosey-Aubril, R., Losso, S.R. & Weaver, J.C. (2022). Neuroanatomy in a middle Cambrian mollisoniid and the ancestral nervous system organization of chelicerates. *Nature Communications* **13**, 410.

Parry, L.A., Smithwick, F., Nordén, K.K., Saitta, E.T., Lozano-Fernandez, J., Tanner, A.R., Caron, J.-B., Edgecombe, G.D., Briggs, D.E.G. & Vinther, J. (2017). Soft-bodied fossils are not simply rotten carcasses – towards a holistic understanding of exceptional fossil preservation. *BioEssays* **40**, 1700167.

Pearce, D.A. (2012). Extremophiles in Antarctica: Life at low temperatures. In *Adaption of Microbial Life to Environmental Extremes* (eds. H. Stan-Lotter & S. Fendrihan) pp. 87-118. Springer Wien, New York.

Penning, R. (2006). *Rechtsmedizin systematisch*. (ed. R. Penning) Uni Med-Verlag Bremen.

Pfeifer, S., Milne, S. & Stevenson, R.M. (1998). The natural decomposition of adipocere. *Journal of Forensic Science* **43**, 368-370.

Pikuta, E.V., Hoover, R.B., Marsic, D., Whitman, W.B., Lupa, B., Tang, J. & Krader, P. (2009). Proteocatella sphenisci gen. nov., sp. nov., a psychrotolerant, spore-forming anaerobe isolated from penguin guano. *International Journal of Systematic and Evolutionary Microbiology* **59**, 2302-2307.

Plank, R., Cansiz, E., Urabe, H., Bode, M., Nagano, T., Nakamura, H. & Habe, T. (2022, March 24) *What is Raman Spectroscopy?*. https://www.horiba.com/deu/raman-imaging-and-spectroscopy/?MP=1547-1631

Plotnick, R.E. (1986). Taphonomy of a modern shrimp: implications for the arthropod fossil record. *Palaios* **1**, 286–293.

Prieto-Barajas, C.M., Valencia-Cantero, E., Santoyo, G. (2018). Microbial mat ecosystems: Structure types, functional diversity, and biotechnological application. *Electronic Journal of Biotechnology* **31**, 48-56.

Prokop, O. & Göhler, W. (1975). *Forensische Medizin*. Verlag Volk und Gesundheit, Berlin

Quast, C., Pruesse, E., Yilmaz, P., Gerken, J., Schweer, T., Yarza, P., Peplies, J. & Glöckner, F.O. (2012). The SILVA ribosomal RNA gene database project: Improved data processing and web-based tools. *Nucleic Acids Res*earch **41**, D590-D596.

Rabus, R., Hansen T.A., Widdel, F. (2006). *Dissimilatory sulfate- and sulfur-reducing prokaryotes in The Prokaryotes*. New York: Springer, 659–768.

Raff, E.C. (2014). Microbial ecology and biofilms in the taphonomy of soft tissues. *Palaios* **29**, 560–569.

Raff, R.A., Andrews, M.E., Pearson, R.L., Turner, F.R., Saur, S.T., Thomas, D.C., Eagan, J.L. & Raff, E.C. (2014). Microbial ecology and biofilms in the taphonomy of soft tissues. *PALAIOS* **29**, 560-569.

Raff, E.C., Andrews, M.E., Turner, F.R., Toh, E., Nelson, D.E. & Raff, R.A. (2013). Contingent interactions among biofilm-forming bacteria determine preservation or decay in the first steps toward fossilization of marine embryos. *Evolution and Development* **15**, 243–256.

Raff, E.C., Schollaert, K.L., Nelson, D.E., Donoghue, P.C.J., Thomas, C.W., Turner, F.R., Stein, B.D., Dong, X., Bengtson, S., Huldtgren, T., Stampanoni, M., Chongyu, Y., & Raff, R.A. (2008). Embryo fossilization is a biological process mediated by microbial biofilms. *Proceedings of the National Academy of Sciences of the United States of America* **105**, 19360–19365.

Raff, E.C., Villinski, J.T., Turner, F.R., Donoghue, P.C.J., & Raff, R.A. (2006). Experimental taphonomy shows the feasibility of fossil embryos. *Proceedings of the National Academy of Sciences of the United States of America* **103**, 5846–5851.

Raman, R. & Mohamad, S.E. (2012). Astaxanthin production by freshwater microalgae *Chlorella sorokiniana* and marine microalgae *Tetraselmis* sp. *Pakistan Journal of Biological Sciences* **15**, 1182-1186.

Rampelotto, P.H. (2013). Extremophiles and Extreme Environments. *Life* **3**, 482-485.

Recio, J.M. & Léon, V. (1976). Hemolymph iron in Crustacea decapoda during the intermolt cycle. *Revista Espanola de Fisiologia* **32**, 307-311.

Reisdorf, A.G. & Wuttke, M. (2012). Re-evaluating moodie´s opisthotonic-posture hypothesis in fossil vertebrates part I: Reptiles – the taphonomy of the bipedal dinosaurs *Compsognathus longipes* and *Juravenator starki* from the Solnhofen Archipelago (Jurassic, Germany). *Palaeobiodiversity and Palaeoenvironment* **92**, 119-168.

Reitner, J., Paul, J., Arp, G. & Hause-Reitner, D. (1996). Lake Thetis Domal Microbialites – A complex framework of calcified biofilms and organomicrites (Cervantes, Western Australia). In *Global and Regional Controls on Biogenic Sedimentation. I. Reef Evolution* (eds. J. Reitner, F. Neuweiler & F. Gunkel) pp. 85-89. Göttinger Arbeiten zur Geologie und Paläontologie, Göttingen.

Roer, R. & Dillaman, R. (1984). The structure and calcification of the crustacean cuticle. *American Zoologist* **24**, 893-909.

Roger, J. (1946). Invertébrés des couches à poissons du Crétacé supérieur du Liban. *Mémoires de la Société géologique de France (Nouvelle série)* **51**: 1–92.

Ruparell, A., Inui, T., Staunton, R., Wallis, C., Deusch, O. & Holcombe, L.J. (2020). The canine oral microbiome: Variation in bacterial populations across different niches. *BMC Microbiology* **20**.

Sagemann, J., Bale, S.J., Briggs, D.E.G. & Parkes, R.J. (1999). Controls on the formation of authigenic minerals in association with decaying organic matter: An experimental approach. *Geochimica et Cosmochimica Acta* **63**, 1083-1095.

Saito, S. & Tasumi, M. (1983). Normal-coordinate analysis of β-carotene isomers and assignments of the Raman and infrared bands. *Journal of Raman Spectroscopy* **14**, 310-321.

Sansom, R., Gabbott, S.E. & Purnell, M.A. (2010). Non-random decay of chordate characters causes bias in fossil interpretation. *Nature* **463**, 797-800.

Schiffbauer, J.D., Wallace, A.F., Broce, J. & Xiao, S. (2014). Exceptional fossil conservation through phosphatization. *The Paleontological Society Papers* **20**, 59–82.

Schneider, D., Arp, G., Reimer, A., Reitner, J. & Daniel, R. (2013). Phylogenetic analysis of a microbialite-forming microbial mat from a hypersaline lake of the Kiritimati Atoll, Central Pacific. *PLoS ONE* **8**.

Schoenen, D. (2019). *Verwesung und Verwesungsstörungen-Entstehung von Eis- und Trockenmumien, Fettwachs-, Faul- und Moorleichen sowie fossilen Geweresten und lithifizierten Gewebeabdrucken.* (ed. D. Schoenen), Shaker Verlag GmbH, Düren (Germany)

Schoenen, D. & Schoenen, H. (2013). Adipocere formation – The result of insufficient microbial degradation. *Forensic Science International* **226**, 301.e1-301.e6.

Schwermann, A.H., Wuttke, M., Schultz, J.A. (2012). Virtopsy of the controlled decomposition of a dormouse *Eliomys quercinus* as a tool to analyse the taphonomy of *Heterohyus nanus* from Messel (Eocene, Germany). *Palaeobiodiversity and Palaeoenvironments* **92**, 29-43.

Shechter, A., Berman, A., Singer, A., Freiman, A., Grinstein, M., Erez, J., Aflalo, E.D. & Sagi, A. (2008). Reciprocal changes in calcification of the gastrolith and cuticle during the molt cycle of the red claw crayfish *Cherax quadricarinatus*. *Biological Bulletin* **214**, 122-134.

Slobodkin, A. (2014). The Family *Peptostreptococcaceae*. In *The Prokaryotes – Firmicutes and Tenericutes* (eds. E. Rosenberg, E.F. DeLong, S. Lory, E. Stackebrandt, F. Thompson) pp. 291-302. Springer Berlin, Heidelberg.

Sourie, R. & Chaisemartin, C. (1961). Les variations de la teneur en calcium de l´hémolymphe chez *Astacus pallipes* Lereboullet. *Vie Milieu* **12**, 605-613.

Sousa, D. Z., Balk M., Alves M. M., Schink B., McInerney M. J., Smidt H., et al. (2010). Degradation of long-chain fatty acids by sulfate-reducing and methanogenic communities. In *Handbook of Hydrocarbon and Lipid Microbiology* (eds. K.N. Timmis, J.R. Meer van der, T.J. McGenity, V. Lorenzo de) Springer Verlag, Berlin.

Sousa, D.Z., Alves, J.I., Alves, M.M., Smidt, H. & Stams, A.J.M. (2009). Effect of sulfate on methanogenic communities that degrade unsaturated and saturated long-chain fatty acids (LCFA). *Environmental Microbiology* **11**, 68-80.

Stolz, J.F. (2000). Structure of Microbial Mats and Biofilms. In *Microbial Sediments*. (eds. E.R. Riding & S.M. Awramik) pp. 1–8. Springer, Berlin, Heidelberg.

Subramanian, B., Tchoukanova, N., Djaoued, Y., Pelletier, C., Ferron, M. & Robichaud, J. (2014). Investigantionns on the geometrical isomers of astaxanthin: Raman spectroscopy of conjugated polyene chain with electronic and mechanical confinement. *Journal of Raman Spectroscopy* **45**, 299-304.

Surdam, R.C. & Stanley, K.O. (1979). Lacustrine sedimentation during the culminating phase of Eocene Lake Gosiute, Wyoming (Green River Formation). *Geological Society of America Bulletin* **90**, 93-110.

Takatori, T., Ishiguro, N., Tarao, H. & Matsumiya, H. (1986). Microbial production of hydroxy and oxo fatty acids by several microorganisms as a model of adipocere formation. *Forensic Science International* **32**, 5-11.

Tazi, L., Breakwell, D.P., Harker, A.R. & Crandall, K.A. (2014). Life in extreme environments: Microbial diversity in Great Salt Lake, Utah. *Extremophiles* **18**, 525-535.

Tomita, K. (1984). On the production of hydroxy fatty acids and fatty acid oligomers in the course of adipocere formation. *Japanese Journal of Legal Medicine* **38**, 257-272.

Travis, D.F. (1955a). The molting cycle of the spiny lobster, *Panulirus argus* Latreille II. Pre-ecdysial histological and histochemical changes in the hepatopancreas and integumental tissues. *Biological Bulletin* **108**, 88-112.

Travis, D.F. (1960). The deposition of skeletal structures in the crustacea. I. The histology of the gastrolith skeletal tissue complex and the gastrolith in the crayfish, *Orconectes* (*Cambarus*) *virilis* Hagen -Decapoda-. *Biological Bulletin* **118**, 137-149.

Travis, D.F. (1963). Structural features of mineralization from tissue to macromolecular levels of organization in the decapod crustacea. *Annals of the New York Academy of Science* **109**, 177-245.

Travis, D.F. (1965). The deposition of skeletal structures in the crustacea. V. The histomorphological and histochemical changes associated with the development and calcification of the branchial exoskeleton in the crayfish, *Orconectes virilis* Hagen. *Acta Histochemical* **20**, 193-222.

Ueland, M., Breton, H.A. & Forbes, S.L. (2014). Bacterial populations associated with early-stage adipocere formation in lacustrine waters. *International Journal of Legal Medicine* **128**, 379-387.

Ueno, M. & Mizuhira, V. (1983). Calcium-transport mechanism in crayfish gastrolith epithelium correlated with the molting cycle. I. The demonstration of calcium-accumulating sites. *Acta Histochemica et Cytochemica* **16**, 596-605.

Ushakumari, U.N. & Ramanuja, R. (2013). Isolation of astaxanthin from marine yeast and study of its pharmacological activity. *International Current Pharmaceutical Journal* **2**, 67-69.

Vannier, J., Liu, J., Lerosey-Aubril, R., Vinther, J. & Daley, A.C. (2014). Sophisticated digestive systems in early arthropods. *Nature Communications* **5**, 3641.

Vass, A.A. (2001). Beyond the grave – understanding human decomposition. *Microbiology Today* **28**, 190–193.

Veen van, W.L., Mulder, E.G. & Deinema, M.H. (1978). The Sphaerotilus-Leptothrix group of bacteria. *Microbiology Reviews* **42**, 329-356.

Waldenstedt, L., Inborr, J. Hansson, I. & Elwinger, K. (2003). Effects of astaxanthin-rich algal meal (*Haematococcus pluvialis*) on growth performance, caecal campylobacter and clostridial counts and tissue astaxanthin concentration of broiler chickens. *Animal Feed Science and Technology* **108**, 119-132.

Wang, X., Willén, R. & Wadström, T. (2000). Astaxanthin-rich algal meal and vitamin C inhibit *Helicobacter pylori* infection in BALB/cA mice. *Antimicrobial Agents and Chemotherapy* **44**, 2452-2457.

Ward, T., J. Larson, J. Meulemans, B. Hillmann, J. Lynch, D. Sidiropoulos, J. R. Spear, Caporaso, G., Blekhman, R., Knight, R., Fink, R. & Knights, D. (2017). BugBase predicts organism-level microbiome phenotypes. *BioRxiv* 133462

Warthmann, R., Lith van, Y., Vasconcelos, C., McKenzie, J.A. & Karpoff, A.M. (2000). Bacterially induced dolomite precipitation in anoxic culture experiments. *Geology* **28**, 1091-1094.

Warthmann, R., Vasconcelos, C., Sass, H., & McKenzie, J. A. (2005). *Desulfovibrio brasiliensis* sp. nov., a moderate halophilic sulfate-reducing bacterium from Lagoa Vermelha (Brazil) mediating dolomite formation. *Extremophiles* **9**, 255–261.

Waugh, D.A., Feldmann. R.M., Burrell, J.L., Hull, A.L., Hein, K. & Schweitzer, C.E. (2009). Ontogenetic variations in cuticle morphology in the blue crab *Callinectes sapidus*, Rathbun, 1896. *Journal of Crustacean Biology* **29**, 141-156.

Wetherill, C. (1856). Ueber Leichenwachs (Adipocere). *Journal für Praktische Chemie* **68**, 26-35.

Wilby, P.R. & Briggs, D.E.G. (1997). Taxonomic trends in the resolution of detail preserved in fossil phosphatized soft tissues. *GEOBIOS* **20**, 493-502.

Wilby, P.R., Briggs, D.E.G., Bernier, P. & Gaillard, C. (1996). Role of microbial mats in the fossilization of soft tissues. *Geology* **24**, 787-790.

Wilby, P.R., Briggs, D.E.G. & Riou, B. (1996). Mineralization of soft-bodied invertebrates in a Jurassic metalliferous deposit. *Geology* **24**, 847–850.

Wilby, P.R. & Whyte, M.A. (1995). Phosphatized soft tissues in bivalves from the Portland Roach of Dorset (Upper Jurassic). *Geological Magazine* **132**, 117-120.

Wilhelm, H. (1952). *Warum kommen Ertrunkene in tiefen Gewässern nicht mehr an die Oberfläche?* Dissertation, Universität Heidelberg.

Yang, J., Ortega-Hernández, J., Butterfield, N.J., Liu, Y., Boyan, G.S., Hou, J., Lan, T. & Zhang, X. (2016). Fuxianhuiid ventral nerve cord and early nervous system evolution in Panarthropoda. *Proceedings of the National Academy of Sciences* **113**, 2988–2993.

Yuan, J.-P., Peng, J., Yin, K. & Wang, J.-H. (2011). Potential health-promoting effects of astaxanthin: A high-value carotenoid mostly from microalgae. *Molecular Nutrition and Food Research* **55**, 150-165.

You, X., Sun, S., Zhu, J., Li, Q., Hu, W. & Dong, H. (2013). Microbially mediated dolomite in Cambrian stromatolites from the Tarim Basin, north-west China: Implications for the role of organic substrate on dolomite precipitation. *Terra Nova* **25**, 387-395.

Zhang, L., Cao, W., Gao, Y., Yang, R., Zhang, X., Xu, J. & Tang, Q. (2020). Astaxanthin (ATX) enhances the intestinal mucosal functions in immunodeficient mice. *Food and Function* **11**, 3371-3381.

Zhang, M., Sun, Y., Chen, L., Cai, C., Qiao, F., Du, Z. & Li, E. (2016). Symbiotic bacteria in gills and guts of chinese mitten crab (*Eriocheir sinensis*) differ from the free-living bacteria in water. *Plosone* **11**, e0148135.

Zhang, L., Zhang, C., Liu, J. & Yang, N. (2020). A strategy for stimulating astaxanthin and lipid production in *Haematococcus pluvialis* by exogenous glycerol application under low light. *Algal Research* **46**, 101779.

Zillner, E. (1885). Zur Kenntnis der Leichenwachsbildung. *Vierteljahrsschrift für gerichtliche Medizin* **42**, 1-31.

APPENDIX

Chapter 3: Additional Information (AI)

Further investigations of calcite clusters found inside the decomposing crayfish revealed two mineralized muscle remains recognized inside individual C9$_{dist.}$, that decomposed in distilled water. μ-CT images revealed that parts of the opener- and closer muscles of the right chela seems to be mineralized (**Figure AI 1**). This assumption was confirmed by CRS analyses, which clearly revealed, that the muscle remains consist of well-ordered calcite (**Figure AI 2**). Investigations by SEM clearly show some kind of a biofilm on mineralized muscle tissue of the closer muscle related to a calcite conglomerate (**Figure AI 3.5**) and mineralized muscle remains of the opener muscle of the right chela (**Figure AI 3.2**). In addition, the dissolving of gastroliths can lead to simultaneously precipitation of calcite and results in a calcified pseudomorph of gastroliths (**Figure AI 4.3**).
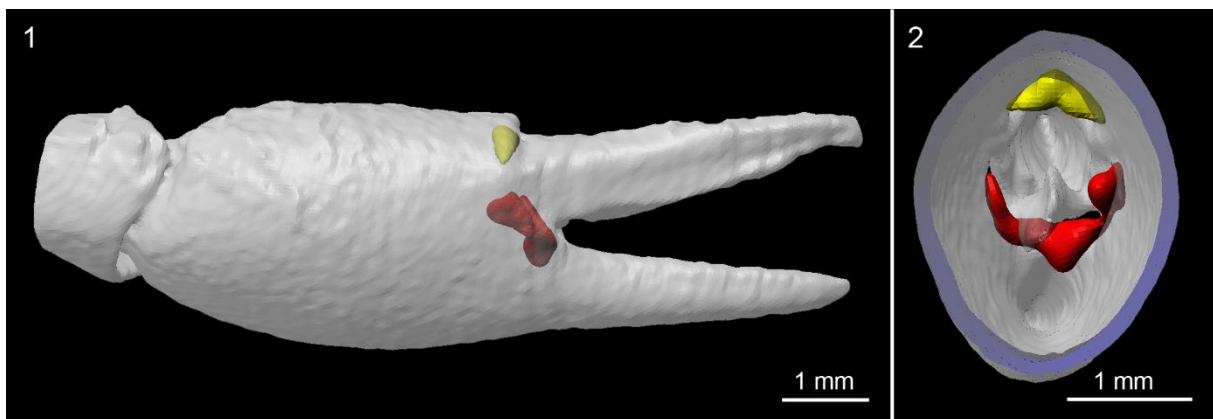
FIGURE AI 1. AI 1.1 3D-model of the right cheliped of sample C9$_{dist.}$ with mineralized parts of opener muscles (yellow) and the closer muscles (red). **AI 1.2** Cross section of the same cheliped as in 1.3 with mineralized muscles.

FIGURE AI 2. Representative Raman spectra of observed muscle remains compared to Raman reference spectra of crystalline apatite and calcite, taken from the RRUFF Raman data base ([#]R060070, [*]R040170 Laetsch & Downs, 2006). Raman spectra of the mineralized muscle exhibit main Raman bands typically for crystallized calcite.
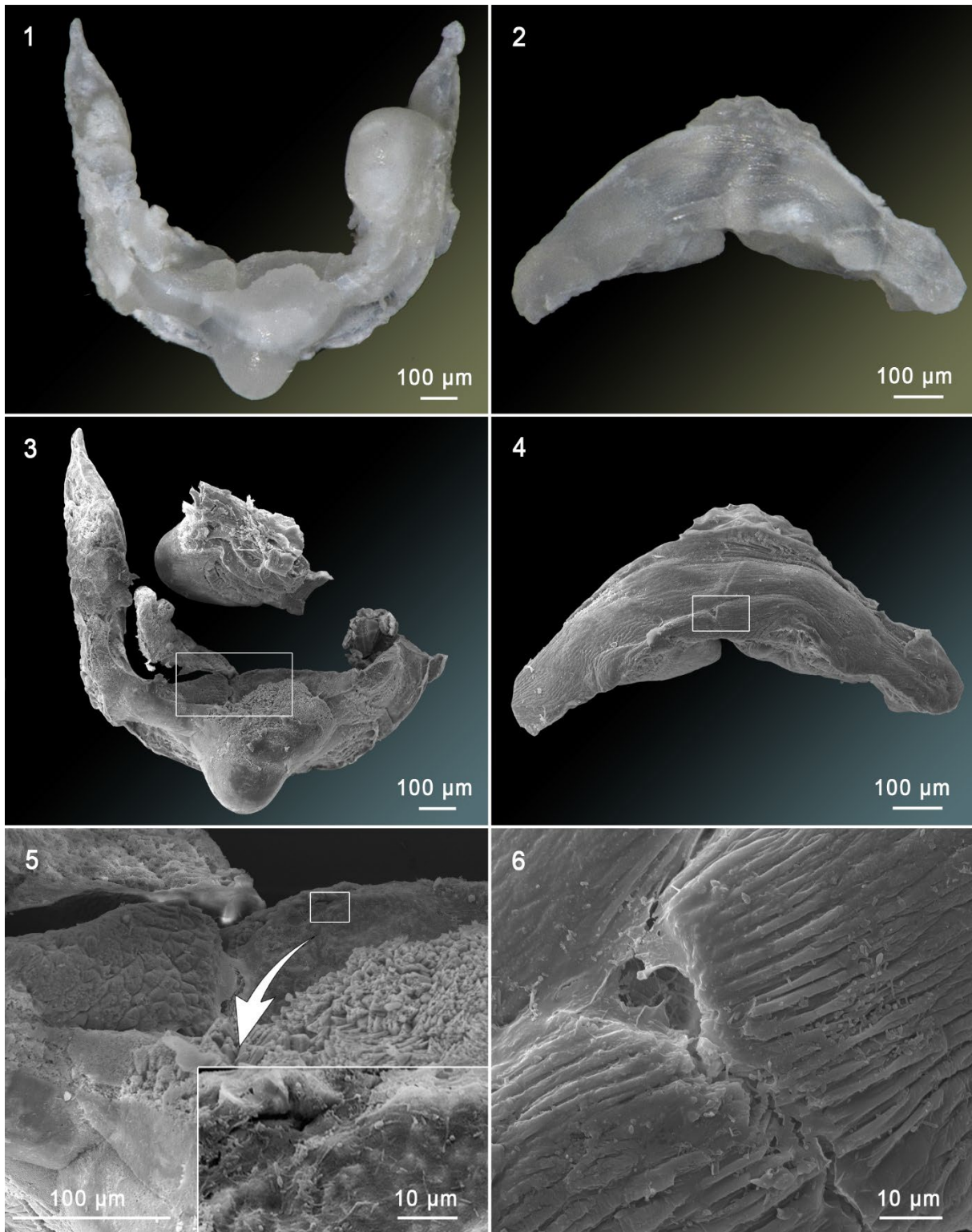
FIGURE AI 3. Photos and SEM images of mineralized structures discovered from the right cheliped of *C. diminutus* C9$_{dist.}$ **AI 3.1** A photo of a horseshoe shaped mineralized structure. **AI 3.2** A photo of a partly mineralized muscle. **AI 3.3** SEM image of the horseshoe shaped mineralized structure, shown in 3.1, broken on the left side, with mineralized muscles (box) **AI 3.4** SEM image of a partly mineralized muscle, shown in 3.2. **AI 3.5** Mineralized muscle with some kind of a biofilm (box). **AI 3.6** Enlarged mineralized muscle showing the muscle fibres.
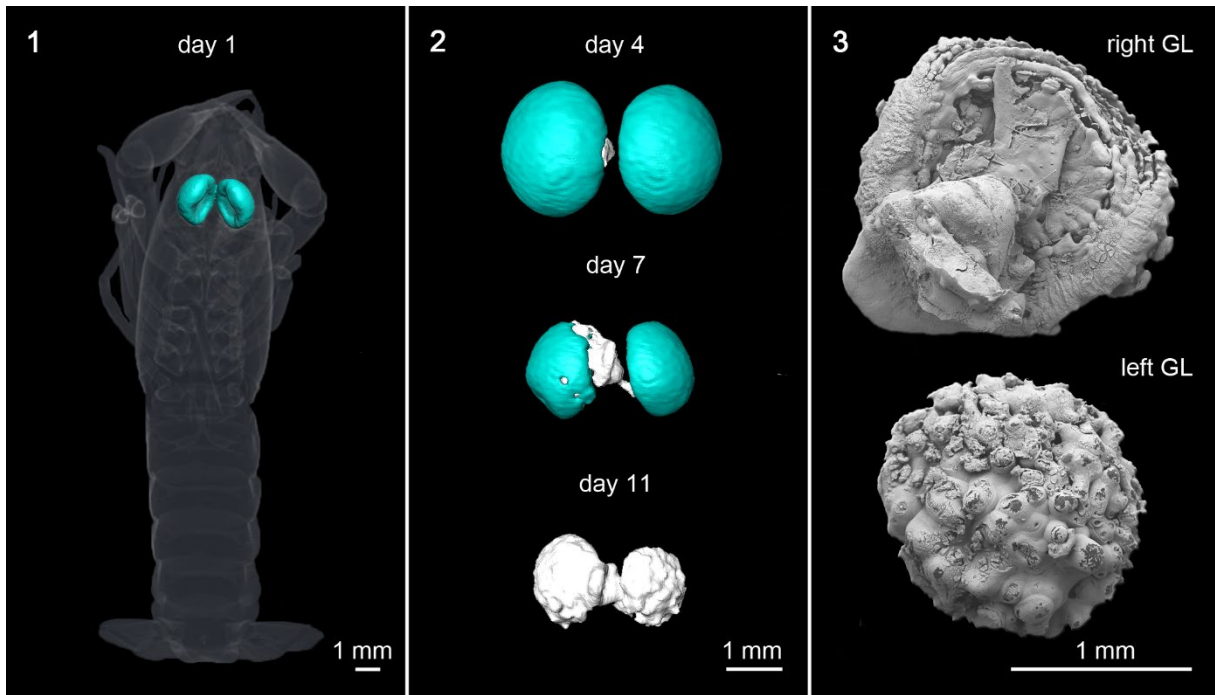
FIGURE AI 4. Images of dissolving gastroliths during the decomposition of *C. diminutus* (C9tank) in freshwater. **AI 4.1** Translucent 3D-model of a crayfish in dorsal view with reconstructed gastroliths inside the crayfish on day 1. **AI 4.2** Frontal view of 3D-models showing the dissolving of ACC of the gastroliths (blue) and simultaneously precipitation of calcite (white) during the decomposition on day 4, 7 and 11. **AI 4.3** SEM-images of calcified pseudomorphs of gastroliths. Right gastrolith in ventral view, left gastrolith in dorsal view. **GL**, gastrolith.

Chapter 3: Additional Study (AS)

Measurement of ^{43}Ca in solution during the decomposition of *Cambarellus diminutus* in tank- and distilled-water at 30°C for a duration of 11 days.

AS.1 Introduction

The results of Chapter 3 show that crayfish which were in the intermoult phase and decomposed in tank water showed a higher calcite precipitation than crayfish that decomposed in distilled water. It was suggested that the difference in the amount of precipitated calcite was a result of diffusion and Brownian molecular motion during the decay in distilled water. In other words, more Ca^{2+} were released into the surrounding medium in distilled water than in tank water, because of missing Ca^{2+} in distilled water and the tendency of particles to distribute themselves evenly in a solution. On the other hand, tank water was more saturated in Ca^{2+} than distilled water, and more Ca^{2+} can remain inside the body. Therefore, a new study was conducted in which the release of Ca^{2+} into the surrounded medium was measured.

AS.2 Material and methods

Six individuals of the crayfish *C. diminutus* (raised in our lab; see chapter 3) with partly filled guts, were sacrificed by placing them in an atmosphere of CO_2. Specimens were not dried before weighing on a microscale. Length were measured from the anterior tip of the cephalothorax to the end of the abdomen, without the telson (**Table AS 1**).

TABLE AS 1. wet weight (ww) [g]; body size (bs) [cm]

Sample	ww	bs	Sample	ww	bs
C11$_{tank}$	0.47	2.40	C11$_{dist.}$	0.41	2.40
C12$_{tank}$	0.26	1.90	C12$_{dist.}$	0.23	1.90
C13$_{tank}$	0.25	1.90	C13$_{dist.}$	0.25	1.80

For the experiment 6 dead specimens (C11$_{tank}$ to C13$_{tank}$ and C11$_{dist}$ to C13$_{dist}$) were each placed in one sterile Falcon tube (50 mL). Three tubes were then filled with 50 mL of tank water and 3 tubes were filled with 50 mL of distilled water. Afterwards tubes were closed and stored in

an incubator (Memmert GmbH & Co. KG, Schwabach, Germany) at a constant temperature of 30°C for 11 days.

μ-CT

The individuals were scanned at the beginning of the experiment and after 11 days using the same μ-CT scanner as in chapter 3. Each data set has a resolution of 30 μm; the scans were performed at 120 kV and 120 μA. Three frames per projection were acquired by a timing of 500 ms for a total of 600 projections. The CT data were processed using the software VG Studio Max 3.2 (Volume Graphics, Heidelberg, Germany) and Avizo 8.1 (Thermo Fisher Scientific, Schwerte, Germany) to reconstruct and visualize the precipitated crystal clusters inside the specimens, and the gastroliths located inside the stomach. In addition, Avizo 8.1 was used for volume measurements of polygonal 3D-surface models.

ICPMS

At the beginning of the experiments 4 mL of 2 samples of tank water and 2 samples of distilled water were taken and filled in a 5 mL tube, which had been previously cleaned twice by deionized water [MilliQ] (18.2 MΩ*cm at 25°C) and dried for two days. For water analyses of the samples $C11_{tank}$ to $C13_{tank}$ and $C11_{dist}$ to $C13_{dist}$ 4 mL of each test tube were taken for the first four days and on day 7 and 11. Water samples out of the six test tubes were each filled in one 5 mL tube. Afterwards, water samples in 5 mL tubes were acidified by 0.2 mL of concentrated nitric acid (HNO_3 [65 %]) and stored at 4°C. On each day, after a water sample was taken, the tubes of $C11_{tank}$ to $C13_{tank}$ were refilled with 4 mL of tank water and tubes of $C11_{dist}$ to $C13_{dist}$ were refilled with 4 mL of distilled water. The following process is explained in chapter 3.

ICPMS measurements revealed that at the beginning of the experiments an average of 45.37 μg/mL calcium was contained in tank water (**Table AS 2**). The amount of calcium in distilled water was below the detection limit (**Table AS 3**).

TABLE AS 2. Concentration of calcium (^{43}Ca) in tank water. **STD**, standard; **M**, measurement; **MV**, mean value; **d**, day; **CP**, check plot

Sample	M 1	M 2	MV	STD
CP_{tank}	45.14	45.59	**45.37**	0.32
$C11_{tank}$ d1	45.77	45.37	**45.57**	0.28
$C12_{tank}$ d1	45.52	45.91	**45.72**	0.28
$C13_{tank}$ d1	45.79	45.65	**45.72**	0.10
$C11_{tank}$ d2	49.01	49.30	**49.16**	0.21
$C12_{tank}$ d2	49.46	49.28	**49.37**	0.13
$C13_{tank}$ d2	47.91	47.58	**47.75**	0.23
$C11_{tank}$ d3	52.25	52.62	**52.44**	0.26
$C12_{tank}$ d3	55.71	55.10	**55.41**	0.43
$C13_{tank}$ d3	57.57	57.10	**57.34**	0.33
$C11_{tank}$ d4	96.97	97.96	**97.47**	0.70
$C12_{tank}$ d4	74.61	75.08	**74.85**	0.33
$C13_{tank}$ d4	82.48	82.42	**82.45**	0.04
$C11_{tank}$ d7	119.77	119.66	**119.72**	0.07
$C12_{tank}$ d7	82.54	83.79	**83.17**	0.88
$C13_{tank}$ d7	102.48	102.19	**102.34**	0.21
$C11_{tank}$ d11	146.36	148.4	**147.38**	1.44
$C12_{tank}$ d11	85.54	85.93	**85.74**	0.28
$C13_{tank}$ d11	100.85	101.23	**101.04**	0.27
CP_{tank} End	45.95	46.07	**46.01**	0.08

TABLE AS 3. Concentration of calcium (^{43}Ca) in distilled water. **STD**, standard; **M**, measurement; **MV**, mean value; **d**, day; **CP**, checkplot; **DL**, detection limit

Sample	M 1	M 2	MV	STD
CP_{dist}	< DL	< DL	**-**	-
$C11_{dist}$ d1	< DL	< DL	**-**	-
$C12_{dist}$ d1	< DL	< DL	**-**	-
$C13_{dist}$ d1	< DL	< DL	**-**	-
$C11_{dist}$ d2	2.39	2.36	**2.38**	0.02
$C12_{dist}$ d2	2.02	2.00	**2.01**	0.01
$C13_{dist}$ d2	2.23	2.22	**2.23**	0.01
$C11_{dist}$ d3	4.34	4.32	**4.33**	0.01
$C12_{dist}$ d3	4.99	4.88	**4.94**	0.08
$C13_{dist}$ d3	6.30	6.41	**6.36**	0.08
$C11_{dist}$ d4	23.29	23.33	**23.31**	0.03
$C12_{dist}$ d4	20.62	20.81	**20.72**	0.13
$C13_{dist}$ d4	32.55	32.16	**32.36**	0.28
$C11_{dist}$ d7	40.15	39.67	**39.91**	0.34
$C12_{dist}$ d7	46.47	46.22	**46.35**	0.18
$C13_{dist}$ d7	50.62	50.33	**50.48**	0.21
$C11_{dist}$ d11	53.51	53.22	**53.37**	0.21
$C12_{dist}$ d11	60.34	59.49	**59.92**	0.60
$C13_{dist}$ d11	50.26	50.12	**50.19**	0.10
CP_{dist} End	< DL	< DL	**-**	-

SEM

On day 11 the altered crayfish samples were removed from the test tubes. Crystal clusters were dissected and coated by a thin layer of gold. Afterwards, samples were scanned with an SEM unit (TESCAN VEGA).

CRS

Crystal clusters were analyzed like in chapter 3

AS.3 Results

µ-CT

µ-CT images revealed that specimens $C11_{tank}$, $C12_{tank}$ and $C11_{dist}$ contained one pair of gastroliths inside their stomach (**Figure AS 1.1**). Volume measurements of polygonal 3D-surface models of gastroliths in tank and in distilled water showed a volume reduction of gastroliths from the beginning to the end of the experiment (**Table AS 4**). In addition, µ-CT images show a precipitation of crystal clusters inside the specimens like in chapter 3.1 (**Figure AS 1.2**; **Table AS 4**).
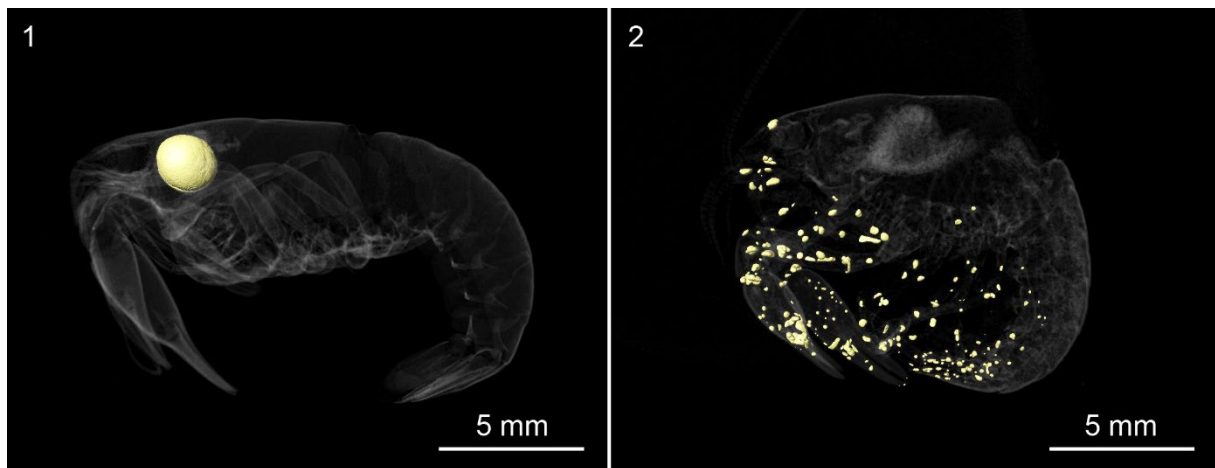
FIGURE AS 1. Translucent 3D-models of *C. diminutus*. **AS 1.1** Translucent 3D-model of sample $C12_{tank}$ on day 1 with 3D-model of one pair of gastroliths. **AS 1.2** Translucent 3D-model of sample $C12_{dist}$ on day 11 with 3D-models of crystal clusters inside.

TABLE AS 4. Total Volume of Gastroliths, TVG [mm^3]; Total Volume of Calcite, TVC [mm^3]

Sample	TVG	TVG$_{End}$	TVC	Sample	TVG	TVG$_{End}$	TVC
C11$_{tank}$	0.288	-	0.197	C11$_{dist.}$	1.073	0.101	0.179
C12$_{tank}$	3.871	1.612	0.003	C12$_{dist.}$	-	-	1.017
C13$_{tank}$	-	-	0.727	C13$_{dist.}$	-	-	0.853

ICPMS

ICPMS measurements of C11$_{tank}$ to C13$_{tank}$ and C11$_{dist}$ to C13$_{dist}$ revealed that in all experimental solutions the calcium content increased with progressive decay (**Table AS 2 and AS 3** and **Figure AS 2**).
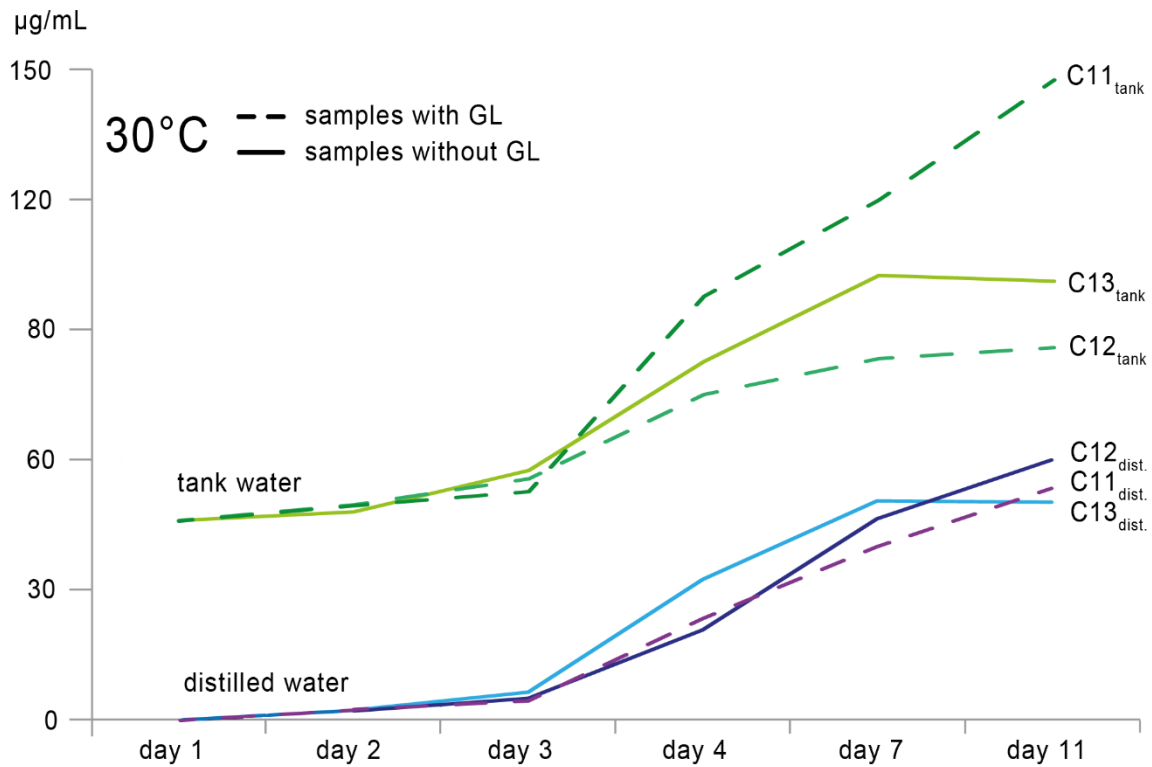
FIGURE AS 2. Comparison of the amount of dissolved calcium ions in tank water samples and distilled water samples for a duration of 11 days. **tank**, tank water; **dist**, distilled water; **C**, crayfish.

SEM

SEM-images show several precipitated crystals varying in sizes from ~200 µm to ~1.100 µm at the end of the experiment (**Figure AS 3**). Most of these structures are spherical or bispherical like in Mähler et al. (2020). In addition, mineralized structures were found inside the pereiopods (**Figure AS 3.1-2**) and the intestine (**Figure AS 3.3**). All crystal clusters are white like in the experiments of Mähler et al. (2020).
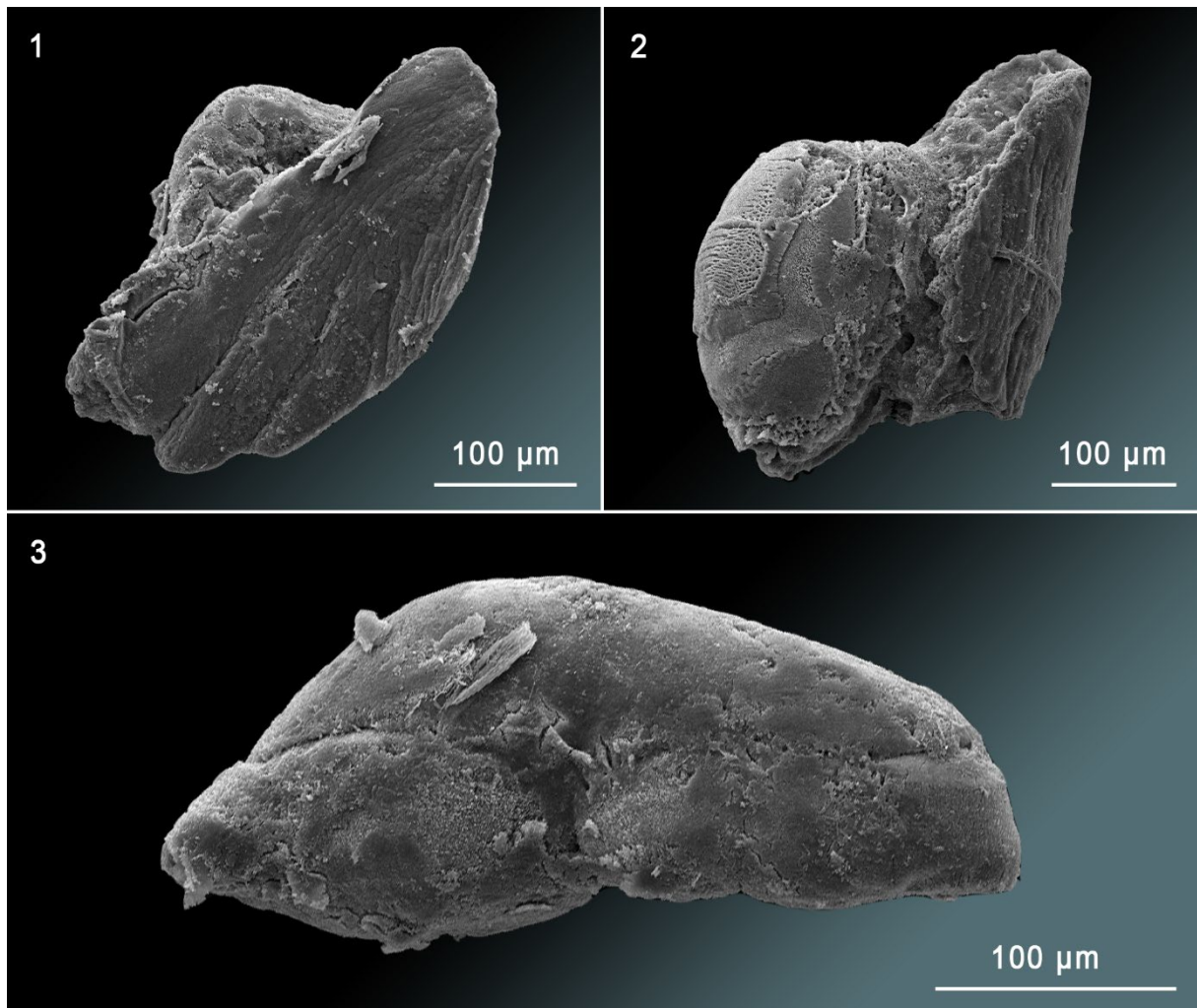
FIGURE AS 3. SEM images of mineralized structures discovered from the pereiopods and the gut of *C. diminutus* C13$_{dist.}$ **AS 3.1** Mineralized structure found inside a pereiopod. **AS 3.2** Mineralized structure found inside a pereiopod. **AS 3.3** Mineralized ingredients of the intestine.

CRS

Raman analyses clearly revealed that the crystal clusters consist of well-ordered calcite, which can be identified by a sharp band near 1085 cm^{-1}, as well as the presence of lattice vibrations near 154 and 281 cm^{-1}, with the latter being absent in amorphous calcium carbonate (ACC) (**Figure AS 4**).
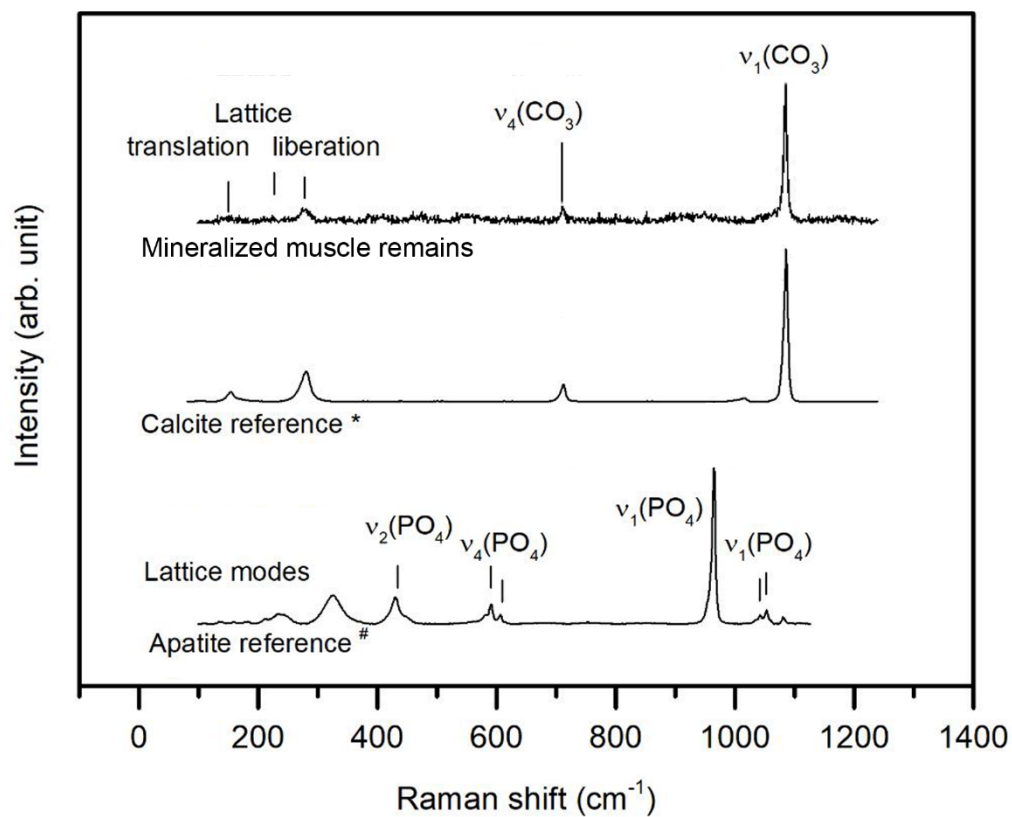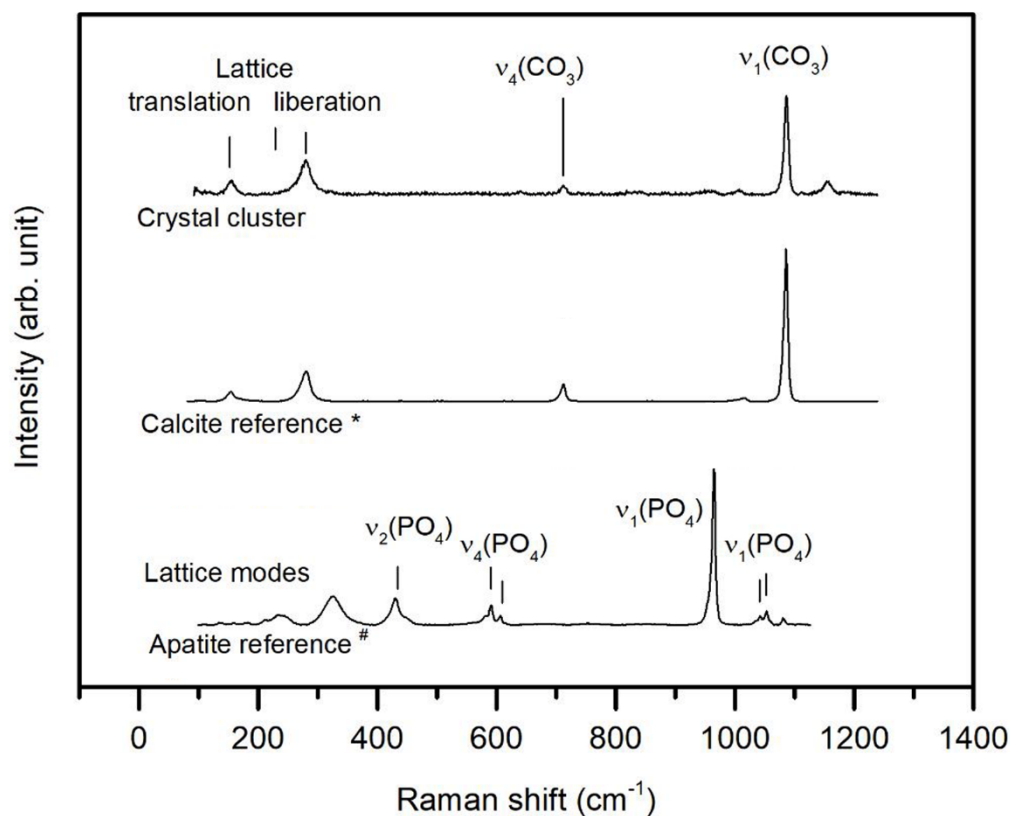

FIGURE AS 4. Representative Raman spectra of observed crystal clusters compared to Raman reference spectra of crystalline calcite and apatite, taken from the RRUFF Raman data base (*R040170, #R060070, Laetsch & Downs, 2006). Raman spectra of the crystal cluster exhibit all main Raman bands typically observed in well crystallized calcite, including the lattice modes, which are absent in amorphous calcium carbonate (Wang et al. 2011).

AS.4 Discussion

The results of this study show, that in all samples calcium ions were released into the surrounded medium with progressive decay (**Table AS 2** and **AS 3** and **Figure AS 2**). If the values of the initial measurements on day 1 in tank water are subtracted from the subsequent values of the following days, it shows that the amount of dissolved calcium was approximately the same in all samples, whether the individuals decomposed in distilled water or tank water (except sample $C11_{tank}$ and $C12_{tank}$). For individual $C11_{tank}$ it is assumed that it was in the early premoult phase, because of the small total volume of gastroliths (TVG: 0.288 mm^3) and the high amount of released Ca^{2+} (147.38 µg/mL – 45.557 µg/mL = ***101.81 µg/mL***). In other words, more dissolved calcium ions were released into the surrounded medium than could precipitate in the carcass as calcite. It is assumed, that individual $C12_{tank}$ was in the early postmoult phase at the time of death, because of the large volume of gastroliths (TVG: 3.9 mm^3) and because of the low total volume of calcite (TVC: 0.003 mm^3). Further on, it seems that individual $C12_{tank}$ has lost most of its calcium ions during the moulting process and not enough calcium ions were taken up by nutrition till the moment of death. Therefore, the release of calcium ions into the solution was also low (85.74 µg/mL – 45.72 µg/mL = ***40.02 µg/mL***) than in the other samples.

Combining the data form this study with those of the study by Mähler et al. (2020) revealed that the TVC in individuals which decomposed in tank water was higher than the TVC in individuals which decomposed in distilled water, if the individuals were in the intermoult phase at the time of death (**Figure AS 5**). However, if the individuals are in one of the moulting phases, the stage of the moulting phase was important.

It is assumed that in tank water Ca^{2+} from the surrounded medium diffused inside the crayfish with a simultaneously calcium dissolution out of the carapace into the medium. But this thesis must be validated by further studies.
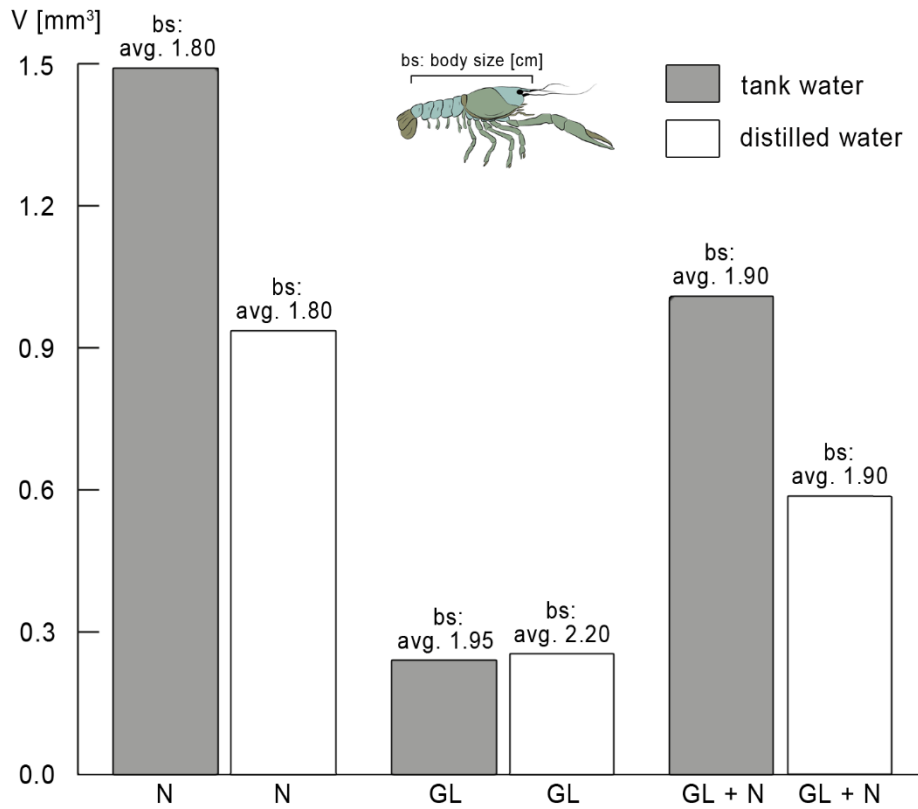
FIGURE AS 5. Mean values of the total volume of calcite (TVC) of individuals which decomposed in tank and distilled water on day 11, from chapter 2 in combination with the individuals of the additional study. **N** mean value of TVC of all individuals without gastroliths (intermoult phase), **GL** mean values of TVC of all individuals with gastroliths (postmoult or premoult phase), **avg.** average.

Chapter 4: Supplement

Supplement 1

Product information

Complete feed for all crustaceans

Ingredients

fish meal, corn starch, wheat flour, spirulina, brewers yeast, wheat germ, gammarus, Ca-caseinate, sea algae, stinging nettle, willow bark, alder cones, fish oil (containing 49% omega fatty acids), mannan oligosaccharides, herbs, alfalfa, parsley, paprika, green-lipped mussel, spinach, carrots, *Haematococcus* algae, garlic.

Analytical constituents

Crude Protein 36.7%, Crude Fat 11.1%, Crude Fiber 4.5%, Moisture 5.2%, Crude Ash 8.6%, Ca 1.9%, P 1.0%.

Additives

Vitamins and provitamins: Vit. A 37,000 IU/kg, Vit. D3 1,800 IU/kg, Vit. E (D, L-α-tocopheryl acetate) 120 mg/kg, Vit. B1 35 mg/kg, Vit. B2 90 mg/kg, stab. Vit. C (L-ascorbyl monophosphate) 550 mg/kg.

SUPPLEMENTARY TABLE S1. Mass-to-charge ratios (m/z) of the analyzed fatty acids. In bold are the m/z values used for identification of the acids

Fatty acid	M_r	$[M–H]^-$
Myristic acid	228.2 Da	**227.2 Da**
Palmitoleic acid	254.2 Da	**253.2 Da**
Palmetic acid	256.2 Da	**255.2 Da**
Linoleic acid	280.2 Da	**279.2 Da**
Oleic acid	282.3 Da	**281.3 Da**
Stearic acid	284.3 Da	**283.3 Da**

Palmitoleate
Exact Mass: 253.22 Da

Palmitate
Exact Mass: 255.23 Da

Linoleate
Exact Mass: 279.23 Da

Stearate
Exact Mass: 283.26 Da

Oleate
Exact Mass: 281.25 Da

Myristate
Exact Mass: 227.20 Da
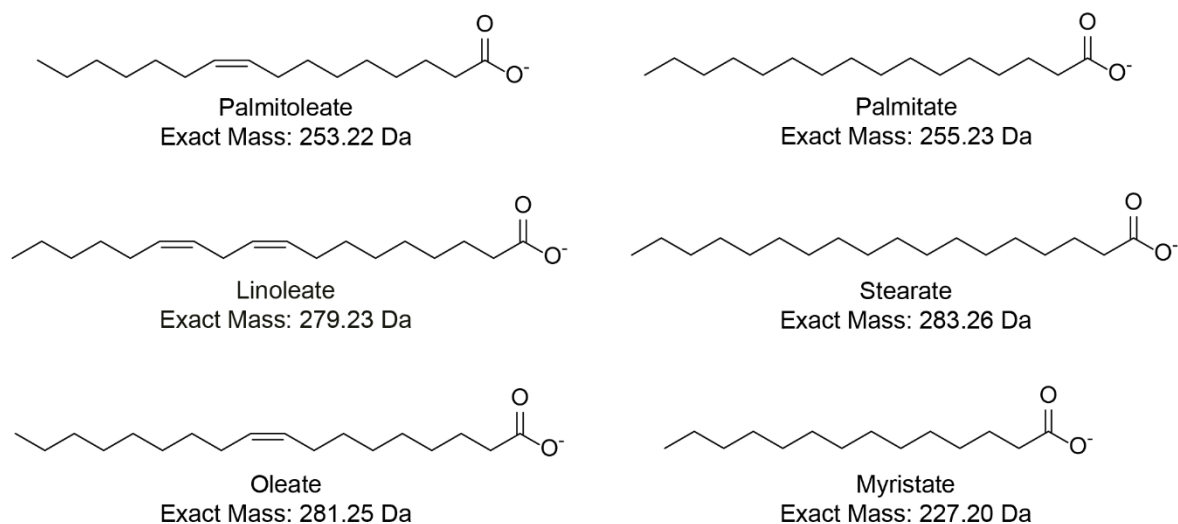
SUPPLEMENTARY FIGURE S1. Structures of the free fatty acids analyzed as deprotonated species [M-H]⁻.
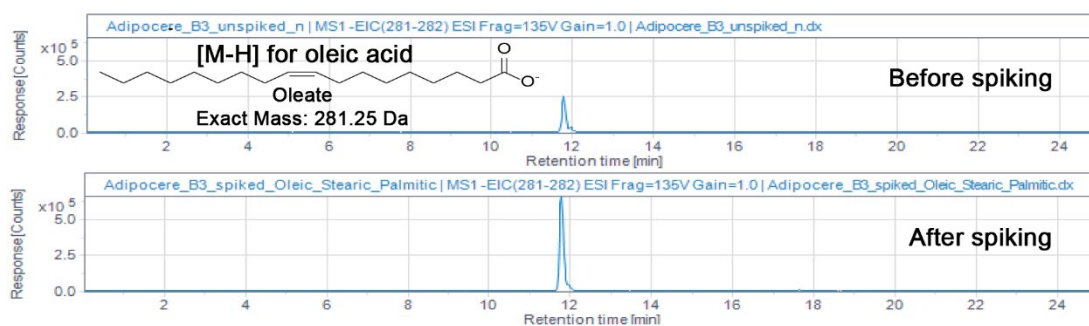
SUPPLEMENTARY FIGURE S2. Extracted ion chromatograms (EIC) showing the deprotonated ion of oleic acid (oleate, 281.3 ±0.7 m/z) in the adipocere extract, and the increase in its peak area following the addition of a known amount of oleic acid, confirming that oleic acid is present in the adipocere extract. Note that this standard addition experiment with oleic acid was performed in a different run and on a different day than the run shown in **Figure 12.1-2**, which explains the slight shift in retention time.

Chapter 5: Supplement

SUPPLEMENTARY TABLE S1.

Size and body weight of specimens. Exp., experiment; ww, wet weigth [g]; bs, body size [cm]

Exp. 1.1			Exp. 2.1			Exp. 3.1			Exp. 4.1		
Sample	ww	bs	Sample	ww	bs	Sample	ww	bs	Sample	ww	bs
E1-2.1	0.47	2.30	E2-2.1	0.19	1.70	E3-7.1	0.47	2.30	E4-7.1	0.33	2.10
E1-2.2	0.41	2.00	E2-2.2	0.28	1.80	E3-7.2	0.31	1.80	E4-7.2	0.21	1.80
E1-3.1	0.28	1.80	E2-3.1	0.25	2.00	E3-14.1	0.19	1.70	E4-14.1	0.32	2.00
E1-3.2	0.53	2.40	E2-3.2	0.28	2.10	E3-14.2	0.34	2.10	E4-14.2	0.23	1.80
E1-4.1	0.32	2.00	E2-4.1	0.17	1.70	E3-21.1	0.52	2.50	E4-21.1	0.30	2.10
E1-4.2	0.38	2.00	E2-4.2	0.18	1.70	E3-21.2	0.32	2.00	E4-21.2	0.23	1.80
E1-7.1	0.64	2.50	E2-7.1	0.21	1.70	E3-49.1	0.21	1.70	E4-49.1	0.31	2.10
E1-7.2	0.23	1.60	E2-7.2	0.25	1.80	E3-49.2	0.35	1.90	E4-49.2	0.36	2.20
E1-14.1	0.34	1.90	E2-14.1	0.13	1.50	E3-77.1	0.29	1.90	E4-77.1	0.24	1.80
E1-14.2	0.20	1.60	E2-14.2	0.13	1.50	E3-77.2	0.31	2.10	E4-77.2	0.24	1.90
E1-21.1	**0.53**	**2.40**	**E2-21.1**	**0.34**	**2.10**	**E3-105.1**	**0.29**	**2.10**	**E4-105.1**	**0.22**	**1.70**
E1-21.2	**0.50**	**2.30**	**E2-21.2**	**0.43**	**2.20**	**E3-105.2**	**0.26**	**2.00**	**E4-105.2**	**0.26**	**1.90**
E1-21.3	**0.28**	**1.80**	**E2-21.3**	**0.38**	**2.30**						

Exp. 5.1			Exp. 6.1			Exp. 7.1			Exp. 8.1		
Sample	ww	bs	Sample	ww	bs	Sample	ww	bs	Sample	ww	bs
E5-2.1	0.14	1.50	E6-2.1	0.28	1.80	E7-7.1	0.14	1.40	E8-7.1	0.19	1.60
E5-2.2	0.16	1.50	E6-2.2	0.20	1.70	E7-7.2	0.15	1.40	E8-7.2	0.21	1.70
E5-3.1	0.17	1.70	E6-3.1	0.24	1.80	E7-14.1	0.18	1.70	E8-14.1	0.21	1.70
E5-3.2	0.22	1.80	E6-3.2	0.30	1.80	E7-14.2	0.14	1.40	E8-14.2	0.20	1.70
E5-4.1	0.21	1.60	E6-4.1	0.20	1.70	E7-21.1	0.16	1.60	E8-21.1	0.23	1.70
E5-4.2	0.24	1.80	E6-4.2	0.20	1.40	E7-21.2	0.08	1.20	E8-21.2	0.25	1.80
E5-7.1	0.16	1.50	E6-7.1	0.24	1.80	E7-49.1	0.12	1.30	E8-49.1	0.22	1.60
E5-7.2	0.13	1.40	E6-7.2	0.21	1.70	E7-49.2	0.11	1.40	E8-49.2	0.23	1.70
E5-14.1	0.10	1.40	E6-14.1	0.24	1.80	E7-77.1	0.10	1.30	E8-77.1	0.29	1.70
E5-14.2	0.12	1.40	E6-14.2	0.22	1.70	E7-77.2	0.17	1.40	E8-77.2	0.19	1.70
E5-21.1	**0.25**	**1.80**	**E6-21.1**	**0.23**	**1.80**	**E7-105.1**	**0.10**	**1.30**	**E8-105.1**	**0.12**	**1.30**
E5-21.2	**0.45**	**2.00**	**E6-21.2**	**0.23**	**1.80**	**E7-105.2**	**0.15**	**1.40**	**E8-105.2**	**0.12**	**1.30**
E5-21.3	**0.31**	**2.00**	**E6-21.3**	**0.23**	**2.00**						

SUPPLEMENTARY TABLE S2.1

Exp. 1 (^{43}Ca) untreated / aerobic / 24°C

Sample	Measurement 1	Measurement 2	Mean value	Variance	STD
E1-CP-1	47.88	47.80	47.84	0.00	0.06
E1-2.1	52.48	52.68	52.58	0.02	0.14
E1-2.2	51.38	51.96	51.67	0.17	0.41
E1-3.1	51.45	51.21	51.33	0.03	0.17
E1-3.2	50.10	50.09	50.10	0.00	0.01
E1-4.1	51.47	51.15	51.31	0.05	0.23
E1-4.2	52.21	52.28	52.25	0.00	0.05
E1-7.1	58.10	56.54	57.32	1.22	1.10
E1-7.2	52.10	51.59	51.85	0.13	0.36
E1-14.1	67.01	67.15	67.08	0.01	0.10
E1-14.2	82.17	82.21	82.19	0.00	0.03
E1-21.1	112.22	110.76	111.49	1.06	1.03
E1-21.2	52.84	53.03	52.94	0.02	0.13
E1-CP-21	51.71	51.28	51.50	0.09	0.30

SUPPLEMENTARY TABLE S2.2

Exp. 2 (^{43}Ca) sterile / aerobic / 24°C

Sample	Measurement 1	Measurement 2	Mean value	Variance	STD
E2-CP-1	45.32	44.62	44.97	0.25	0.49
E2-2.1	42.78	42.65	42.72	0.01	0.09
E2-2.2	43.78	44.09	43.94	0.05	0.22
E2-3.1	78.94	77.97	78.46	0.47	0.69
E2-3.2	154.26	151.74	153.00	3.18	1.78
E2-4.1	70.70	71.17	70.94	0.11	0.33
E2-4.2	77.84	77.06	77.45	0.30	0.55
E2-7.1	188.25	186.56	187.41	1.43	1.20
E2-7.2	189.26	190.60	189.93	0.90	0.95
E2-14.1	135.17	134.01	134.59	0.67	0.82
E2-14.2	128.13	128.36	128.25	0.03	0.16
E2-21.1	233.72	238.02	235.87	9.25	3.04
E2-21.2	145.14	146.12	145.63	0.48	0.69
E2-CP-21	57.19	58.03	57.61	0.35	0.59

SUPPLEMENTARY TABLE S2.3

Exp. 3 (^{43}Ca) untreated / aerobic / 4°C

Sample	Measurement 1	Measurement 2	**Mean value**	Variance	STD
E3-CP-1	48.36	46.56	**47.46**	1.62	1.27
E3-7.1	56.20	55.80	**56.00**	0.08	0.28
E3-7.2	45.56	54.84	**50.20**	43.06	6.56
E3-14.1	46.56	64.64	**55.60**	163.44	12.78
E3-14.2	75.84	75.60	**75.72**	0.03	0.17
E3-21.1	61.76	61.56	**61.66**	0.02	0.14
E3-21.2	60.28	60.76	**60.52**	0.12	0.34
E3-49.1	92.44	91.56	**92.00**	0.39	0.62
E3-49.2	118.96	118.00	**118.48**	0.46	0.68
E3-77.1	154.64	151.96	**153.30**	3.59	1.90
E3-77.2	173.12	171.48	**172.30**	1.34	1.16
E3-105.1	151.04	150.28	**150.66**	0.29	0.54
E3-105.2	153.08	152.40	**152.74**	0.23	0.48
E3-CP-105	79.68	79.12	**79.40**	0.16	0.40

SUPPLEMENTARY TABLE S2.4

Exp. 4 (^{43}Ca) sterile / aerobic / 4°C

Sample	Measurement 1	Measurement 2	**Mean value**	Variance	STD
E4-CP-1	42.92	42.16	**42.54**	0.29	0.54
E4-7.1	48.60	47.44	**48.02**	0.67	0.82
E4-7.2	53.20	54.56	**53.88**	0.92	0.96
E4-14.1	61.04	61.32	**61.18**	0.04	0.20
E4-14.2	57.88	58.20	**58.04**	0.05	0.23
E4-21.1	50.16	48.76	**49.46**	0.98	0.99
E4-21.2	50.44	49.68	**50.06**	0.29	0.54
E4-49.1	94.32	97.00	**95.66**	3.59	1.90
E4-49.2	87.32	87.40	**87.36**	0.00	0.06
E4-77.1	115.68	116.16	**115.92**	0.12	0.34
E4-77.2	118.08	116.12	**117.10**	1.92	1.39
E4-105.1	127.68	125.04	**126.36**	3.48	1.87
E4-105.2	119.32	119.00	**119.16**	0.05	0.23
E4-CP-105	43.32	42.84	**43.08**	0.12	0.34

SUPPLEMENTARY TABLE S2.5

Exp. 5 (^{43}Ca) untreated / anaerobic / 24°C

Sample	Measurement 1	Measurement 2	**Mean value**	Variance	STD
E5-CP-1	48.56	48.88	**48.72**	0.05	0.23
E5-2.1	55.27	55.32	**55.30**	0.00	0.04
E5-2.2	55.19	54.91	**55.05**	0.04	0.20
E5-3.1	54.13	53.4	**53.77**	0.27	0.52
E5-3.2	56.46	56.07	**56.27**	0.08	0.28
E5-4.1	56.92	56.62	**56.77**	0.05	0.21
E5-4.2	56.72	57.36	**57.04**	0.20	0.45
E5-7.1	70.82	69.12	**69.97**	1.44	1.20
E5-7.2	70.92	71.01	**70.97**	0.00	0.06
E5-14.1	73.98	74.43	**74.21**	0.10	0.32
E5-14.2	61.96	62.73	**62.35**	0.30	0.54
E5-21.1	97.24	98.74	**97.99**	1.13	1.06
E5-21.2	94.84	96.75	**95.80**	1.82	1.35
E5-CP-21	97.64	97.67	**97.66**	0.00	0.02

SUPPLEMENTARY TABLE S2.6

Exp. 6 (^{43}Ca) sterile / anaerobic / 24°C

Sample	Measurement 1	Measurement 2	**Mean value**	Variance	STD
E6-CP-1	48.56	48.88	**48.72**	0.05	0.23
E6-2.1	52.96	53.22	**53.09**	0.03	0.18
E6-2.2	53.61	54.01	**53.81**	0.08	0.28
E6-3.1	56.05	56.48	**56.27**	0.09	0.30
E6-3.2	55.81	55.50	**55.66**	0.05	0.22
E6-4.1	59.95	58.79	**59.37**	0.67	0.82
E6-4.2	56.37	55.21	**55.79**	0.67	0.82
E6-7.1	65.77	66.58	**66.18**	0.33	0.57
E6-7.2	64.85	64.93	**64.89**	0.00	0.06
E6-14.1	99.02	97.83	**98.43**	0.71	0.84
E6-14.2	77.94	77.51	**77.73**	0.09	0.30
E6-21.1	93.92	94.08	**94.00**	0.01	0.11
E6-21.2	88.41	89.33	**88.87**	0.42	0.65
E6-CP-21	57.80	58.67	**58.24**	0.38	0.62

SUPPLEMENTARY TABLE S2.7

Exp. 7 (^{43}Ca) untreated / anaerobic / 4°C

Sample	Measurement 1	Measurement 2	**Mean value**	Variance	STD
E7-CP-1	51.74	51.22	**51.48**	0.14	0.37
E7-7.1	42.73	41.88	**42.31**	0.36	0.60
E7-7.2	42.63	43.44	**43.04**	0.33	0.57
E7-14.1	43.59	42.93	**43.26**	0.22	0.47
E7-14.2	43.54	41.28	**42.41**	2.55	1.60
E7-21.1	45.60	46.29	**45.95**	0.24	0.49
E7-21.2	46.09	46.42	**46.26**	0.05	0.23
E7-49.1	64.90	67.38	**66.14**	3.08	1.75
E7-49.2	58.92	58.20	**58.56**	0.26	0.51
E7-77.1	69.08	69.76	**69.42**	0.23	0.48
E7-77.2	72.58	73.60	**73.09**	0.52	0.72
E7-105.1	100.91	100.35	**100.63**	0.16	0.40
E7-105.2	92.58	92.70	**92.64**	0.01	0.08
E7-CP-105	153.87	152.57	**153.22**	0.85	0.92

SUPPLEMENTARY TABLE S2.8

Exp. 8 (^{43}Ca) sterile / anaerobic / 4°C

Sample	Measurement 1	Measurement 2	**Mean value**	Variance	STD
E8-CP-1	43.59	43.17	**43.38**	0.09	0.30
E8-7.1	34.32	33.69	**34.01**	0.20	0.45
E8-7.2	34.80	35.20	**35.00**	0.08	0.28
E8-14.1	36.56	38.05	**37.31**	1.11	1.05
E8-14.2	37.69	38.69	**38.19**	0.50	0.71
E8-21.1	38.45	38.52	**38.49**	0.00	0.05
E8-21.2	37.57	37.48	**37.53**	0.00	0.06
E8-49.1	52.90	53.28	**53.09**	0.07	0.27
E8-49.2	50.71	51.04	**50.88**	0.05	0.23
E8-77.1	66.03	66.98	**66.51**	0.45	0.67
E8-77.2	73.23	72.54	**72.89**	0.24	0.49
E8-105.1	73.90	75.00	**74.45**	0.60	0.78
E8-105.2	86.27	87.37	**86.82**	0.61	0.78
E8-CP-105	77.27	77.40	**77.34**	0.01	0.09

SUPPLEMENTARY TABLE S3.1

Changes due to decomposition in Exp. 1 (untreated / aerobic / 24°C)

Sample	Color	Cuticle	Branchiae	Hepatopancreas	Gastric	Intestine	Ganglion	Muscles
E1-2.1	red	solid	visible	visible	visible	visible	visible	normal
E1-2.2	red	solid	visible	visible	visible	visible	visible	normal
E1-3.1	red	solid	visible	visible	decomp.	visible	visible	normal
E1-3.2	red	solid	visible	visible	decomp.	visible	visible	normal
E1-4.1	red	solid	visible	visible	decomp.	visible	visible	pink
E1-4.2	red	solid	visible	visible	decomp.	visible	visible	pink
E1-7.1	red	jelly	decomp.	decomp.	decomp.	decomp.	decomp.	pulpy
E1-7.2	red	jelly	decomp.	decomp.	decomp.	decomp.	decomp.	pulpy
E1-14.1	red	jelly	decomp.	decomp.	decomp.	decomp.	decomp.	pulpy
E1-14.2	red	jelly	decomp.	decomp.	decomp.	decomp.	decomp.	pulpy
E1-21.1	red	jelly	decomp.	decomp.	decomp.	decomp.	decomp.	pulpy
E1-21.2	red	jelly	decomp.	decomp.	decomp.	decomp.	decomp.	pulpy
E1-21.3	red	jelly	decomp.	decomp.	decomp.	decomp.	decomp.	pulpy

SUPPLEMENTARY TABLE S3.2

Changes due to decomposition in Exp. 2 (sterile / aerobic / 24°C)

Sample	Color	Cuticle	Branchiae	Hepatopancreas	Gastric	Intestine	Ganglion	Muscles
E2-2.1	blue	solid	visible	visible	visible	visible	visible	normal
E2-2.2	blue	solid	visible	visible	visible	visible	visible	normal
E2-3.1	blue/red	solid	visible	visible	decomp.	visible	visible	normal
E2-3.2	blue/red	solid	visible	visible	decomp.	visible	visible	normal
E2-4.1	red	solid	visible	visible	decomp.	visible	visible	pink
E2-4.2	red	solid	visible	visible	decomp.	visible	visible	pink
E2-7.1	red	jelly	visible	decomp.	decomp.	decomp.	decomp.	pulpy
E2-7.2	red	jelly	visible	decomp.	decomp.	decomp.	decomp.	pulpy
E2-14.1	red	jelly	decomp.	decomp.	decomp.	decomp.	decomp.	pulpy
E2-14.2	red	jelly	decomp.	decomp.	decomp.	decomp.	decomp.	pulpy
E2-21.1	red	jelly	decomp.	decomp.	decomp.	decomp.	decomp.	pulpy
E2-21.2	red	jelly	decomp.	decomp.	decomp.	decomp.	decomp.	pulpy
E2-21.3	red	jelly	decomp.	decomp.	decomp.	decomp.	decomp.	pulpy

SUPPLEMENTARY TABLE S3.3

Changes due to decomposition in Exp. 3 (untreated / aerobic / 4°C)

Sample	Color	Cuticle	Branchiae	Hepatopancreas	Gastric	Intestine	Ganglion	Muscles
E3-7.1	blue	solid	visible	visible	visible	visible	visible	normal
E3-7.2	blue	solid	visible	visible	visible	visible	visible	normal
E3-14.1	blue	solid	visible	visible	visible	visible	visible	normal
E3-14.2	blue	solid	visible	visible	visible	visible	visible	normal
E3-21.1	blue	solid	visible	visible	visible	visible	visible	normal
E3-21.2	blue	solid	visible	visible	visible	visible	visible	normal
E3-49.1	blue	solid	visible	visible	visible	visible	visible	normal
E3-49.2	blue/red	solid	visible	decomp.	decomp.	visible	visible	pink
E3-77.1	red	soft	visible	decomp.	decomp.	visible	visible	pink
E3-77.2	red	soft	visible	decomp.	decomp.	visible	visible	pink
E3-105.1	red	soft	decomp.	decomp.	decomp.	visible	visible	pink
E3-105.2	red	soft	decomp.	decomp.	decomp.	visible	visible	pink

SUPPLEMENTARY TABLE S3.4

Changes due to decomposition in Exp. 4 (sterile / aerobic / 4°C)

Sample	Color	Cuticle	Branchiae	Hepatopancreas	Gastric	Intestine	Ganglion	Muscles
E4-7.1	blue	solid	visible	visible	visible	visible	visible	normal
E4-7.2	blue	solid	visible	visible	visible	visible	visible	normal
E4-14.1	blue	solid	visible	visible	visible	visible	visible	normal
E4-14.2	blue	solid	visible	visible	visible	visible	visible	normal
E4-21.1	red/blue	solid	visible	visible	visible	visible	visible	normal
E4-21.2	red/blue	solid	visible	visible	visible	visible	visible	normal
E4-49.1	red/blue	solid	visible	decomp.	decomp.	visible	visible	normal
E4-49.2	red/blue	solid	visible	visible	visible	visible	visible	normal
E4-77.1	red/blue	solid	visible	decomp.	decomp.	visible	visible	normal
E4-77.2	red/blue	solid	visible	decomp.	decomp.	visible	visible	normal
E4-105.1	red/blue	soft	decomp.	decomp.	decomp.	visible	visible	pink
E4-105.2	red/blue	soft	decomp.	decomp.	decomp.	visible	visible	pink

SUPPLEMENTARY TABLE S3.5

Changes due to decomposition in Exp. 5 (untreated / anaerobic / 24°C)

Sample	Color	Cuticle	Branchiae	Hepatopancreas	Gastric	Intestine	Ganglion	Muscles
E5-2.1	blue	solid	visible	visible	visible	visible	visible	normal
E5-2.2	blue	solid	visible	visible	visible	visible	visible	normal
E5-3.1	blue	solid	visible	visible	visible	visible	visible	pink
E5-3.2	blue	solid	visible	visible	visible	visible	visible	pink
E5-4.1	blue/red	solid	visible	decomp.	decomp.	visible	visible	pink
E5-4.2	blue/red	solid	visible	decomp.	decomp.	visible	visible	pink
E5-7.1	red/blue	jelly	decomp.	decomp.	decomp.	decomp.	decomp.	pulpy
E5-7.2	red/blue	jelly	decomp.	decomp.	decomp.	decomp.	decomp.	pulpy
E5-14.1	red	jelly	decomp.	decomp.	decomp.	decomp.	decomp.	pulpy
E5-14.2	red	jelly	decomp.	decomp.	decomp.	decomp.	decomp.	pulpy
E5-21.1	red	jelly	decomp.	decomp.	decomp.	decomp.	decomp.	pulpy
E5-21.2	red	jelly	decomp.	decomp.	decomp.	decomp.	decomp.	pulpy
E5-21.3	red	jelly	decomp.	decomp.	decomp.	decomp.	decomp.	pulpy

SUPPLEMENTARY TABLE S3.6

Changes due to decomposition in Exp. 6 (sterile / anaerobic / 24°C)

Sample	Color	Cuticle	Branchiae	Hepatopancreas	Gastric	Intestine	Ganglion	Muscles
E6-2.1	blue	solid	visible	visible	visible	visible	visible	normal
E6-2.2	blue	solid	visible	visible	visible	visible	visible	normal
E6-3.1	blue/red	solid	visible	visible	visible	visible	visible	pink
E6-3.2	blue/red	solid	visible	visible	visible	visible	visible	pink
E6-4.1	blue/red	solid	visible	decomp.	decomp.	visible	visible	pink
E6-4.2	blue/red	solid	visible	decomp.	decomp.	visible	visible	pink
E6-7.1	red	jelly	decomp.	decomp.	decomp.	decomp.	decomp.	pulpy
E6-7.2	red	jelly	decomp.	decomp.	decomp.	decomp.	decomp.	pulpy
E6-14.1	red	jelly	decomp.	decomp.	decomp.	decomp.	decomp.	pulpy
E6-14.2	red	jelly	decomp.	decomp.	decomp.	decomp.	decomp.	pulpy
E6-21.1	red	jelly	decomp.	decomp.	decomp.	decomp.	decomp.	pulpy
E6-21.2	red	jelly	decomp.	decomp.	decomp.	decomp.	decomp.	pulpy
E6-21.3	red	jelly	decomp.	decomp.	decomp.	decomp.	decomp.	pulpy

SUPPLEMENTARY TABLE S3.7

Changes due to decomposition in Exp. 7 (untreated / anaerobic / 4°C)

Sample	Color	Cuticle	Branchiae	Hepatopancreas	Gastric	Intestine	Ganglion	Muscles
E7-7.1	red	solid	visible	decomp.	decomp.	visible	visible	normal
E7-7.2	red	solid	visible	decomp.	visible	visible	visible	normal
E7-14.1	red	solid	visible	decomp.	decomp.	visible	visible	normal
E7-14.2	red	solid	visible	decomp.	decomp.	visible	visible	pink
E7-21.1	red	solid	visible	visible	visible	visible	visible	pink
E7-21.2	red	solid	visible	visible	visible	visible	visible	pink
E7-49.1	red	soft	visible	decomp.	decomp.	visible	visible	pink
E7-49.2	red	soft	visible	decomp.	decomp.	visible	visible	pink
E7-77.1	red	soft	decomp.	decomp.	decomp.	decomp.	visible	pulpy
E7-77.2	red	soft	decomp.	decomp.	decomp.	visible	visible	normal
E7-105.1	red	soft	visible	decomp.	decomp.	decomp.	decomp.	pulpy
E7-105.2	red	soft	visible	decomp.	decomp.	decomp.	decomp.	pulpy

SUPPLEMENTARY TABLE S3.8

Changes due to decomposition in Exp. 8 (sterile / anaerobic / 4°C)

Sample	Color	Cuticle	Branchiae	Hepatopancreas	Gastric	Intestine	Ganglion	Muscles
E8-7.1	red	solid	visible	decomp.	decomp.	visible	visible	normal
E8-7.2	red	solid	visible	decomp.	decomp.	visible	visible	normal
E8-14.1	blue	solid	visible	visible	visible	visible	visible	normal
E8-14.2	blue	solid	visible	visible	visible	visible	visible	normal
E8-21.1	green/blue	solid	visible	decomp.	decomp.	visible	visible	normal
E8-21.2	blue	solid	visible	visible	visible	visible	visible	normal
E8-49.1	blue/red	solid	visible	decomp.	decomp.	visible	visible	pink
E8-49.2	blue/red	solid	visible	decomp.	decomp.	visible	visible	pink
E8-77.1	blue/red	solid	visible	decomp.	visible	visible	visible	pink
E8-77.2	blue/red	solid	visible	decomp.	decomp.	visible	visible	pink
E8-105.1	green/red	soft	visible	decomp.	decomp.	visible	visible	pink
E8-105.2	green/red	soft	visible	decomp.	decomp.	visible	visible	pink

SUPPLEMENTARY TABLE S4.1

Environmental changes in Exp. 1 (untreated / aerobic / 24°C)

Sample	pH	O$_2$ [mg/L]	Water	Flower	Olfactics	Gas accumulation	Sediment
E1-CP	7.41	8.15	clear	no	neutral	no	normal
E1-2.1	6.95	8.30	clear	no	musty	no	normal
E1-2.2	6.88	8.25	clear	no	musty	no	normal
E1-3.1	6.70	8.35	clear	no	musty	no	normal
E1-3.2	6.90	8.30	clear	no	musty	no	normal
E1-4.1	6.68	8.40	clear	no	musty	no	normal
E1-4.2	6.96	8.40	clear	no	musty	no	normal
E1-7.1	6.89	7.30	clear	no	musty	no	normal
E1-7.2	6.81	7.45	clear	no	musty	no	normal
E1-14.1	7.52	7.90	gloomy	yes	musty	yes	black covered
E1-14.2	7.95	7.60	gloomy	yes	musty	yes	black covered
E1-21.1	7.37	3.90	gloomy	yes	musty	yes	black covered
E1-21.2	7.56	5.50	gloomy	yes	musty	yes	black covered
E1-21.3	7.48	3.75	gloomy	yes	musty	yes	black covered
E1-CP-End	7.93	7.90	clear	no	neutral	no	normal

SUPPLEMENTARY TABLE S4.2

Environmental changes in Exp. 2 (sterile / aerobic /24°C)

Sample	pH	O$_2$ [mg/L]	Water	Flower	Olfactics	Gas accumulation	Sediment
E2-CP	7.81	6.90	clear	no	neutral	no	normal
E2-2.1	6.21	6.70	clear	no	neutral	no	normal
E2-2.2	6.45	6.75	clear	no	neutral	no	normal
E2-3.1	6.33	6.85	gloomy	no	musty	no	normal
E2-3.2	6.42	6.85	gloomy	no	musty	no	normal
E2-4.1	6.51	6.90	gloomy	no	musty	no	normal
E2-4.2	6.38	6.85	gloomy	no	musty	no	normal
E2-7.1	6.40	7.00	gloomy	no	musty	no	normal
E2-7.2	6.33	6.90	gloomy	no	musty	no	normal
E2-14.1	6.49	1.10	gloomy	no	musty	no	black covered
E2-14.2	6.68	4.35	gloomy	no	musty	no	black covered
E2-21.1	7.05	6.90	gloomy	no	musty	no	black covered
E2-21.2	7.46	6.90	gloomy	no	musty	no	black covered
E2-21.3	6.53	6.95	gloomy	no	musty	no	black covered
E2-CP-End	7.27	7.4	clear	no	neutral	no	normal

SUPPLEMENTARY TABLE S4.3

Environmental changes in Exp. 3 (untreated / aerobic / 4°C)

Sample	pH	O_2 [mg/L]	Water	Flower	Olfactics	Gas accumulation	Sediment
E3-CP	7.85	8.80	clear	no	neutral	no	normal
E3-7.1	7.29	8.90	clear	no	neutral	no	normal
E3-7.2	7.35	8.90	clear	no	neutral	no	normal
E3-14.1	7.10	8.80	clear	no	neutral	no	normal
E3-14.2	6.95	8.80	clear	no	neutral	no	normal
E3-21.1	7.14	8.20	clear	no	musty	no	black covered
E3-21.2	7.02	8.30	clear	no	musty	no	black covered
E3-49.1	7.30	8.00	clear	no	musty	no	black covered
E3-49.2	6.50	7.80	clear	no	musty	no	black covered
E3-77.1	7.18	6.70	clear	no	musty	no	black covered
E3-77.2	7.51	6.70	clear	no	musty	no	black covered
E3-105.1	6.86	8.10	clear	no	musty	no	black covered
E3-105.2	6.91	8.00	clear	no	musty	no	black covered
E3-CP-End	7.33	8.90	clear	no	neutral	no	normal

SUPPLEMENTARY TABLE S4.4

Environmental changes in Exp.4 (sterile / aerobic / 4°C)

Sample	pH	O_2 [mg/L]	Water	Flower	Olfactics	Gas accumulation	Sediment
E4-CP	6.00	8.00	clear	no	neutral	no	normal
E4-7.1	7.40	8.00	clear	no	neutral	no	normal
E4-7.2	7.94	8.00	clear	no	neutral	no	normal
E4-14.1	6.90	8.00	clear	no	neutral	no	normal
E4-14.2	7.01	8.40	clear	no	neutral	no	normal
E4-21.1	6.61	8.70	clear	no	neutral	no	normal
E4-21.2	6.72	8.40	clear	no	neutral	no	normal
E4-49.1	7.04	8.40	clear	no	musty	no	normal
E4-49.2	7.01	8.40	clear	no	musty	no	normal
E4-77.1	7.18	7.11	clear	no	musty	no	white covered
E4-77.2	7.19	7.13	clear	no	musty	no	white covered
E4-105.1	6.62	2.00	clear	no	musty	no	normal
E4-105.2	6.93	2.00	clear	no	musty	no	normal
E4-CP-End	6.93	8.00	clear	no	neutral	no	normal

SUPPLEMENTARY TABLE S4.5

Environmental changes in Exp. 5 (untreated / anaerobic / 24°C)

Sample	pH	O₂ [mg/L]	Water	Flower	Olfactics	Gas accumulation	Sediment
E5-CP	7.29	0.80	clear	no	neutral	no	normal
E5-2.1	7.24	3.00	clear	no	neutral	no	normal
E5-2.2	7.14	2.90	clear	no	neutral	no	normal
E5-3.1	7.08	1.70	clear	no	musty	no	normal
E5-3.2	7.00	1.50	clear	no	musty	no	normal
E5-4.1	6.83	2.70	clear	no	musty	no	normal
E5-4.2	6.70	3.40	clear	no	musty	no	normal
E5-7.1	6.62	2.00	clear	no	musty	no	normal
E5-7.2	6.62	2.00	clear	no	musty	no	normal
E5-14.1	6.60	1.50	clear	no	musty	no	black covered
E5-14.2	6.57	1.50	clear	no	musty	no	black covered
E5-21.1	6.45	1.10	gloomy	no	musty	no	black covered
E5-21.2	6.52	1.00	gloomy	no	musty	no	black covered
E5-21.3	6.54	0.80	gloomy	no	musty	no	black covered
E5-CP-End	6.93	0.80	clear	no	neutral	no	normal

SUPPLEMENTARY TABLE S4.6

Environmental changes in Exp. 6 (sterile / anaerobic / 24°C)

Sample	pH	O₂ [mg/L]	Water	Flower	Olfactics	Gas accumulation	Sediment
E6-CP	7.29	0.90	clear	no	neutral	no	normal
E6-2.1	6.72	1.50	clear	no	neutral	no	normal
E6-2.2	6.89	1.50	clear	no	neutral	no	normal
E6-3.1	6.65	4.50	gloomy	no	musty	no	normal
E6-3.2	6.54	4.50	gloomy	no	musty	no	normal
E6-4.1	6.42	1.20	gloomy	no	musty	no	normal
E6-4.2	6.59	3.20	gloomy	no	musty	no	normal
E6-7.1	6.58	0.80	gloomy	no	musty	no	normal
E6-7.2	6.65	1.10	gloomy	no	musty	no	normal
E6-14.1	6.50	1.10	gloomy	no	musty	no	normal
E6-14.2	6.76	1.10	gloomy	no	musty	no	normal
E6-21.1	6.53	0.80	gloomy	no	musty	no	normal
E6-21.2	6.44	0.80	gloomy	no	musty	no	black covered
E6-21.3	6.43	0.90	gloomy	no	musty	no	black covered
E6-CP-End	7.06	0.90	clear	no	neutral	no	normal

SUPPLEMENTARY TABLE S4.7

Environmental changes in Exp. 7 (untreated / anaerobic / 4°C)

Sample	pH	O_2 [mg/L]	Water	Flower	Olfactics	Gas accumulation	Sediment
E7-CP	7.95	7.00	clear	no	neutral	no	normal
E7-7.1	7.16	2.60	clear	no	neutral	no	normal
E7-7.2	7.10	1.90	clear	no	neutral	no	normal
E7-14.1	7.00	7.70	clear	no	neutral	no	normal
E7-14.2	7.00	7.70	clear	no	neutral	no	normal
E7-21.1	6.98	5.50	clear	no	musty	no	black covered
E7-21.2	6.97	5.50	clear	no	musty	no	black covered
E7-49.1	6.81	2.00	clear	no	musty	no	black covered
E7-49.2	6.84	1.80	clear	no	musty	no	black covered
E7-77.1	6.76	2.60	clear	no	musty	no	black covered
E7-77.2	6.76	2.60	clear	no	musty	no	black covered
E7-105.1	6.72	1.90	clear	no	musty	no	black covered
E7-105.2	6.61	1.30	clear	no	musty	no	black covered
E7-CP-End	6.59	1.20	clear	no	neutral	no	normal

SUPPLEMENTARY TABLE S4.8

Environmental changes in Exp. 8 (sterile / anaerobic / 4°C)

Sample	pH	O_2 [mg/L]	Water	Flower	Olfactics	Gas accumulation	Sediment
E8-CP	7.95	8.00	clear	no	neutral	no	normal
E8-7.1	7.03	6.20	clear	no	neutral	no	normal
E8-7.2	7.09	6.40	clear	no	neutral	no	normal
E8-14.1	7.00	7.10	clear	no	neutral	no	normal
E8-14.2	7.00	6.90	clear	no	neutral	no	normal
E8-21.1	6.97	6.30	clear	no	neutral	no	normal
E8-21.2	6.98	6.10	clear	no	neutral	no	normal
E8-49.1	6.46	1.80	clear	no	musty	no	normal
E8-49.2	6.58	2.60	clear	no	musty	no	normal
E8-77.1	6.72	2.70	clear	no	musty	no	normal
E8-77.2	6.56	2.40	clear	no	musty	no	normal
E8-105.1	6.95	2.40	clear	no	musty	no	normal
E8-105.2	6.41	1.20	clear	no	musty	no	normal
E8-CP-End	6.53	1.20	clear	no	neutral	no	normal

SUPPLEMENTARY TABLE S5.1

Total Volume of Calcite (TVC) [mm^3] 24°C

Sample	Day 1	Day 2	Day 3	Day 4	Day 7	Day 14	Day 21
E1-21.1	-	-	-	0.400	1.589	1.999	2.779
E1-21.2	-	-	-	0.034	0.058	0.064	0.082
E1-21.3	-	-	-	0.152	1.086	1.464	2.020
E2-21.1	-	-	-	-	-	-	-
E2-21.2	-	0.003	0.019	0.027	0.196	0.251	0.379
E2-21.3	-	-	0.406	0.804	0.907	0.914	0.947
E5-21.1	-	-	-	-	0.045	0.090	0.107
E5-21.2	-	-	0.384	1.504	1.822	1.874	2.659
E5-21.3	-	-	-	0.114	1.521	1.930	2.353
E6-21.1	-	-	-	0.065	0.311	0.276	0.261
E6-21.2	-	-	-	-	0.046	0.066	0.050
E6-21.3	-	-	0.185	0.701	1.544	1.040	0.457

SUPPLEMENTARY TABLE S5.2

Total Volume of Calcite (TVC) [mm^3] 4°C

Sample	Day 1	Day 7	Day 14	Day 21	Day 49	Day 77	Day 105
E3-105.1	-	-	-	-	-	-	-
E3-105.2	-	-	-	-	-	-	-
E4-105.1	-	-	-	-	-	-	-
E4-105.2	-	-	-	-	-	-	-
E7-105.1	-	-	-	-	-	-	-
E7-105.2	-	-	-	-	-	-	-
E8-105.1	-	-	-	-	-	-	-
E8-105.2	-	-	-	-	-	-	-

SUPPLEMENTARY TABLE S6.1

Total Volume of Gastroliths (TVG) [mm^3] 24°C

Sample	Day 1	Day 2	Day 3	Day 4	Day 7	Day 14	Day 21
E1-21.1	0.190	0.187	0.182	0.179	0.169	0.146	0.132
E1-21.2	4.571	4.330	3.951	3.843	3.093	2.192	2.042
E1-21.3	0.148	0.143	0.137	0.134	0.009	0.005	-
E2-21.1	0.041	0.040	0.037	0.032	0.016	0.016	-
E2-21.2	1.288	1.282	1.233	1.204	1.102	0.645	-
E2-21.3	0.127	0.099	0.095	0.075	0.061	0.020	-
E5-21.1	-	-	-	-	-	-	-
E5-21.2	-	-	-	-	-	-	-
E5-21.3	-	-	-	-	-	-	-
E6-21.1	-	-	-	-	-	-	-
E6-21.2	-	-	-	-	-	-	-
E6-21.3	-	-	-	-	-	-	-

SUPPLEMENTARY TABLE S6.2

Total Volume of Gastroliths (TVG) [mm^3] 4°C

Sample	Day 1	Day 7	Day 14	Day 21	Day 49	Day 77	Day 105
E3-105.1	0.116	0.098	0.081	0.060	0.056	0.043	0.029
E3-105.2	-	-	-	-	-	-	-
E4-105.1	-	-	-	-	-	-	-
E4-105.2	0.549	0.537	0.503	0.496	0.440	0.431	0.373
E7-105.1	-	-	-	-	-	-	-
E7-105.2	-	-	-	-	-	-	-
E8-105.1	-	-	-	-	-	-	-
E8-105.2	-	-	-	-	-	-	-

Declaration of authorship

Chapter 1

<u>Unpublished:</u>

Bastian Mähler wrote the General Introduction and designed all figures.

Chapter 2

<u>Published as:</u> Janssen, K.[*], **Mähler, B.**[*], Rust, J., Bierbaum, G. & McCoy, V.E. (2021). The complex role of microbial activity in fossilization. *Biological Reviews*.

https://doi.org/10.1111/brv.12806

*Authors contributed equally to this work.

Chapter 3

<u>Published as:</u> **Mähler, B.**[*], Janssen, K., Menneken, M., Tahoun, M., Lagos, M., Bierbaum, G., Müller, C.E. & Rust, J. (2020). Calcite precipitation forms crystal clusters and muscle mineralization during the decomposition of *Cambarellus diminutus* (Decapoda: Cambaridae) in freshwater. *Palaeontologia Electronica*.

https://doi.org/10.26879/992

*Corresponding author

Bastian Mähler designed the study and prepared the manuscript. He did analysis with μ-CT, SEM, ICPMS and virtual reconstruction. He also designed the figures (except Figure 7).

Kathrin Janssen wrote a part in the discussion about urea and bacteria.

Martina Menneken did CRS analysis, wrote the text parts and did Figure 7.

Mariam Tahoun did AAS analysis and wrote the text parts.

Markus Lagos prepared the calibration solution and calibrated the device. *Bastian Mähler* prepared the sample solutions and did ICPMS analysis. *Markus Lagos* wrote the methods part and *Bastian Mähler* did the evaluation of the data.

Chapter 3: Additional Information (AI)

Bastian Mähler did SEM, μ-CT, virtual reconstruction and ICPMS. He designed the tables and figures except Figure AI 2

Martina Menneken did CRS analysis and designed Figure AI 2

Chapter 3: Additional Study (AS)

Bastian Mähler did SEM, μ-CT, virtual reconstruction and took photos of crystal structures with a digital microscope. He designed the figures except Figure AS 4

Martina Menneken did CRS analysis and designed Figure AS 4

Markus Lagos prepared the calibration solution and calibrated the device. *Bastian Mähler* prepared the sample solutions and did ICPMS analysis. *Bastian Mähler* wrote the methods part and did the evaluation of the data.

Chapter 4

Review in progress *Scientific Reports*: **Mähler, B.**[*], Janssen, K., Tahoun, M., Tomaschek, F., Schellhorn, R., Müller, C.E., Bierbaum, G. & Rust, J. (sub. 2022). Adipocere formation in biofilms as a first step in soft tissue preservation.

 *Corresponding author

Bastian Mähler designed the study and prepared the manuscript. He did analysis with μ-CT, SEM, virtual reconstruction, took the photos, prepared the samples for further analysis with CRS, did general observation and dissections. He also designed Table 1 and the figures (except Figure 3.3, 5, 11 and 12, as well as Supplementary Figure S1 and S2).

Kathrin Janssen did DNA extraction, 16S rRNA gene amplicon sequencing wrote the text parts and designed Figure 5.

Mariam Tahoun did HPLC-UV/MS analysis, wrote the text parts and designed Table S1, Figure 11 and 12, as well as Supplementary Figure S1 and S2.

Frank Tomaschek did CRS analysis, wrote the text parts and designed Figure 3.3.

Chapter 5

Unpublished:

Bastian Mähler designed the study and prepared the main text parts. He did analysis with μ-CT, SEM, ICPMS, virtual reconstruction, took the photos, prepared the samples for further analysis with CRS and ICPMS, did general observations and dissections. He also designed the figures and all Supplementary Tables (except Figure 16).

Mara Lönartz did CRS analysis, wrote the text parts and designed Figure 16.

Markus Lagos prepared the calibration solution and calibrated the device. *Bastian Mähler* prepared the sample solutions and did ICPMS analysis. *Markus Lagos* wrote the methods part and *Bastian Mähler* did the evaluation of the data.